


Doctoral Dissertation
Doctoral Program in Bioengineering and medical-surgical sciences (32^{nd} cycle)

Fracture Risk of the Proximal Femur in Osteoporosis: a Closer Look at the Role of Geometry

Alessandra Aldieri

* * * * * *

Supervisors
Prof. Alberto L. Audenino, Supervisor
Prof. Cristina Bignardi, Co-supervisor

Doctoral examination committee
Prof. Tomaso Maria Villa, Referee, Politecnico di Milano
Dr. Pinaki Bhattacharya, Referee, University of Sheffield

Politecnico di Torino
April 2020

I hereby declare that, the contents and organisation of this dissertation constitute my own original work and does not compromise in any way the rights of third parties, including those relating to the security of personal data.

Alessandra Aldieri
Torino, April 2020

Summary

Osteoporosis, the silent disease, is a metabolic disorder mainly affecting post-menopausal women which induces progressive loss and deterioration of the bone tissue. The bone gradually becomes more porous and fragile often without symptoms, until a fracture occurs. 200 million people are currently affected by this disorder globally, and due to the increased longevity of the population, especially in western countries, its incidence is expected to grow dramatically over the next 30 years. Osteoporosis clinical relevance lies in the fractures it causes: according to the World Health Organization, in 2010 3.5 million fractures were estimated to have occurred in European countries. Not only impressively high levels of morbidity and mortality are associated to these fractures, but there are also strong economic implications for the healthcare systems. Among osteoporotic fractures, hip fractures are considered to be particularly devastating because of the severe aftermaths they entail as well as the related costs. At present, the presence of osteoporosis is assessed based on the Bone Mineral Density (BMD) measurement using DXA, the standard imaging technology for diagnosis purposes. Comparing the patient-specific BMD value with that related to a standard young population, the T-score is computed, which represents the gold-standard for patients classification. Based on the T-score value, patients are indeed classified as healthy (T-score > -1), osteopenic ($-2.5 <$ T-score < -1) or osteoporotic (T-score < -2.5). However, T-score predictive weaknesses have increasingly been highlighted in literature. In particular, its poor sensitivity has been pointed out, given

that almost half of the people suffering from an osteoporosis-related fracture would not be currently classified as at risk by the T-score.

Against this background, the main purpose of the work presented within this thesis was to investigate if the current gold-standard predictive performances in estimating the proximal femur fracture risk could be enhanced. Particular attention was paid to the proximal femur geometry, since geometry does represent a determinant of the resistance to loading of a structure. In this respect, Hip Structural Analysis (HSA) is a tool allowing the extraction of a number of geometric variables directly from the mineral mass information contained in DXA images. HSA variables are provided to clinicians together with the DXA related data, but do not actually find any practical application.
To achieve the main objective of the study, a cohort of 28 post-menopausal was used, for whom DXA and CT images were available simultaneously. Unfortunately, no follow-up information was available for them, but two additional patients, fractured at the proximal femur because of a fall at home within 1 year after the DXA exam, were included in the study although lacking the CT images.

In the first chapter, three-dimensional Finite Element (FE) analyses were built taking advantage of the available CT images. Indeed, they allowed the construction of realistic models combining the three-dimensional patient-specific anatomical features and heterogeneous material properties distribution. To investigate the patient-specific risk of proximal femur fracture, a sideways fall condition was simulated and two different fracture risk indices, the Risk Factor Index (RFI) and the Femoral Strength (FS) were extracted adopting principal strains-based failure criteria. Subsequently, a multivariate regression analysis was carried out in order to identify the optimal regression model for predicting the RFI and FS from the available HSA parameters. CT is not indeed routinely employed for

osteoporotic patients and the 3D models development is therefore prevented. That is the main reason why HSA variables, clinically available, were included in the regression analysis, aiming to identify those most relevant with respect to estimated fracture predictors. The most meaningful HSA parameters turned out to be the buckling ratio at the neck and shaft together with the neck shaft angle. This outcome was consistent with the prevailing bending stress occurring, especially at the neck, during sideways falls and with the reduction in cortical stability which takes place with ageing, and is worsened by osteoporosis. Moreover, compared to the T-score, the two risk indices allowed to disclose distinct risk levels among patients belonging to the same T-score range, with particular attention to the osteopenic one. From this perspective, the two additional fractured patients, osteopenic, were correctly predicted by the optimal regression models in the higher risk regions.

In the second chapter, two-dimensional FE analyses built on DXA images were performed in analogy with the CT-based ones of the previous chapter. Patient-specific proximal femur geometry and heterogeneous material properties based on the available pixel-by-pixel BMD maps were included in the analyses, although characterized by the projective nature of the DXA image. The purpose was to assess if DXA-based FE analyses, which would be clinically attainable because based on the standard imaging technique, could be considered comparable to the CT-based ones. Therefore, patient-specific 2D FE analyses reproducing a sideways fall were carried out for the 28 patients analogously to those performed in the previous chapter on the same patients. Equivalent fracture risk indices, RFI and FS, were computed (RFI_{2D} and FS_{2D}). Although a significant correlation was found between the 2D and 3D risk predictors, the correlation was modest, thus supporting the conclusion that CT- and DXA-based outcomes would not appear to be equivalent. However, the HSA variables identified as the most relevant to the two-dimensional fracture risk were the buckling ratio at the neck and shaft, cross-sectional moment of inertia

and neck-shaft angle, not discordant to those relevant to the CT-based risk. Furthermore, compared to the T-score, RFI_{2D} and FS_{2D} highlighted as at higher risk the same patients the CT-based RFI and FS drew attention to. The fractured patients were correctly located in the high risk area by the FS_{2D}, only one by the RFI_{2D}.

In the third chapter, statistical shape and intensity models were built aiming to further investigate the role of geometry, BMD distribution and their interaction within the fracture risk determination. Principal Component Analysis (PCA) and Partial Least Square (PLS) algorithms were employed, aiming to identify not only the most meaningful modes of variations of the shape and BMD distribution, but also those most relevant with respect to the 3D-based Femoral Strength (FS). DXA-based shape and BMD data were used, with the purpose of accomplishing usable outcomes, able to be integrated in the current diagnostic framework. On the other hand, the FS extracted from the CT-based FE analyses was used as the reference response variable, judged more realistic and comprehensive. Statistical shape modelling allowed to capture global morphological features not limited to the HSA variables, which are discrete and often interrelated. In addition, the main intensity features could be gathered as a whole through statistical intensity modelling. Interestingly, significant correlations were identified between the main intensity and shape modes. The most meaningful BMD distribution features turned out to be able to explain most of the variance contained in the FS. However, when combined with shape features, the percentage of variance explained increased from 57.18% to 66.9%. Eventually, Canonical Correlation Analysis allowed to predict the changes in shape and BMD distribution occurring for decreasing FS values. In this respect, the main anatomical alterations interested an increase in the neck-shaft angle and a narrowing of the intertrochanter width.

In conclusion, this works represents an attempt to clarify the role of

geometry within the osteoporotic fracture risk of the proximal femur. The HSA variables most relevant to the fracture risk were, except for the neck-shaft angle, all intrinsically tightly related to the density distribution. This might appear an evidence of the fact that the use of HSA variables as risk predictors might be misleading in interpreting the role of geometry, since they are actually determined based on the mineral mass distribution enclosed in DXA images. From this perspective, statistical shape-intensity modelling highlighted this aspect, since most of the femoral strength variance was explained by the main BMD distribution features rather than by the anatomical ones. However, the inclusion of shape features did lead to an improvement, which might seem to witness a role of geometry. DXA-based FE analyses, combining the heterogeneous material properties extracted from the local BMD map with the patient-specific 2D femoral shape, did manage to better stratify osteopenic patients, although they may not be considered equivalent to CT-based FE analyses.
In the end, larger cohorts with available follow-up information will unquestionably help in gaining further insights in the synergistic role shape and BMD distribution play as proximal femur fracture risk determinants, but the results, with regard to the statistical shape-intensity modelling approaches especially, appear promising tools for accomplishing that ambition.

Contents

Chapter 1

Introduction

1.1 Phisiopatology

Osteoporosis is a silent metabolic disorder which entails significant reductions in the density and quality of the bone, therefore affecting its mechanical strength. As bone loss and deterioration occur and bone gets more porous and fragile, the risk of fracture is highly increased (Figure 1.1). Bone degradation occurs silently and progressively, often without

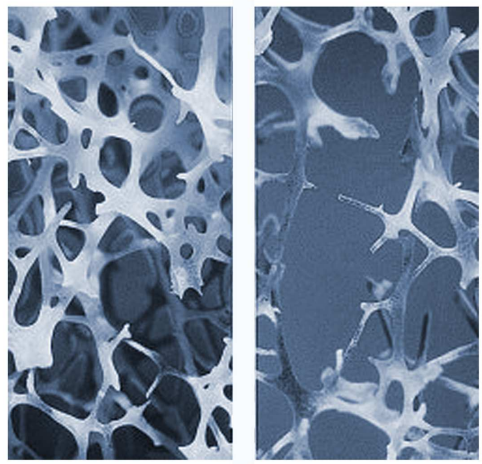

Figure 1.1: The comparison between normal bone (left) and osteoporotic bone (right). From http://www.iofbonehealth.org/.

symptoms until the first fracture occurs. One fracture every 3 seconds has been estimated to to take place.

Two different kinds of bone can be distinguised in the adult human skeleton: cortical and trabecular bone. Cortical bone is dense and compact, it encases all parts of the skeleton, but it is prominent in the diaphyses of long bones, such as the femur. Trabecular or cancelleous bone, on the contrary, abundant in the spine, is formed by a porous and interlocking structure of vertical and horizontal *trabeculae*. Although being architecturally different, these two types of bones are very similar at the molecular and biochemical levels. Indeed, the main structural constituents

of bone tissue as a whole are the Extra-Cellular Matrix (ECM) and the cells. While cells are responsible for the control of bone formation and resorption, the ECM, together with the geometric and micro-architectural features related to the tissue distribution in space, governs its mechanical properties. The ECM is made up of a non-mineralized component, known as osteoid, which is mainly composed of collagen and in which cells are embedded, plus a minerlized component, hydroxyapatite, deposited on the osteoid in a highly organized way [1]. The physiological homeostasis of this metabolically active tissue is maintained thanks to the activities of osteoclasts, cells responsible for bone resorption, and osteoblasts, responsible for bone formation. Bone is indeed continuously formed, reabsorbed, and replaced within this so called bone remodelling process. Therefore, changes in bone mass depend on the coordinated actions of these bone reabsorbing and forming cells. Increased bone resorption or decreased bone formation might indeed result in osteoporosis.

The awareness of a particular condition in which bone resulted weakened, thus fostering the occurrence of fractures, lies back to the XIX century. In the early 1820s indeed, Sir Astley Cooper registered that London hospitals were "*seldom without an example of fracture of the neck of the thighbone*", highlighting how "*women are much more likely to this species of fracture than men*", and that this kind of fractures "*seldom happens but at an advanced period of life*". Osteoporosis, literally meaning 'porous bone', was subsequently defined during the first half of the XX century as "*atrophy*" of the fully developed bone producing a "*rarefied skeleton*" by Albright et al., in a study involving 40 post-menopausal women [2], which thus formulated the basis for the ensuing research. Eventually, in 1994, the World Health Organization (WHO) issued a report where osteoporosis was comprehensively defined as "a disease characterised by low bone mass and micro-architectural deterioration of bone tissue, leading to enhanced bone fragility and a consequent increase in fracture risk" [3].
Osteoporosis, which has since then kept the 1994 WHO definition, is to date categorized into primary and secondary causes. Primary osteoporosis

is further classified into Type I, associated to menopause and oestrogen deficiency, and Type II osteoporosis, which affects both men and women older than 70 years. Secondary causes, on the contrary, might ensue a number of disorders, such as endocrine, hematopoietic or renal diseases, and medications [4]. Due to the cohort included in this thesis, made up of post-menopausal women, primary osteoporosis will be the main focus of the work.

Actually, during lifetime, the bone remodelling process acts indeed in favour of the deposition phase until the achievement of the peak bone mass, at the age of 25-30 years. Afterwards, following a temporary period of stability, bone loss begins at about the age of 35 years [5]. This process is accelerated in the immediate post-menopausal years in women. In fact, the production of oestrogen, an hormone playing a central role in regulating the remodelling process, undergoes a steep decrease after the menopause, leading to further bone loss and deterioration. Low bone mass and microarchitecturally deteriorated bone tissue, which characterize osteoporosis, therefore lead to enhanced bone fragility and increased fracture risk with ageing (Figure 1.2). Beyond tissue mineralization den-

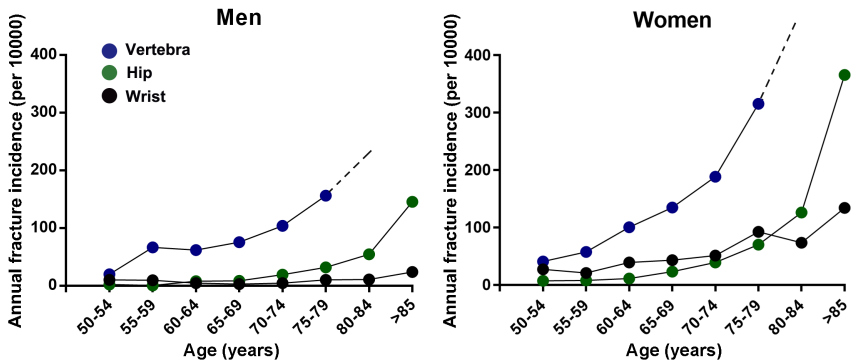

Figure 1.2: Age- and sex-specific incidence of vertebral, hip and wrist fracture. The fracture incidence rises with age for both men and women, although the increase in much steeper for women. Adapted from Cooper et al., 1993 [6].

sity, the strength of a bone comprises a number of components including

bone architecture, geometry, porosity, and is therefore strictly related to bone quality, microarchitecture and bone mass distribution. Although bone loss interests the bone mass as a whole, cancelleous bone horizontal *trabeculae* are particularly predisposed to resorption. Without the support of these crossing horizontal components, vertical *trabeculae* are much more susceptible to compressive instability, and this often leads to crush of the cancelleous bone, frequently observed within the spine [1].
Primary osteoporosis develops slowly and silently, until it suddenly manifests with fractures, its main aftermath, which are where its clinical significance lies [7]. Beyond age and menopause-related bone loss, also muscle strength, poor balance, visual acuity might interact with a poor bone mass playing a pivotal role in determining the fracture risk. As a matter of fact, osteoporotic fractures represent multi-factorial complex events, resulting primarily from a combination of reduced bone strength and increased rate of falls (Figure 1.3).

1.2 Epidemiology

Osteoporosis is the most common metabolic disorder, affecting 200 million people all over the world [4]. In 2010, 22 million women and 5.5 million men in the European Union (EU) had osteoporosis according to the WHO diagnostic criteria [9]. Its incidence raises with ageing, and due to the increased longevity of the population, it is expected to grow dramatically. In Europe, the proportion of elderly people over the whole population will rise by 33% over the next 25 years [7] and in Italy, where 3.5 million women and 1 million men have been estimated to suffer from osteoporosis, the proportion of individuals over 65 years is expected to increase by 25% in the next 20 years, reasonably leading to a proportional increase in osteoporosis incidence [10].

Although both men and women are affected by this disorder, women, as already mentioned, are those worst hit: worldwide, one in three women over 50 years will indeed undergo a fracture in her lifetime, compared to

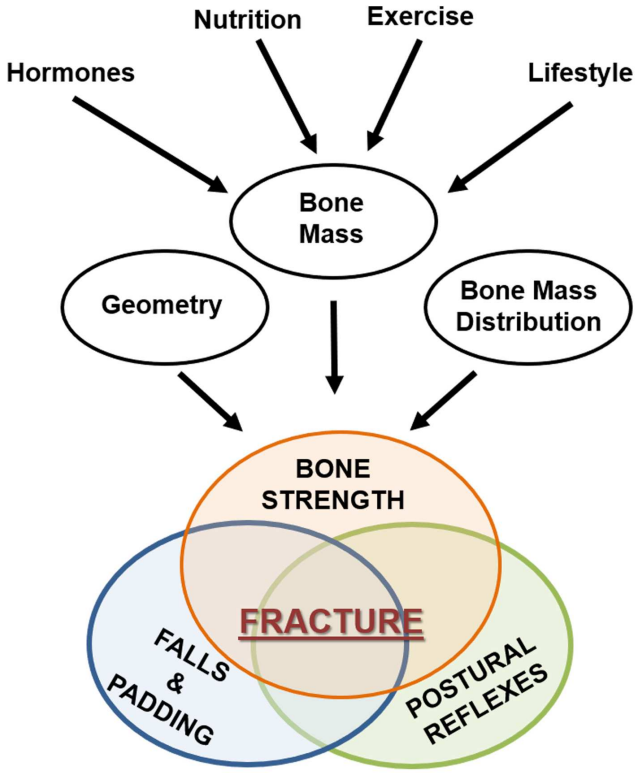

Figure 1.3: The interplay among the main pathogenetic factors contributing to the occurrence of osteoporotic fractures. Adapted from Heaney, 1974 [8].

the one in five men doing so [11]. Furthermore, age has a strong impact on osteoporosis incidence: based on the WHO diagnostic criteria, osteoporosis affects 20% of all post-menopausal Caucasian women and 50% of those aged 80 years. Looking at the Italian hip fracture incidence for men and women (Figure 1.4), an exponential increase in incidence can be observed, with much higher rates in women compared to men.

Osteoporosis manifests clinically with fractures, with one fracture estimated to occur every 3 seconds [7], more than 8.9 million annually. The definition of osteoporotic fracture is actually not straightforward. In fact,

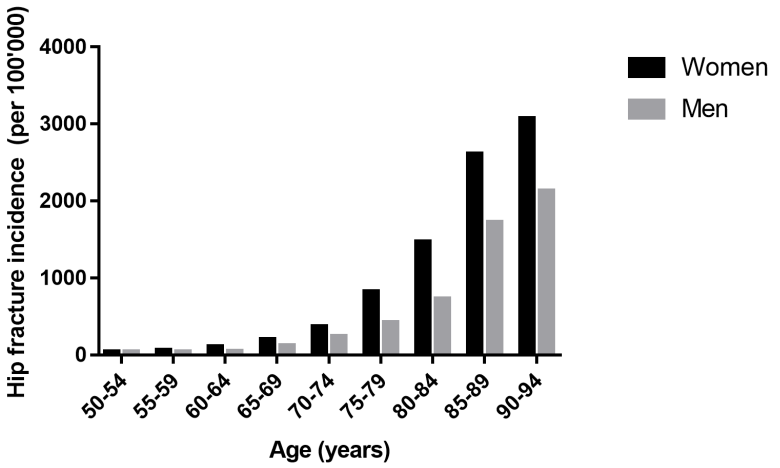

Figure 1.4: Hip fracture incidence (per 100'000) by age in Italian men and women. Adapted from [7].

the increasing rate of fractures with age does not provide sufficient evidence for osteoporosis, as it could be related to an higher incidence of falls [7]. Usually, however, fracture sites are considered to be osteoporotic when associated to low bone mass and their incidence rises with age after the age of 50 years [7]. The most common fracture sites are the hip, spine, distal forearm, and proximal humerus [12]. Fractures rates are much higher in the western countries: in spite of its more modest population, approximately one third of the osteoporotic fractures occur in Europe. In 2010, the WHO estimated, in European countries, 3.5 million fractures [13]. Beyond this health burden, the occurrence of osteoporotic fractures has significant social and economic implications, with great impact on health care systems, morbidity and mortality [12]. Osteoporotic fractures represent indeed one of the main causes of death among the elderly, with incidence comparable to stroke and breast cancer [10]. In 2010, the number of deaths causally related to this kind of fractures were estimated at 43000 in the EU [13]. Osteoporotic fractures also lead to a considerable reduction in the

level of independence due to disability and, therefore, to an higher need for long-term care (Figure 1.5). From this perspective, osteoporosis costs, including pharmacological interventions, were registered to amount to €37 billion in 2010 [13]. Costs of treating incident fractures represented 66%

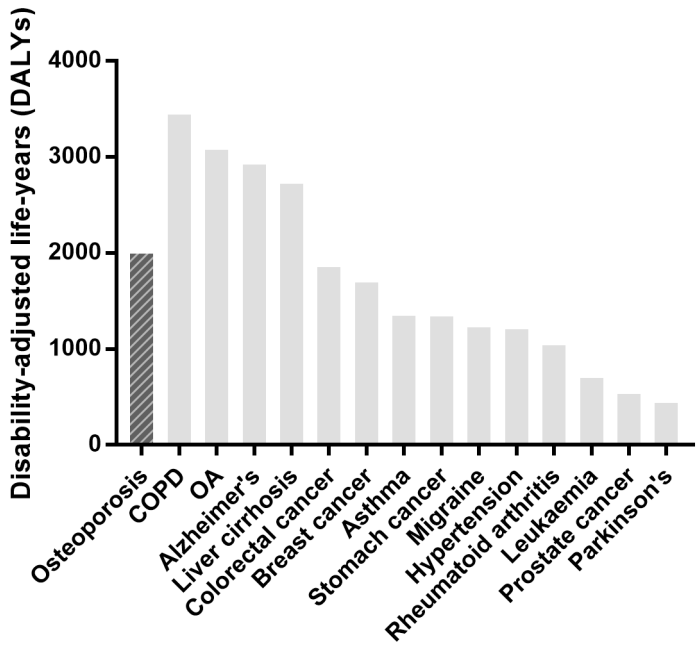

Figure 1.5: Disability-adjusted life-years (DALYs) lost due to a number of diseases. COPD: Chronic Obstructive Pulmonary Disease, OA: Osteoarthritis. Adapted from [14].

of these costs, pharmacological interventions 5%, long-term fracture care 29%. Not accounting for the pharmacological prevention-related costs, hip fractures alone represented 54% of the total costs [9]. Among osteoporotic fractures, hip fractures are indeed the most serious, with a 10-20% increased mortality in the first year following the fracture [15]. Approximately 50% of fracture-related deaths are estimated to be due to hip fractures [9]. Besides, fractures of the proximal femur are considered to

be particularly devastating due to the significant aftermaths they cause in terms of persistent pain and limited physical mobility [16]. Due to the growing global life expectancy, worldwide, the incidence of hip fractures is estimated to increase by 3.5 times by 2050, ascending to a total of 6.26 million fractures in the same year [17]. Mainly caused by falls [7], they result, *inter alia*, from the age-related decrease in bone mass at the proximal femur together with an age-related increased rate of falls. The lifetime risk of hip fracture for a woman is 14%; because risk increases with age, women who are older than 85 years are approximately eight times more likely than women 65–74 years old to be admitted to the hospital for a hip fracture [4]. In 2017, in Italy, a total of 560000 fractures were recorded, with a related health-care system cost of €9.4 billion. 20% of them being represented by hip fractures, they were responsible for an expense of approximately €6 billion (*2018 country-specific report on the clinical, societal, and cost burden associated with fragility fractures*: `http://www.panoramasanita.it/wp-content/uploads/2018/10/report-firmo-iof.pdf`).

1.3 Assessment of fracture risk

As suggested by the osteoporosis definition presented previously, bone mass represents an important component of the risk of fracture, although other factors, such as bone microarchitecture or geometry, affect bone strength and, consequently, its resistance to trauma [10, 18]. At present, nevertheless, bone mass is the main variable employed clinically, on which diagnosis, monitoring and the management of the disease in general are based. Bone Mineral Density (BMD) is the clinical parameter used, which is derived from the Bone Mineral Content (BMC, expressed in grams) and can be measured *in vivo* exploiting a variety of techniques such as Quantitative Computed Tomography (QCT), Dual X-ray Absorptiometry (DXA), quantitative ultrasound and quantitative magnet-resonance tomography, though DXA is the current gold-standard technique (Table 1.1). DXA fundamental principle is the variable absorption of X-rays by

different body components. By measuring the attenuation of X-rays with high- and low-energy photons, the bone can be distinguished from soft tissues and the mineralized bone mass eventually assessed neglecting surrounding soft tissues attenuation effect. DXA is highly accurate and fast, subjecting the patients to a low radiation dose (Table 1.1) [19].
The image DXA yields is the two-dimensional projection of the mineral

Table 1.1: General overview of the most common techniques to assess the bone mass. Adapted from [19].

Technique	**Site**	**Scan Time** (min)	**Precision error** (%)	**Radiation exposure** (mrem)
DXA	Radius, Calcaneus Spine, Hip Whole body	5-15	1-3	1-5
QCT	Spine	10-30	2-4	50
QUS	Calcaneus, Tibia	5-10	3-4	0

mass: in particular, its pixels are the sum of the mineral mass along the ray path (along a line) extending from the X-ray source, through the body of the patient, to the detector [20]. From this perspective, DXA main drawback is that it can only provide a two-dimensional image, therefore only allowing to obtain an actually areal BMD, the BMC per unit area (g/cm^2). However, it is very versatile, allowing the assessment of bone mineral content of the whole skeleton as well as at specific sites, such as those most susceptible to fracture. The most commonly measured sites for DXA-based BMD measurements are the proximal femur and the lumbar spine, but alternative sites might be the calcaneus, proximal and distal radius. Since vertebral and hip fractures are the most clinically relevant fractures, lumbar spine and proximal femur do represent the most frequently assessed sites (Figure 1.6). BMD is more often expressed in units of Standard Deviation (SD) as the T-score. T-score represents the number of SDs the patient-specific BMD differs from the mean value of a young

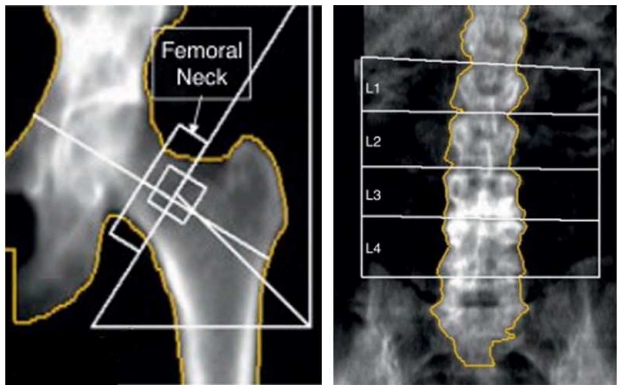

Figure 1.6: One typical DXA image at the hip (left) and at the lumbar spine (rigth). Adapted from [21].

standard population. Because a reduced BMD has been shown to be one of the strongest risk factor for fractures [10, 19, 22], osteoporosis diagnostic definition is based on the T-score. In 1994 indeed, the WHO published diagnostic criteria for post-menopausal women grounded on the T-score, which, since then, have been widely accepted and used [3]. According to the WHO, the thresholds presented in Table 1.2, referred to T-score values computed at the hip, lumbar spine or forearm, should be considered while classifying patients not younger than 50 years. Nevertheless, those classification criteria were slightly modified later [23], specifying the femoral neck as the reference site and accommodating them to men and non-white women as well.

Although osteoporotic clinical diagnosis relies on BMD quantitative assessment, it must not be forgotten that the real clinical significance of the pathology lies in the fractures it causes. The aim of the treatment is then the decrease of the risk of fracture, which, therefore, requires to be assessed reliably so that the intervention is worthwhile. Although bone tissue material properties, affected by the composition of both the mineral and organic matrices, do impact on the amount of stress required to cause fracture, [20], there is still a limited awareness of the best ways to

Table 1.2: Osteoporosis diagnostic criteria based on T-score.

Category	**T-score-based definition**
Normal	Tscore>-1
Osteopenia	-2.5<T-score<-1
Osteoporosis	T-score<-2.5
Severe Osteporosis	T-score<-2.5 in presence of fragility fracture

effectively predict fractures and of the best time to start therapeutic intervention for preventive purposes. BMD measurement can provide clinicians with a relative estimate of the risk of fracture, but there is consistent evidence that, in spite of the increased low-trauma fractures and decreased bone density with older age, the majority of the patients suffering from low-trauma fractures are not classified as osteoporotic according to T-score [24, 25]. On top of that, changes in BMD following pharmacological intervention have been demonstrated to explain only a small proportion of the variance found in the reduction of the fracture risk [26, 27]. Low bone mass is recognized to be an important component of the risk of fracture, although other skeletal and non-skeletal factors do contribute to skeletal fragility as well [12]. Currently, although T-score does represent a threshold for diagnosis, it is not accepted as the unique threshold for pharmacological intervention. Italian guidelines nevertheless, recommend intervention in subjects with rather high fracture risk, specifying treatment might not be usually justified in patients with T-score higher than -2.5 [7]. Actually, besides BMD, a number of purely clinical risk factors operating independently of BMD have been identified. Age, low BMI, the presence of prior fractures, smoking, use of glucocorticoids, alcohol intake, increased probability of falling due to age, addressed as clinical

risk factors, have been contemplated in clinics as able to support the risk of fracture prediction, integrating T-score-derived information. From this perspective, with the purpose of overcoming BMD and related T-score limitations, a fracture risk assessment tool (FRAX) was developed [23], which computes the 10-year probability of a major osteoporotic fracture combining together the BMD measurement at the femoral neck with the afore-mentioned clinical risk factors in order to identify the patients at greater risk and assist treatment decisions. Yet, a considerable part of the patients facing a hip fracture are not considered at high risk even when BMD information is combined with epidemiological models such as FRAX [28], which would suggest the need to find more accurate practices to estimate fracture risk.

Besides purely clinical risk factors, geometry as well as quality and distribution of bone mass do play a pivotal role in determining the overall bone strength; hence, with the aim to overcome T-score limitations taking them into account, DXA softwares have recently been integrated with tools which work on the conventional DXA scans, such as the Hip Structural Analysis (HSA) and Trabecular Bone Score (TBS). HSA method, widely used due to the possibility to easily estimate geometrical and structural variables from hip DXA, expresses the mineral data at particular bone regions in geometric terms, thus providing a number of proximal femur geometrical descriptors. TBS, on the other hand, provides additional information about the trabecular microarchitecture quality through one parameter obtainable from a vertebral DXA image, processed analysing the pixel intensity variations throughout it. Although many studies have focused on investigating their role in supporting T-score within the absolute risk of fracture defnition [29–34], they currently do not find any clear clinical role yet, despite being already in hands of clinicians. HSA, in particular, is inherently limited by the single plane nature of DXA, therefore not being fully able to reflect bone strength. Moreover, HSA geometrical variables are discrete representation of the proximal femur morphology, and many of them result to be cross-correlated [35]. In 2019, nonetheless,

the TBS and Hip Axis Length (HAL) as an HSA geometric parameter were claimed to be associated with the risk of fracture by The International Society of Clinical Densitometry (*International Society of Clinical Densitometry official positions*: https://www.iscd.org/official-positions/2019-iscd-official-positions-adult/), which would seem to more strongly legitimize their employment in clinics.

In the last decades then, Finite Element (FE) models have been thoroughly investigated as potential fracture risk and strength predictors, due to the possibility to accurately integrate patient-specific geometry, a variety of loading conditions and heterogeneous patient-specific material properties extracted from clinical images for accurate and comprehensive structural analyses [36–41]. Since the first model described in literature, in 1985 [42], efforts have been spent especially in developing models from Quantitative Computed Tomography (QCT) images, aiming to non-invasively assess bone strength [28]. Today, bone FE models can be considered able to predict bone strenght with excellent accuracy compared to DXA-BMD [42], and the combination of the two within the diagnostic procedure appears definitely promising. Although they cannot be regarded as cost-effective as hip fracture risk predictors [28] yet, the use of patient-specific FE-based investigations has gained such relevance in the field, that they were contemplated already in 2015 within The International Society for Clinical Densitometry official positions (https://www.iscd.org/official-positions/2015-iscd-official-positions-adult/). Therein, it was stated that femoral or vertebral strength as estimated from QCT-based FE analyses could be used to initiate pharmacological treatment in conjunction with validated thresholds and other clinical risk factors, as well as to monitor age- and treatment-related changes.
Since the use of FE analyses for fracture risk estimation purposes will be the main focus of the two following chapters, a more in-depth literature analysis and description of their applications will be provided therein.

1.4 Hip fractures

In the overall context of osteoporotic fractures, hip fractures are commonly given particular attention due to the considerable impact and serious aftermaths they entail. Among all osteoporotic fractures, they turn out to be the most detrimental in terms of mortality rate, decreased mobility, quality of life, loss of independence [43, 44] and, therefore, the global costs for the healthcare systems. In 2017, in Italy, the costs associated to fragility fractures amounted to €9.4 billion and between €5.5 and €6 billion were hip fractures-related costs (*2018 country-specific report on the clinical, societal, and cost burden associated with fragility fractures*: http://www.panoramasanita.it/wp-content/uploads/2018/10/report-firmo-iof.pdf).
Hip fractures are generally classified based on the location where they take place: in the first instance, intracapsular and extracapsular fractures are distinguished. Intracapsular fractures basically occur at the femoral neck, although a further classification within them can be made (Figure 1.7). Extracapsular fractures, on the other hand, can occur either at the intertrochanteric, trochanteric, or subtrochanteric region, as shown in Figure 1.7.

Due to the age-related increased probability of falling, the majority of hip fractures result from falls, more often from standing, and sideways falls would seem responsible for a huge percentage of hip fractures, contributing to about 95% of all hip fracture cases [45]. Considering the combination of bending and axial compression involved, fall-related impact on the proximal femur represents a particularly critical condition [46, 47]. In addition, during a fall, the bone experiences impact loads which result completely different from those usually experienced during walking or climbing stairs (Figure 1.8) [48].

Clinically, as already mentioned, the primary screening to determine the potential hip fracture risk in the elderly is the assessment of the osteoporosis status based on the BMD measurement. When performing DXA

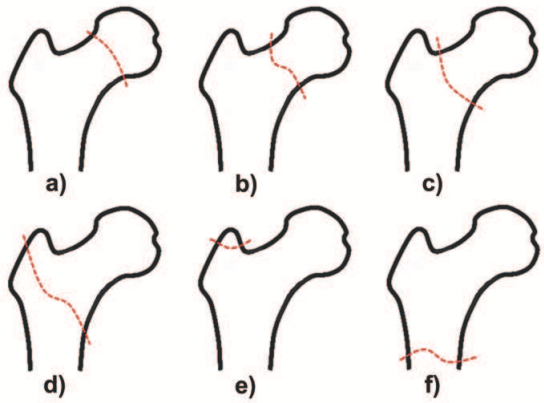

Figure 1.7: Intracapsular (top) and extracapsular (bottom) femur fractures. Intracapsular fractures can be further divided in subcapital (a), cervical (b) and basicervical (c), while extracapsular fractures can be intertrochnateric (d), trochanteric (e) or subtrochanteric (f).

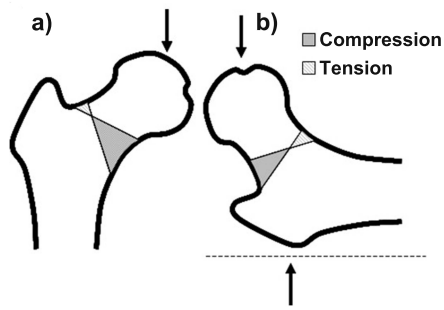

Figure 1.8: Different tensional states at the femoral neck resulting from walking (a) or falling on the side (b). From [48].

at the proximal femur, the BMD is provided at different specific regions of interest, i.e. the femoral neck, the trochanter, the intertrochanter, Ward's triangle and total femur, which includes all the previous ones. It is mainly on the neck and total femur BMD measurements that the WHO has defined the presence of osteoporosis, although currently the BMD is known to explain only partially the occurrence of fractures [49, 50]. From this

perspective, the role of HSA parameters has been explored to better clarify their role as supportive hip fracture risk predictors [20, 30, 51, 52]. HSA tries indeed to exploit DXA data in order to express mineral mass in mechanically meaningful terms rather than in density only [20]. As a matter of fact, long bones are mainly loaded in bending and axial compression, and HSA provides estimates of the bone cross-sectional area, on which the axial component of stress depends, as well as the cross-sectional moment of inertia, indicator of the bone mass distribution with respect to the center of mass, which controls the bending stress.

There are three different Regions Of Interest (ROIs) where the various

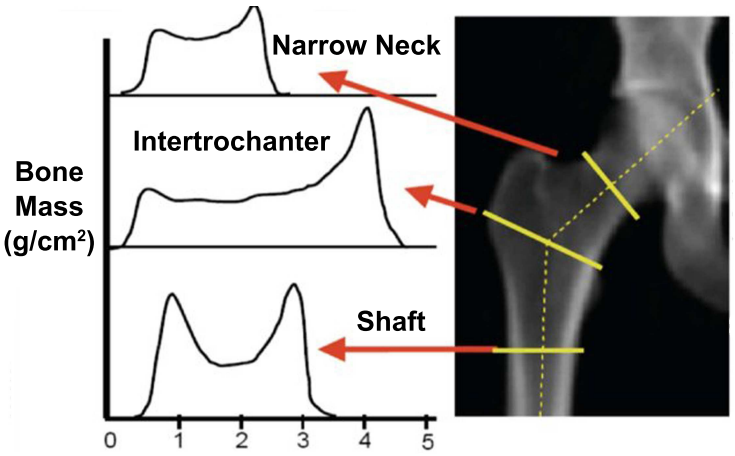

Figure 1.9: The three ROIs where HSA parameters are extracted: Narrow Neck, Intertrochanter, Shaft. From [53].

HSA parameters are extracted [53], which are all 5 mm wide: the Narrow Neck (NN), located at the narrowest portion of the femoral neck, the Intertrochanter (IT), at the intersection between neck and shaft axes, the Shaft (S), placed distally with respect to the afore-mentioned intersection by 1.5 times the femoral neck width (Figure 1.9). Whereas the NN and IT regions are considered both cortical and trabecular ROIs, the Shaft region is considered to be cortical only. A brief summary of the main HSA

variables is provided in Table 1.3.

Table 1.3: The main HSA variables cited in the literature and mainly used in this study. From [53].
CSA: Cross Sectional Area; CSMI: Cross-Sectional Moment of Inertia; W: Width; ED: Endocortical Diameter; CT: Cortical Thickness; Z: Section Modulus; BR: Buckling Ratio.

HSA Variable	**Variable Description**
NSA (°)	Angle between neck and shaft axes
HAL (cm)	Distance from pelvic brim to outer margin of greater trochanter along neck axis
Variables calculated either at NN, IT or S	
BMD (g/cm^2)	The Bone Mineral Density, calculated as $(\frac{CSA}{W}) * 1.05$ [54]
CSA (cm^2)	The total mineralized bone area in the cross section
CSMI (cm^4)	Index of structural rigidity, computed as the integral of the bone density within a pixel times the square of its distance from the area center of mass
W (cm)	The outer diameter computed as the width of the mass profile
ED (cm)	Estimate of the inside diameter of the cortex
CT (cm)	The mean cortical thickness
Z (cm^3)	Indicator of bending strength, calculated as the ratio between CSMI and maximum distance from center of mass to outer cortex
BR	The relative thickness of the cortex as an estimate of cortical stability in buckling, computed as the ratio between the maximum distance from center of mass to outer cortex and the average cortical thickness.

1.5 Aim of the Thesis project

In the previous sections the urgent need to enhance the fracture risk prediction in osteoporotic cohorts has been underlined. Especially in western countries, where the population is increasingly greying, osteoporotic fractures in general, with hip fractures playing an important role among

them, have become a social and economic burden. The limitations of the BMD-based T-score have been largely proven, and aiming to overcome them, great efforts have been spent by researchers in the field.
QCT-based FE analyses, able to combine patient-specific geometry and material properties, were proved to achieve optimal accuracy levels in terms of patient-specific geometry and material properties. However, CT is not, at present, included within the standard clinical process which is adopted for osteoporosis diagnosis purposes. It would indeed subject the patients to an increased radiation dose compared to the gold-standard DXA and, above all, would entail increased costs for the healthcare systems.
Therefore, attention has been paid to the femur geometric features, knowing the shape, together with the material properties, represents a determinant of the strength of a structure. From this perspective, HSA allows the extraction of a number of discrete geometric variables from DXA images. Hence, due to their easy extraction and already feasible application, they have been extensively investigated, mostly in retrospective cohorts, as fracture risk predictors. Nevertheless, results are often contrasting and a clear consensus has not yet been achieved.

With this in mind, this thesis represents an attempt to get deeper insights in the role geometry might play in determining the risk of fracture, simultaneously exploring possible ways to enhance the current gold-standard.
This could not be done retrospectively, but rather involved, taking advantage of the simultaneous availability of CT and DXA images for the same set of patients, the performance of CT- and DXA-based Finite Element analyses. The ambition was to relatively estimate the fracture risk level for the available cohort, aiming, on one hand, to identify attainable fracture risk predictors to be integrated in the clinical diagnostic process supporting the T-score; on the other hand, to propose tools which, taking advantage of larger cohorts with follow-up information, might help in more consistently interpreting the role of geometry.

Chapter 2

3D Finite Element modelling for hip fracture prediction: a HSA-Based Model

This chapter is partially based on the publication:

Aldieri, A., Terzini, M., Osella, G., Priola, A.M., Angeli, A., Veltri, A., Audenino, A.L. and Bignardi, C.

'Osteoporotic hip fracture prediction: is T-score-based criterion enough? A hip structural analysis-based model'

in *Journal of Biomechanical Engineering*, 140(1), 111004, 2018.

Abstract

The current gold-standard for osteoporosis diagnosis is based on Bone Mineral Density (BMD) measurement, which, however, has been demonstrated to poorly predict fracture. Further parameters in the hands of the clinicians are represented by the Hip Structural Analysis (HSA) variables, geometric descriptors of the proximal femur cross-section. The purpose of this study was to investigate the suitability of HSA parameters as additional hip fracture risk predictors. With this aim, twenty-eight three-dimensional patient-specific models of the proximal femur were built from Computed Tomography (CT) images and a sideways fall condition was reproduced by Finite Element analyses. A Risk Factor Index (RFI) and Femoral Strength (FS) were calculated based on principal strains fracture criteria. The power of HSA variables combinations to predict the RFI and FS values was assessed by multivariate linear regression analyses. The optimal regression models, identified through the Akaike information criterion, comprises the buckling ratio at the narrow neck and femoral shaft, the cross-sectional moment of inertia at the narrow neck and the neck-shaft angle. The models were tested on two additional patients who suffered a hip fracture after a fall. The results highlighted them as at an higher risk level, supporting the prediction power of the adopted approach.

2.1 Introduction

In view of the DXA-BMD and T-score limitations in accurately estimating the proximal femur fracture risk, three-dimensional Finite Element (FE) modelling approaches have thoroughly been adopted and investigated [41, 55]. The proximal femur has indeed gained exceptional consideration in the scientific literature given that hip fractures are recognised as the most severe type of osteoporotic fracture [56]. As a matter of fact, FE models built from clinical images are able to include most of the bone strength determinants, integrating patient-specific mechanical properties, anatomical features as well as the possibility to examine a variety of loading conditions, which is the reason why they have been employed for fracture risk and fracture load estimation. Stance [57–60] and fall [60–63] configurations have principally been studied, with particular attention to falls, which are the major cause of hip fracture [45]. Potentially, three-dimensional (Quantitative) Computed Tomography (CT)-based FE models could be considered extremely accurate and reliable fracture risk estimators. From this perspective, FE models employed for fracture load prediction and compared to corresponding *in vitro* experiments reported much more accurate estimations with respect to any density-based evaluation [64]. QCT-based FE models were also demonstrated to be 6-7 pp more accurate than T-score in the femoral strength prediction as well as in the classification of patients as fractured or non-fractured [28]. Having said that, the application of CT-based FE in a clinical and thus in an *in vivo* setting remains challenging. First of all, their direct application within the clinical decision process has not yet been demonstrated to be cost-effective [28]: three-dimensional FE models development requires indeed CT, more expensive and time-consuming than DXA; besides, different methodological choices and modelling assumptions could potentially affect the final FE models accuracy [64].

Having this in mind, the main purpose of the work presented in this first chapter was the identification of the Hip Structural Analysis (HSA)

parameters best related to the strength and fracture risk as identified from CT-based FE models. In other words, FE analyses outcomes were used to investigate the predictive capabilities of the already available clinical data, in order to identify and, in case, provide, additional geometric predictors for the estimation of hip fracture risk.

2.2 Materials and Methods

2.2.1 Subject-specific FE model construction

Twenty-eight post-menopausal female subjects, aged from 55 to 81 years (treated in San Luigi Gonzaga Hospital in Orbassano, Italy), were involved in the present study after having signed an informed consent. Patients affected by cancer were excluded due to the possible presence of bone metastasis, which would have affected bone strength. By means of cross checks in the Hospital database, only patients with available clinical data, DXA derived information (Discovery DXA system, Hologic, Waltham, MA, USA), and CT scans (Brilliance 64, Philips, Amsterdam, Netherlands) acquired in the same year were selected. Since the sourced CT scans were not prescribed for osteoporosis diagnosis purposes, only the proximal portion of the femur was included, and only patients whose femur was clearly visible in the CT scans were included in the study. CT slices thickness was 2 mm, and the pixel width was 0.6857 mm.

Three-dimensional subject-specific geometric models of the proximal femur were built (Figure 2.1) through a semi-automatic segmentation procedure (Mimics, v17, Materialise, Leuven, Belgium) on the CT images based on Hounsfield Units (HU). Subsequently, all 3D models were cut 2.5 cm below the midpoint of the lesser trochanter.

Once the CT-based geometric models construction was accomplished, a sensitivity analysis was carried out on FE mesh elements dimensions prior to the heterogeneous HU-based material properties assignment, in order to assess the mesh density required to achieve sufficiently accurate results.

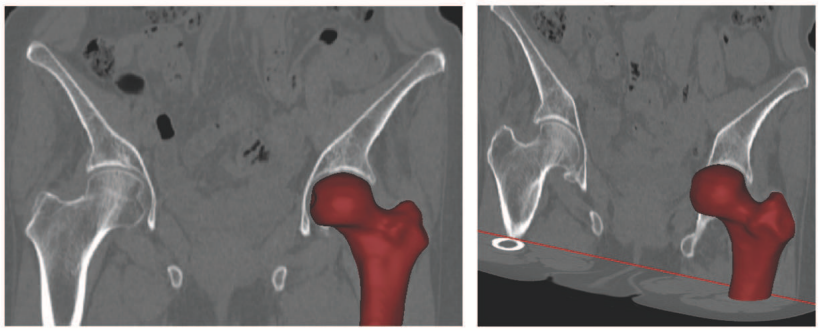

Figure 2.1: One example of geometric model of the proximal femur built from CT images.

One available patient-specific three-dimensional model was thus meshed with ten-nodes tetrahedral elements (C3D10 Abaqus elements) with decreasing edge dimensions of 3, 2, 1.2, 1, 0.8 mm (Figure 2.2). Subsequently,

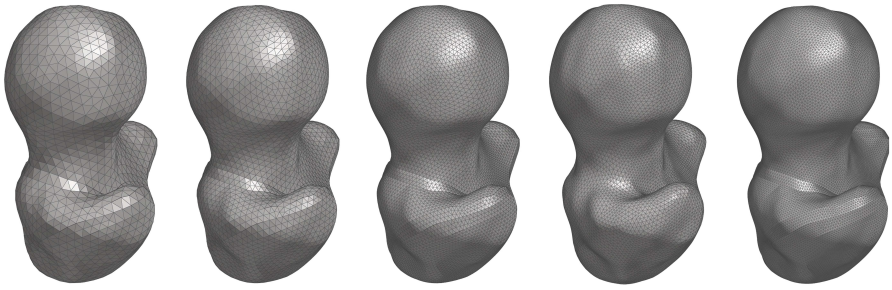

Figure 2.2: Different mesh dimensions tested within the sensitivity analysis. From left to right the elements edge length decreases from 3 mm to 2, 1.2, 1, 0.8 mm.

after aligning the proximal femur according to its anatomical reference system, defined on neck and shaft axes, simplified boundary conditions were applied to simulate a fall on the side, as exemplified in Figure 2.3. Briefly, the load was applied on the greater trochanter, head nodes were restrained along the impact load direction and the distal nodes connected to a hinge. These boundary conditions were applied in accordance with a number of experimental [48, 65, 66] and coupled experimental-computational [60, 61,

63, 67] studies investigating the resistance and failure of the proximal femur during a sideways fall. Aiming to investigate the effect of elements size, the models were assigned a uniform isotropic elastic modulus of 15 GPa and a Poisson's ratio of 0.3. Mesh sensitivity analysis was based

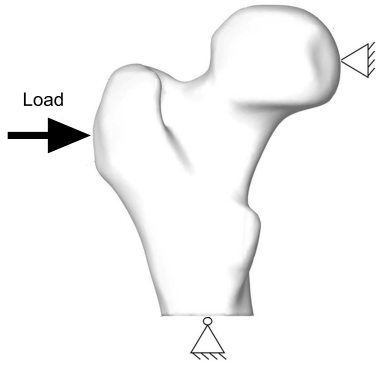

Figure 2.3: Boundary conditions employed to carry out the mesh dimensions sensitivity analysis.

on minimum (or compressive) and maximum (or tensile) principal strains extracted at the neck region. For each mesh, the highest tensile principal strain and the lowest compressive principal strain were extracted at the neck and the corresponding error with respect to the finest mesh computed. With an error lower than 3% (Figure 2.4), accounting for the required computational cost as well, the 1.2 mm edge length mesh was judged sufficiently accurate and therefore selected to mesh all the models, being in accordance to mesh dimensions adopted in similar studies too [68, 69].

Subsequently, heterogeneous material properties were mapped onto the FE models. An elastic bone mechanical response was assumed, since proximal femur was observed to behave elastically until the onset of a fracture [70] and the study did not want to focus on damage progression. The elastic modulus was determined based on a density-elasticity relationship

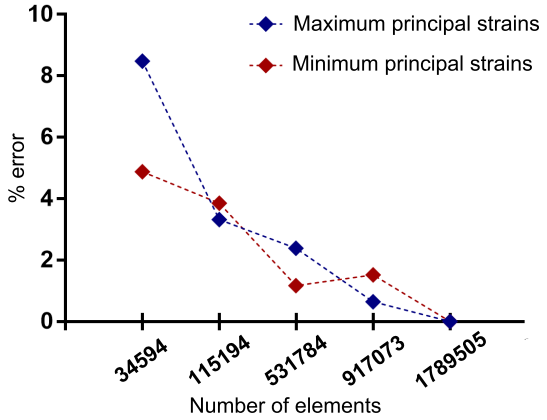

Figure 2.4: Mesh dimensions sensitivity analysis: % error for tensile and compressive principal strains computed with respect to the most refined mesh (0.8 mm edge length).

[71] which has been shown to yield accurate strain predictions [69, 72, 73]:

$$E = 15.010\,\rho_{app}^{2.18},\ if\ \rho_{app} \leq 0.28\,g/cm^3 \tag{2.1}$$

$$E = 6.850\,\rho_{app}^{1.49},\ if\ \rho_{app} > 0.28\,g/cm^3, \tag{2.2}$$

where E is the Young's modulus, expressed in GPa, and ρ_{app} is the apparent density, computed from CT-derived HU values, in g/cm^3.
Without the possibility to properly calibrate the available CT images, a pseudo-calibration was performed [74], aiming to estimate the linear relation between HU and apparent density (ρ_{app}), needed to calculate the relative Young's modulus values (Equations 2.1, 2.2). The maximum cortical bone density was assumed to be about $2\,g/cm^3$ [75], corresponding to the average highest HU value found in the cortical bone (found to be 1200 HU). At the lowest end, the density of $0\,g/cm^3$ was assigned to bone marrow, and the equivalent average lowest HU value detected to be -140 HU.

In order to assign HU-based inhomogeneous material properties, mesh elements had to be divided in groups, or bins, based on their HU value. Hence, an average HU value for each mesh element was first identified; then, the global elements HU span was divided into a discrete number of intervals, in order that each element could be assigned to a specific interval on the basis of its own HU value. For each interval, the central HU was identified and a Young's modulus (E) value evaluated from it. In this way, each HU interval represented a material group, where the elements shared a common elastic modulus (E) value based on the interval central HU value. Aiming to assess the minimum number of HU bins for the heterogeneous material properties assignment leading to accurate results, a further sensitivity analysis was carried out. Highest tensile and lowest compressive principal strains were considered, with the percentage errors computed with respect to the output obtained with the highest number of bins (i.e. 60 bins). With an error inferior to 5% (Figure 2.5), the HU range partition into 40 different intervals was judged sufficiently accurate for the inhomogeneous material properties assignment.

The global HU range of the CT images was then divided into 40 different

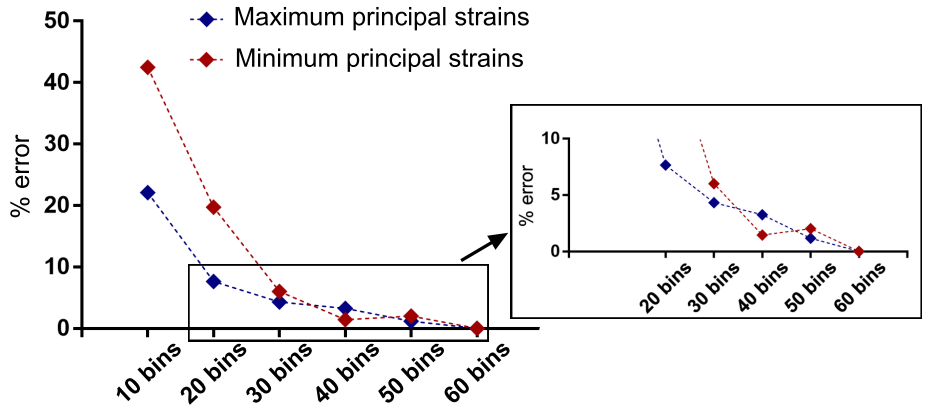

Figure 2.5: Material bins sensitivity analysis: % error for tensile and compressive principal strains computed with respect to the 60 bins-based material properties assignment.

bins, and the bin-specific Young's modulus computed starting from the bin central HU value. On the basis of its average HU, each element was allocated to one specific bin and assigned with the corresponding E.

2.2.2 FE analyses generation

Static FE simulations were performed in Abaqus (v13, Simulia, Dassault Systèmes, Rhode Island, U.S.), aiming to reproduce a sideways fall condition, the most frequent cause of a femur fracture in the elderly [45].

Two different spatial configurations of the proximal femurs were investigated. The former one, a reference configuration to some extent, was achieved aligning the femurs with respect to the anatomical reference system defined by neck and shaft axes. Besides, by means of a simultaneous 30° posterior (α) and 15° medial (β) rotation with respect to the neck and shaft axis respectively, a tilted configuration was obtained (Figure 2.6) [63, 72, 76]. The two different configurations were simulated applying the same boundary conditions (Figure 2.7). The impact load was applied on the trochanter as a distributed force in the x direction, while the head nodes, in order to consider acetabular cartilage effect, were bound to the ground by means of spring elements with a 10000 $\frac{N}{mm}$ stiffness [77, 78] along both the load and the in-plane orthogonal directions, aiming to let a static displacement. Although head nodes are usually constrained during FE analyses, the use of spring elements was coherent with experimental studies where head cartilage was taken into account [65, 104]. The distal nodes of the proximal femur models were connected through link elements to a reference node positioned 0.1 m distally [60, 61, 63], having all the translational degrees of freedom fixed. Although the lack of experimental tests here prevented the direct validation of the employed boundary conditions, they were adopted in accordance with validated studies [60, 61, 63, 67].

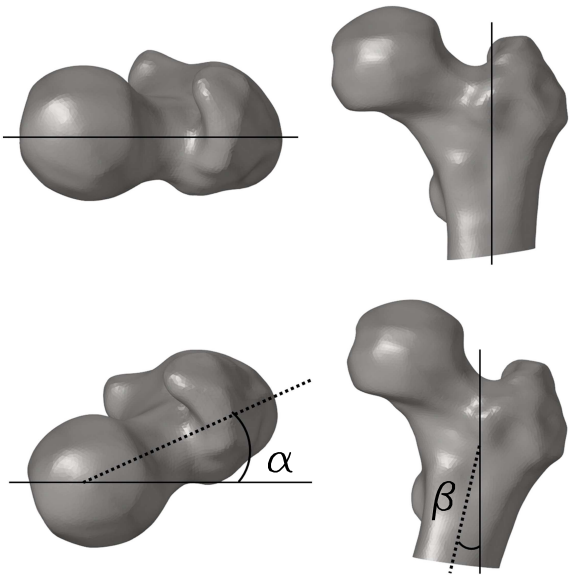

Figure 2.6: The two different configurations explored from the axial (left) and coronal (right) view. First row: the reference configuration; second row: the tilted configuration.

2.2.3 FS and RFI estimates

Within the post-processing phase, principal strains represented the main variable of interest, in accordance with a large number of similar studies where maximum principal strain criteria for fracture prediction were adopted and validated [40, 57, 60, 69, 80, 81].
For each element, the minimum (ε_1) and maximum (ε_3) principal strains were extracted at the centroid; in agreement with a validated procedure [60, 69], by comparing their absolute values, a compressive or tensile predominance was assessed and a Risk Factor (RF) could be calculated at each mesh element as:

$$RF = \frac{\varepsilon_{max}}{\varepsilon_{lim}}, \tag{2.3}$$

where ε_{max} refers to the selected tensile or compressive principal strain value ($\varepsilon_{max} = max(|\varepsilon_1|, \varepsilon_3)$), and ε_{lim} represents the compressive or tensile

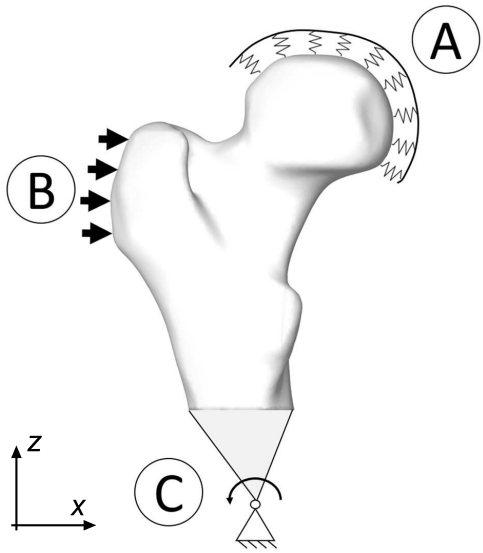

Figure 2.7: Boundary conditions applied to reproduce the sideways fall. A) head nodes were bound to the ground through spring elements with $10000\frac{N}{mm}$ stiffness; B) impact load was applied as a distributed force on the trochanteric surface; C) distal nodes of the proximal femur were connected to a spherical joint placed 0.1 m distally by means of link elements. From [79].

limit value (0.0074 in tension, 0.0104 in compression) [82]. In particular, because according to experimental evidences fracture propagates from the external cortex [48, 60, 69], only superficial elements were considered.
Two different fracture risk predictors were measured based on principal strains: the Femoral Strength (FS) and the Risk Factor Index (RFI).
The FS, i.e. the maximum force the femur can sustain until the onset of a fracture, was estimated linearly increasing the impact load up to the onset of the fracture was hypothesized to occur. Specifically, fracture initiation was assumed when the number of contiguous elements in the outer cortex with a RF bigger than 1 exceeded 0.3% (adapted from [60]) of the total surface elements. At each load increment (200 N), the RF was extracted

for the cortex elements, and elements contiguity recognized when the distance between their centroids was lower than 1.5 mm.
The RFI on the other hand, the ratio of the highest tensile or compressive principal strain to the corresponding threshold limit, was simply derived as the highest RF found in the bone outer cortex at a patient-specific impact load, dependent on patients' mass and height. Subject-specific values of the impact load were assessed implementing an equivalent 1 Degree of Freedom mass-spring-damper dynamic system (Figure 2.8) in Simulink (Matlab v2107b, The MathWorks, Massachusetts, U.S.) to simulate a sideways impact from standing [83]. The system mass value was

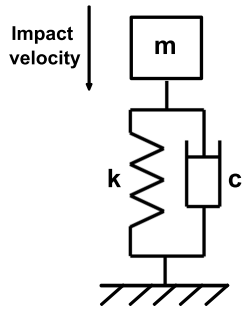

Figure 2.8: The 1 Degree Of Freedom model used to determine the patient-specific impact load. Mass and impact velocity were assigned patient-specifically, while the stiffness (k) and damping coefficient (c) were kept constant.

assigned specifically for each patient, while the spring and damper values, accounting for trochanteric soft tissues, were kept constant for all and determined according to [84–86]. Specifically, experimental data contained in [84] and extracted from trochanteric soft tissues harvested from cadavers of elderly individuals (77 ± 10 years), allowed the estimation of the stiffness and damping as 30 $\frac{kN}{m}$ and 300 $\frac{N\,s}{m}$, which found agreement with [83, 87]. As regards the impact velocity, it was computed integrating the patient-specific height in a two-link kinematic model [88]: the body was simplistically seen as a two-link model, modelling legs and trunk as two uniform slender bars connected with a frictionless hinge located at the hip

[88]. Employing energy conservation and a 45° Jack-knife configuration, the impact velocity just before the impact resulted in $2.72\sqrt{h}$ (see [88] for further details on how it was derived), with h being the total body height (in meters). The average impact velocity was $3.39\,m/s$, with $0.084\,m/s$ standard deviation. From the dynamic load output by Simulink, the value of the first peak was identified as the impact load to be applied on greater trochanter surface for the RFI extraction.
The FS and RFI were computed with the femur in the neutral orientation (FS_n and RFI_n) and in the inclined one (FS_i and RFI_i). Eventually, the most critical values for each patient were identified [89], which will be addressed as FS and RFI:

$$FS = min(FS_n, FS_i) \tag{2.4}$$

$$RFI = max(RFI_n, RFI_i). \tag{2.5}$$

2.2.4 Assessment of HSA variables as fracture predictors

As previously explained, the HSA program, based on DXA images, employs the mineral mass distribution along a line of pixels arranged on the proximal femur cross-section at particular locations to extrapolate geometrical and structural descriptors essentially based on the X-ray attenuation profile [90]. Because bone geometry represents a determinant of bone strength and structural properties of the proximal femur can be estimated through HSA from routine DXA scans, HSA variables role has been widely investigated [51, 91]. The HSA variables considered for this study were represented by the Bone Mineral Density (BMD), the average cortical thickness (CT), the Buckling Ratio (BR), the Cross-Sectional Moment of Inertia (CSMI), the Cross-Sectional Area (CSA), the Width (W) of the considered bone site (Figure 2.9). A summarizing descriptive table for these variables was provided and is available in the introductive Chapter (Table 1.3). These measures were all available at the three aforementioned locations: the narrow neck (nn) region, the intertrochanteric

(it) region, the femoral shaft (fs) region (Figure 2.9). Besides, the Hip Axis Length (HAL) and the Neck Shaft Angle (NSA), available as additional HSA parameters (Figure 2.9), were used within this post-processing phase as well. Because some of these HSA variables were presumably cross-correlated, being extracted from the same mineral mass distribution provided by DXA, a collinearity diagnosis was carried out and the Variance Inflation Factor (VIF) computed for each variable [92]. The VIF can be computed for each i^{th} variable of interest as:

$$VIF_i = \frac{1}{1 - R_i^2}, \tag{2.6}$$

where R_i^2 is the coefficient of determination derived regressing the i^{th} variable on the other ones. An high VIF is then the evidence of the presence of collinearity. Although usually a VIF>30 is considered of concern, HSA variables showing a VIF>100 were rejected in the first place, so that all but 8 HSA variables were kept out because judged collinear. The VIF was then recomputed on the 8 remaining ones: all exhibiting a VIF<10, they were not considered to be collinear and thus kept for the regression models construction. The 8 non-collinear variables kept for the subsequent regression analysis are presented for the entire cohort included in this study in Table 2.1.

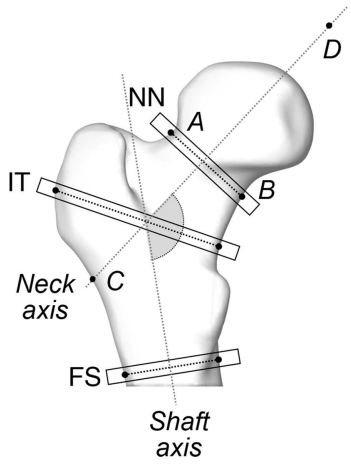

Figure 2.9: Overview of the anatomical sites (narrow neck (nn), intertrochanter (it), femoral shaft (fs)) on which the HSA method is performed. Some HSA parameters are highlighted. AB: width (W) at the NN site; CD: Hip Axis Length (HAL) identified on the neck axis between points D (which represents the pelvic brim) and C (the outer margin of the greater trochanter); the Neck Shaft Angle (NSA) is highlighted in grey, between the neck and shaft axes. From [79].

Table 2.1: Independent HSA variables used for the regression models construction for the whole cohort included. Patients 29 & 30 are two additional fractured ones, for whom CT was not available. They were recorder to have fractured following a fall at home within 1 year from the DXA. nn: narrow neck; it: intertrochanter; fs: femoral shaft; BR: Buckling Ratio; CSMI: Cross-Sectional Moment of Inertia; W: Width.

			nn		**it**			**fs**
Pat.	**NSA** (°)	**HAL** (mm)	**BR**	**CSMI** (mm^4)	**BR**	**CSMI** (mm^4)	**W** (mm)	**BR**
P1	124.63	95	10.53	2.20	9.43	9.92	5.29	3.62
P2	138.35	106	22.76	1.69	13.37	7.29	5.48	5.89
P3	113.91	108	12.66	2.44	8.49	8.69	5.04	2.83
P4	115.9	85	19.49	3.18	11.70	9.07	6.12	2.37
P5	124	101	11.90	1.60	8.87	12	5.21	4.71
P6	120.47	88	19.21	1.17	16.09	4.83	5.03	4.06
P7	128.10	92	6.42	1.55	6.29	8.22	4.70	1.92
P8	122.80	108	12.42	2.41	9.54	14.21	5.72	3.04
P9	123.21	107	12.12	3.20	10.91	13.91	5.93	3.53
P10	122.58	95	10.97	1.78	8.22	13.28	5.59	3.40

P11	123.39	107	12.69	2.87	11.11	18.06	6.21	4.02
P12	128.52	107	15.63	1.91	10.15	12.95	5.67	3.08
P13	126.19	120	22.49	2.85	14.57	13.58	6.09	5.04
P14	121.18	95	7.93	3.04	9.36	10.7	5.41	2.32
P15	123.36	105	14.96	1.96	13.90	8.68	5.43	5.49
P16	116.55	92	10.76	2.13	7.64	21.52	6.10	2.73
P17	115.82	107	12.33	2.39	10.25	14.21	5.61	4.51
P18	123.76	109	15.84	2.09	12.51	15.43	6.31	3.95
P19	129.94	108	10.23	3.11	8.32	18.01	5.88	2.65
P20	122.68	97	11.27	2.39	9.09	12.76	5.36	3.98
P21	132.62	91	10.61	1.42	7.41	7.46	4.96	1.46
P22	124.14	108	16.17	1.89	10.89	14.66	5.98	4.11
P23	124.17	102	13.57	1.92	11.61	9.46	5.25	3.75
P24	126.7	99	12.73	2.34	8.42	13.80	5.67	3.25
P25	124.37	103	14.01	1.49	12.59	9.47	5.42	5.69
P26	127.49	107	14.24	1.92	13.19	10.31	5.93	4.86
P27	129.47	102	11.52	4.69	8.05	17.90	6.01	2.10
P28	127.48	96	17.21	1.70	13.54	7.79	5.29	4.49
P29	117	87	17.70	2.44	9.70	4.51	6.34	2.80
P30	123	103	19.90	2.28	16.30	3.32	6	5.37

Aiming to understand the HSA most relevant to both the FS and RFI, taken as dependent variables y once at a time, different multivariate linear regression models were built from combinations of all the available HSA variables (x), taken as predictors of the dependent variable y (the FS and RFI) according to the relationship:

$$y = \beta_0 + \sum_i \beta_i \, x_i \tag{2.7}$$

where β_0 and β_i are the regression coefficients and x_i represents the i^{th} independent HSA variable. For each dependent variable, a total of 238 models were computed, considering all the possible combinations of the 8 independent variables gathered in groups containing from 2 to 6 elements. The computed models were ranked on the basis of the Akaike information criterion (AIC) [93].

The Akaike's Information Criterion (AIC) measures the relative goodness of fit of a model. Based on the maximum value of the likelihood function of the model (l), the AIC allows to estimate the information lost when approximating reality, in order to select, from a set of models, the best one, which minimizes the loss of information. The rationale behind the model selection process is the principle of parsimony: although a fit improvement can be obtained by adding parameters to a model, this will cause the information in the data to be split over an higher number of parameters. Hence, the criterion includes a penalty term which represents an increasing function of the number of regressor variables. Therefore, the AIC for a given model is a function of its maximized likelihood function (l) and of the number of regressor variables, including the intercept (K):

$$AIC = -2l + 2K \tag{2.8}$$

Under the assumption of normally distributed residuals, l can be estimated as $\frac{n}{2}\, log(\frac{SSE}{n})$, where SSE represents the residual sum of squares of the least square regression and n the sample size. As mentioned before, the second component ($2K$) represents a penalty term that becomes larger as the number of parameters increases and which penalizes the AIC, increasing its value. Therefore, in our work, the combination of HSA variables included within the regression model selected by AIC would be the one with the minimum AIC value. However, AIC is not interpretable by itself, but it becomes valuable when compared with the AIC of a series of models, since it is only able to provide information about the relative quality of a model with respect to other models. The Akaike weights (w_j), on the other hand, computed as the relative likelihood of the model normalized to obtain a positive set of Akaike weights, can provide a measure of the weight of evidence in favour of each model. Akaike [93] suggests that $e^{-0.5\Delta_j}$ approximates the relative likelihood of the model l_j given the data, where $\Delta_j = AIC_j - min(AIC)$ are the AIC differences, evaluated as the difference between the j^{th} AIC and the smallest AIC value among

all the candidate models (i.e. the "best" model). Therefore, the Akaike weights of the j^{th} model in a set of R candidate models can be computed as follows:

$$w_j = \frac{e^{-0.5\,\Delta_j}}{\sum_{r=1}^{R} e^{-0.5\,\Delta_r}}. \tag{2.9}$$

Furthermore, from this perspective, the relative importance of each predictor variables x_i can be assessed by summing the Akaike weights across all the models in the set where variable i occurs, thus obtaining the cumulative Akaike Weights $w_+(i)$. The larger the sum $w_+(i)$, the more important the variable x_i is when compared to the other variables.
In addition to the variables and model ranking based on AIC, the regression models quality was estimated using the adjusted Pearson's correlation coefficient (R^2_{adj}) as well. The predictive ability of the optimal model, characterized by the highest Akaike weight, was assessed exploiting the HSA parameters of two additional post-menopausal patients (aged 71 and 75 years) who experienced hip fracture and for whom DXA data related to the year preceding the fall were available. Hence, lastly, FS and RFI values predicted for the fractured patients were compared to those extracted from the FE models, in order to establish their patient-specific risk level.

2.3 Results

The two main outcomes extracted from the FE analyses, i.e. the RFI and the FS, are compared in Figure 2.10. Although the RFI identification was dependent on a patient-specific impact load determined taking into account the patient-specific mass and height values, they turn out to be quite strongly correlated ($R = 0.83, p < 0.0001$).

As mentioned in the previous section, the RFI and the FS were obtained comparing $\mathrm{RFI_n}$, $\mathrm{RFI_i}$ and $\mathrm{FS_n}$, $\mathrm{FS_i}$, i.e. the corresponding values related to the two different proximal femur configurations explored (neutral and tilted configuration), and taking the most critical values for each

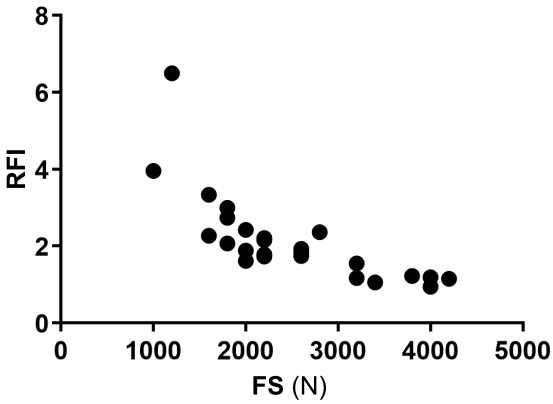

Figure 2.10: Comparison between the FE analyses-based RFI and FS values identified for the 28 patients included in the study.

patient. From this perspective, the comparison between the outcomes of the two analysed configurations in terms of both the RFI and the FS is presented in Figure 2.11. Independently of the considered index (RFI or FS) the outcomes resulting from the two configurations are significantly correlated ($R > 0.7$, $p < 0.0001$). The inclined one, as expected [72], turned out to be the most critical between the two, with higher RFI and lower FS values.

Figures 2.12 and 2.13 show the superficial distribution of the RF for the 28 patients at the load-step when fracture was supposed to occur for the neutral (Figure 2.12) and inclined (Figure 2.13) femur orientations. For visualization purposes, the cell-centered variable is shown as interpolated at the nodes and the RF higher than the 90^{th} percentiles have been depicted, judged evidence of a considerable strain level. Some patients show high RF at the greater trochanter, but that area was not considered while identifying the contiguous failed elements because it might have been affected by the load application. Whereas the neutral configuration caused a more inhomogeneous distribution of the failed area among the patients,

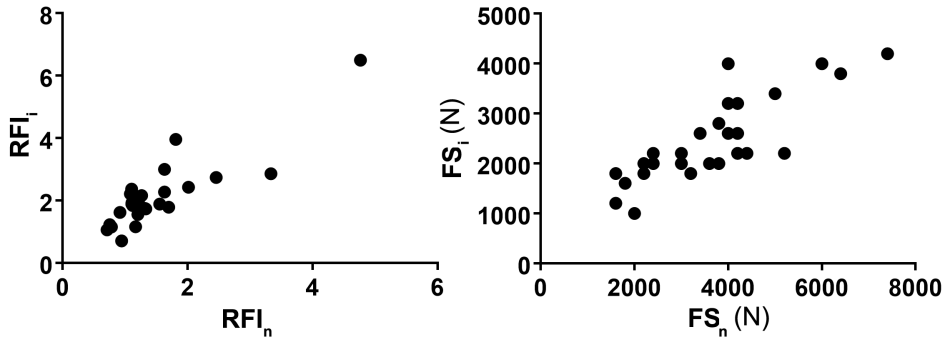

Figure 2.11: RFI (left) and FS (right) values in the neutral and inclined configurations explored through the FE analyses.

in the inclined one it was mostly located posteriorly, where the femur was mainly loaded in compression. To help the reader compare the patients from the perspective of their FS as well, Figure 2.14 offers an overview of the patient-specific FS values as assessed from the FE analyses in the neutral and inclined femur orientation respectively.

Thanks to the AIC-based multivariate linear regression analysis, the most suitable HSA variables for the RFI and FS prediction could be identified. For this purpose, both RFI_n, RFI_i and FS_n, FS_i were considered, with an interest in the most relevant variables in the different cases. The HSA variables included within the best 5 regression models according to the AIC are presented in Tables 2.2 and 2.3. As visible, the AIC-based optimal HSA descriptors were strongly related to the bone resistance to bending, dominant during sideways falls. Nearly all the RFI-based optimal combinations incorporated the NSA, which is known to play a role, affecting the bending moment arm at the neck, together with the BR at the narrrow neck (RFI_i) and femoral shaft (RFI_n). Because in the neutral configuration the impact load was applied along the neck axis, the neck was presumably subjected to a predominant axial compression rather than bending, with the shaft loaded similarly to a fixed beam. On the contrary, in the inclined one, the introduction of an anteversion angle is likely to

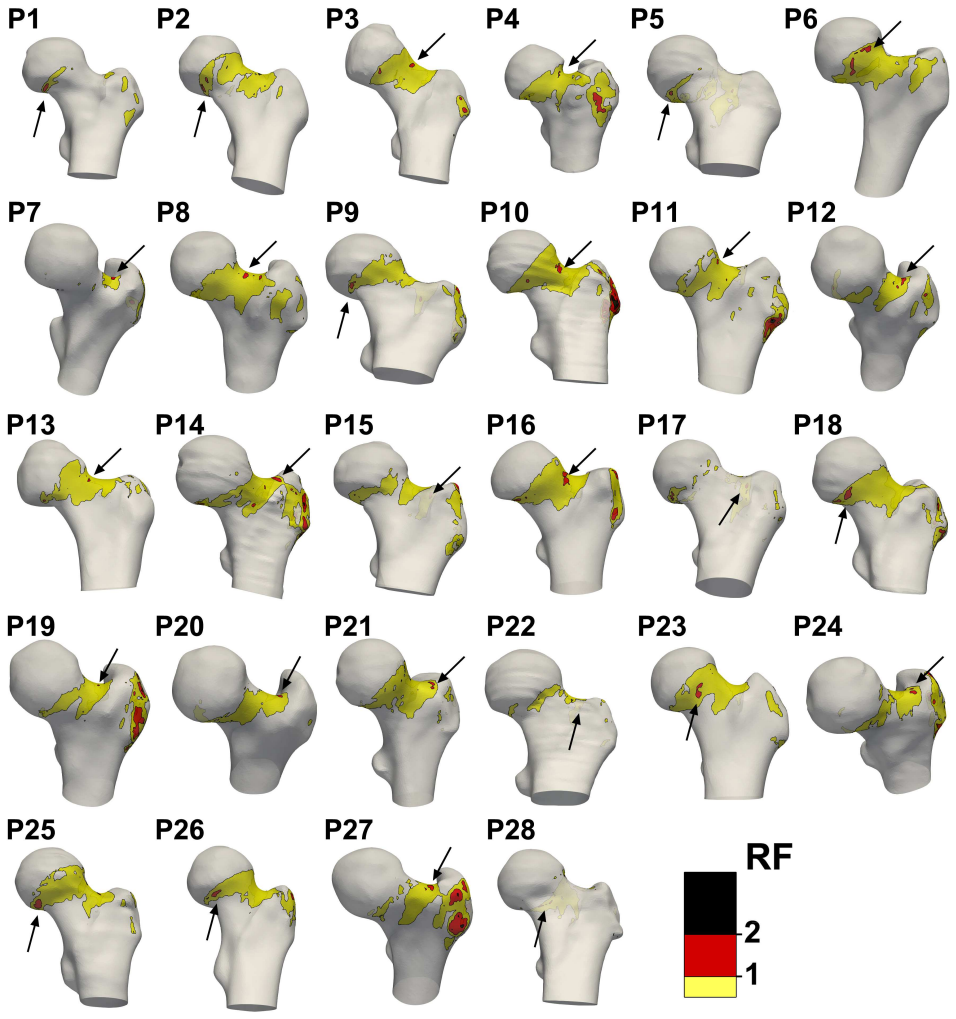

Figure 2.12: Superficial *RF* distribution for the 28 patient-specific models in the neutral configuration, shown at the load-step causing failure. Only *RF* values above the 90^{th} percentile (0.41) are depicted. The arrows highlight the identified failed area.

have caused a more prominent bending loading at the neck itself, which could have made the BR at the narrow neck a better predictor. Taking

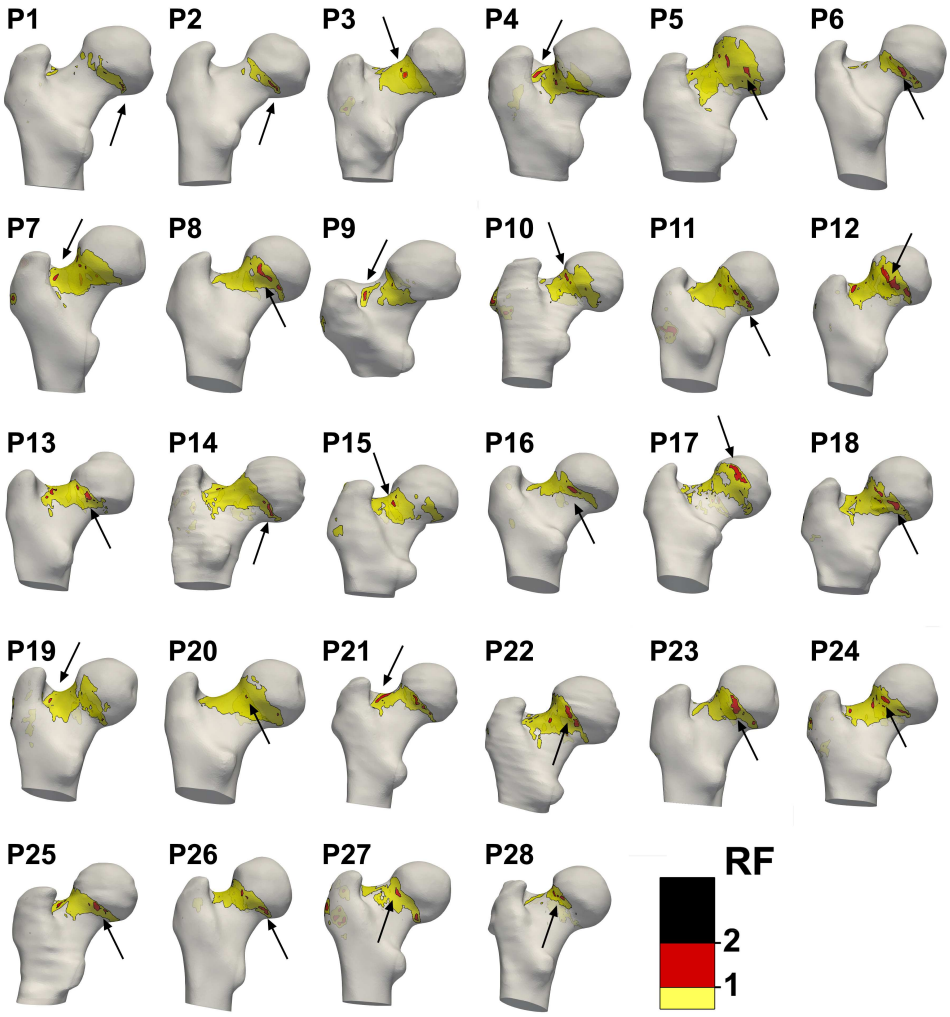

Figure 2.13: Superficial *RF* distribution for the 28 patient-specific models in the inclined configuration, shown at the load-step causing failure. Only *RF* values above the 90^{th} percentile (0.49) are depicted. The arrows highlight the identified failed area.

the FS as the dependent variable, the AIC-based regression analysis drew attention to the BR and CSMI at the narrow neck independently of the femur orientation. The optimal HSA variables combination for the inclined

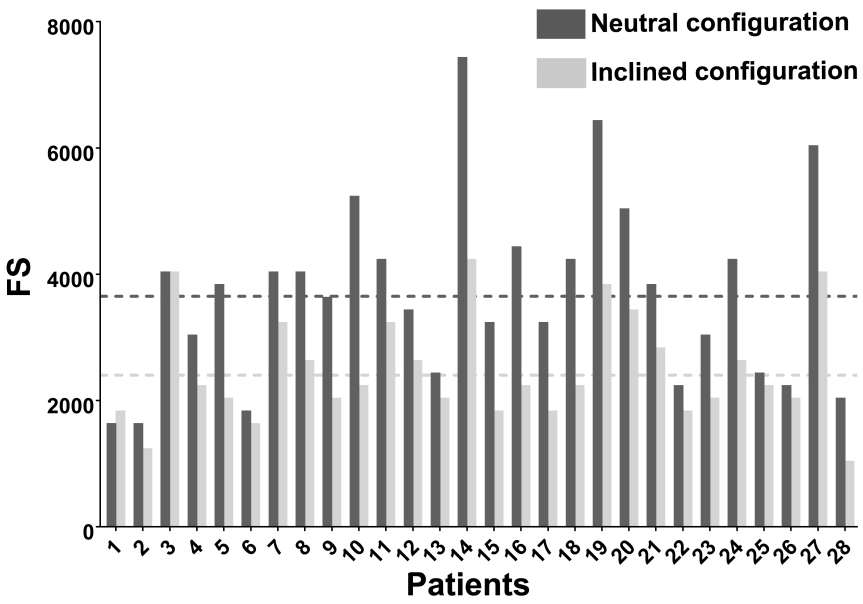

Figure 2.14: The patient-specific FS values (N) in the inclined and neutral orientations. The corresponding mean values are shown as dotted lines.

femur configuration also included the BR at the femoral shaft, and the NSA did not appear in any combination.
The coefficients of the optimal regression models for the RFI and the FS, which can be written as

$$\mathrm{RFI}_{HSA} = \beta_0 + \beta_1\, NSA + \beta_2\, BR_{nn}, \tag{2.10}$$

$$\mathrm{FS}_{HSA} = \beta_0 + \beta_1\, CSMI_{nn} + \beta_2\, BR_{nn} + \beta_3\, BR_{fs} \tag{2.11}$$

are shown in Table 2.4, in their standardized version (beta weights) as well. Looking at the beta weights, the effect of the independent variables on the dependent one do not differ significantly, except for the NSA contribution which seems to be slightly inferior to that of BR in the case of the RFI regression model.

Table 2.2: The HSA variables included in the best five RFI regression models according to AIC. R^2_{adj} and the Akaike weights w are provided too.

Variables	R^2_{adj}	w
RFI$_n$		
$\{NSA, BR_{fs}\}$	0.332	0.049
$\{NSA, BR_{nn}\}$	0.372	0.047
$\{NSA, BR_{nn}, BR_{fs}\}$	0.442	0.047
$\{NSA, BR_{nn}, BR_{it}, BR_{fs}\}$	0.406	0.035
$\{BR_{nn}, BR_{it}, BR_{fs}\}$	0.353	0.030
RFI$_i$		
$\{NSA, BR_{nn}\}$	0.493	0.097
$\{NSA, CSMI_{nn}, BR_{nn}\}$	0.519	0.080
$\{HAL, NSA, BR_{nn}, BR_{fs}\}$	0.551	0.075
$\{NSA, BR_{nn}, BR_{fs}\}$	0.507	0.057
$\{HAL, NSA, BR_{nn}, BR_{it}BR_{fs}\}$	0.577	0.053
RFI		
$\{NSA, BR_{nn}\}$	0.457	0.091
$\{NSA, CSMI_{nn}, BR_{nn}\}$	0.483	0.071
$\{HAL, NSA, BR_{nn}, BR_{fs}\}$	0.513	0.059
$\{NSA, BR_{nn}, BR_{fs}\}$	0.470	0.051
$\{HAL, NSA, BR_{nn}, BR_{it}, BR_{fs}\}$	0.541	0.041

With the purpose of visualizing the goodness of the identified predictive models, Figure 2.15 offers the comparison between the true, i.e. as extracted from the FE analyses, and the predicted RFI and FS values for the whole dataset, which both resulted to be significantly correlated ($p < 0.0001$), with a better performance of the FS predictive model.
Lastly, Table 2.5 provides the eight HSA variables included in the AIC regression analysis ranked according to their Akaike cumulative weights w_+ with respect to the RFI and FS regressions.
Looking at it, the attention is drawn to the BR at the narrow neck and shaft, which might then appear as a pivotal parameter, being placed

Table 2.3: The HSA variables included in the best five FS regression models according to AIC. R^2_{adj} and the Akaike weights w are provided as well.

Variables	R^2_{adj}	w
FS$_n$		
$\{CSMI_{nn}, BR_{nn}\}$	0.592	0.181
$\{CSMI_{nn}, BR_{nn}, BR_{fs}\}$	0.592	0.072
$\{CSMI_{nn}, BR_{nn}, CSMI_{it}\}$	0.589	0.065
$\{CSMI_{nn}, BR_{nn}, BR_{it}\}$	0.586	0.059
$\{CSMI_{nn}, BR_{nn}, W_{it}\}$	0.578	0.046
FS$_i$		
$\{CSMI_{nn}, BR_{nn}, BR_{fs}\}$	0.583	0.069
$\{CSMI_{nn}, BR_{nn}\}$	0.547	0.055
$\{HAL, CSMI_{nn}, BR_{nn}, BR_{fs}\}$	0.603	0.049
$\{HAL, CSMI_{nn}, BR_{nn}, W_{it}, BR_{fs}\}$	0.630	0.0405
$\{CSMI_{nn}, BR_{nn}, W_{it}\}$	0.565	0.039
FS		
$\{CSMI_{nn}, BR_{nn}, BR_{fs}\}$	0.566	0.065
$\{CSMI_{nn}, BR_{nn}\}$	0.531	0.054
$\{HAL, CSMI_{nn}, BR_{nn}, BR_{fs}\}$	0.589	0.049
$\{HAL, CSMI_{nn}, BR_{nn}, W_{it}, BR_{fs}\}$	0.613	0.035
$\{CSMI_{nn}, BR_{nn}, W_{it}\}$	0.545	0.034

Table 2.4: The regression coefficients β_i and standardized regression coefficients β_{Si} for the optimal multivariate models.

y	β_0	β_1	β_2	β_3	β_{S0}	β_{S1}	β_{S2}	β_{S3}
RFI	-9.35	0.07	0.16	-	-	0.35	0.55	-
FS	3302.08	451.22	-81.01	-212.24	-	0.39	-0.37	-0.29

among the first three most important HSA variables.

In Figure 2.16, the predictive abilities of the RFI and FS are compared to those of the T-score for all the patients. RFI and FS values are displayed

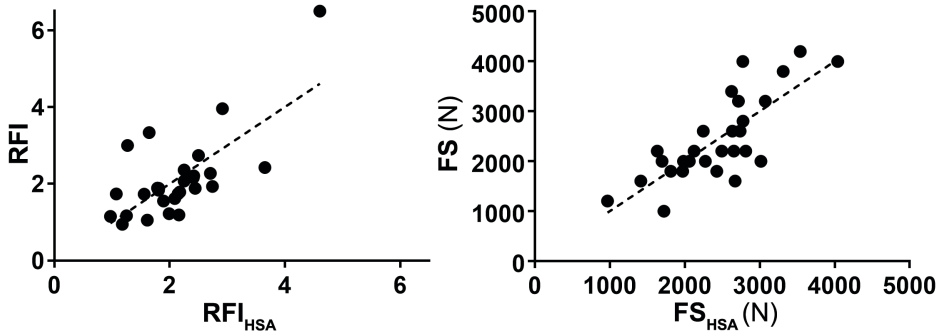

Figure 2.15: Comparison between FS, FS_{HSA} (left) and RFI, RFI_{HSA} (right) for each patient. The true and estimated values were significantly correlated ($p < 0.0001$, $R^2 = 0.50$ for the RFI and $R^2 = 0.61$ for the FS). The corresponding regression lines are reported as well.

Table 2.5: The eight HSA variables ranked according to their cumulative Akaike weights w_+ related to the RFI and FS regression analyses.

RFI		**FS**	
HSA Variables	w_+	**HSA Variables**	w_+
BR_{nn}	0.9308	$CSMI_{nn}$	0.8702
NSA	0.8233	BR_{fs}	0.6163
BR_{fs}	0.4550	BR_{nn}	0.6152
HAL	0.3222	HAL	0.4110
$CSMI_{nn}$	0.2898	W_{it}	0.3841
BR_{it}	0.2829	BR_{it}	0.3447
W_{it}	0.2182	$CSMI_{it}$	0.2335
$CSMI_{it}$	0.2116	NSA	0.1582

as computed from the FE analyses outcomes for the 28 patients with CT available and as predicted by the optimal regression models for the two additional fractured patients whose DXA information was available only. The two fractured patients are displayed as empty circles, while patients who may seem highlighted as at higher risk have been depicted with empty

diamonds. As visible, it might seem that among the non-osteoporotic patients some are at higher risk of fracture.

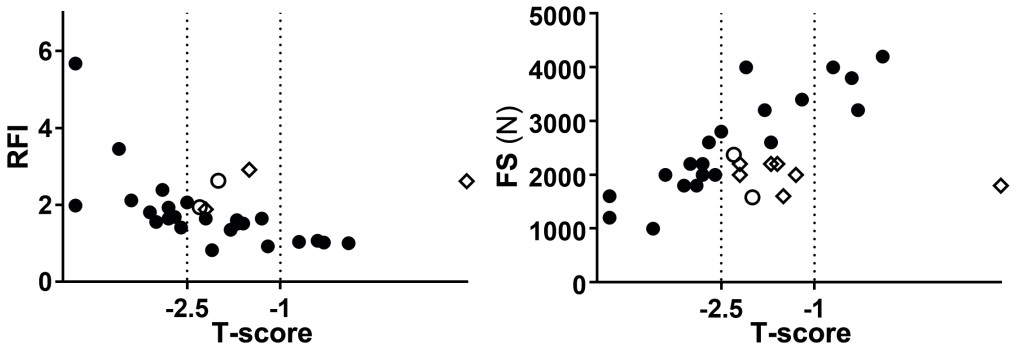

Figure 2.16: Comparison between the RFI and FS with the T-score outcomes. The three standard ranges of the T-score based criterion are highlighted: no osteoporosis/osteopenia: T-score > -1; osteopenia: $-2.5 <$ T-score > -1; osteoporosis: T-score < -2.5. Empty circles refer to the two fractured patients predicted values, while empty diamond show the non-osteoporotic patients appearing at higher risk. Both RFI and FS turned out to be significantly correlated to the T-score (RFI: $R = 0.42, p < 0.02$, FS $R = 0.52, p < 0.003$).

2.4 Discussion

The study presented in this chapter aimed to investigate HSA variables as potential osteoporotic hip fracture risk interpreters, given that in recent years many studies have confirmed the limitations of the gold-standard T-score [94–96] together with the role played by femur geometry [30, 51]. Herein, this could not be done retrospectively and the most relevant HSA parameters assessment was based on two proximal femur fracture risk indices extracted from CT-based FE analyses.

In our findings, the main HSA parameters involved in the optimal regression models as predictors of the RFI and FS were the BR at the narrow neck and shaft, together with the NSA. These results turn out to be in

accordance with the outcomes of Gnudi et al. [52], in which the NSA was identified as the sole statistically significant variable, and of Kaptoge et al. [30], where BR and NSA were identified as hip fracture predictors. Coherently with many other studies, the predictive ability of BR highlighted in this study is consistent with the idea that osteoporosis degrades strength by reducing cortical stability [30]. In particular, this outcome also highlights the important role of the gradual widening of the bone aimed at maintaining strength while progressively losing bone mass, which eventually leads to cortical instability and to an abrupt loss of mechanical strength [97]. Unfortunately, these changes are concealed by an unaltered areal BMD [98]. Moreover, the most effective osteoporosis treatments, leading to fracture risk reduction, are supposed to stimulate cortical bone thickness increase [99, 100], supporting the relevance of the BR, in which cortical thickness information is contained. The presence of the BR at the femoral shaft among the best predictors might seem uncommon, but it was found to be in accordance with retrospective analyses on fracture-prone geometric features [101–103].

It is not straightforward to assess why the NSA was not included among the best FS predictors (Table 2.3): with an effect on the bending moment arm at the neck, NSA might affect the strain level directly, mirrored by the RFI which basically represents the highest principal strain value. However, this direct link may be lost when establishing the load required to make a specific number of contiguous elements reach a strain threshold. The HSA-derived BMDs were not included in the AIC-based regression analysis: being directly calculated from other HSA variables, the VIF calculation prevented their inclusion in the subsequent analysis. Interestingly, the inclusion of the BMD computed at the femoral neck in the two identified optimal predictive models did lead to an increase in their corresponding explained variance (13.5% and 3.2% increase for the RFI and the FS models respectively), although, with the only exception of the NSA for the RFI regression model, it entailed the other HSA variables to lose their significance at the 5% significance level in the models. The

BMD was indeed significantly correlated to the BR as computed both at the narrow neck and femoral shaft and to the CSMI at the narrow neck, once again pointing out the mineral mass-dependency of the considered HSA variables.

If attention is drawn to Figure 2.16, the predictive abilities of the two regression models and the T-score for each patient can be compared. It is noteworthy to observe that, on one hand, the patients who would be classified as osteoporotic according to the T-score based criterion (T-score < -2.5) are all correctly identified by relatively high (> 3) RFI and low (< 2300) FS values; on the other, that, among the patients who would be classified as only osteopenic ($-2.5 <$ T-score < -1), some are highlighted as at higher risk according to their RFI and FS values. Actually, the two fractured patients, classified as osteopenic by the T-score, are located at the most critical bounds of the FS and RFI range covered by the other osteopenic patients. One of the two in particular, markedly outdistances the others. Other osteopenic patients, displayed with empty diamonds, would appear at higher fracture risk, with the FS covering a wider range and drawing attention to an higher number of them (patients 1, 4, 5, 9, 10, 16 classified as at higher risk according to the FS; patients 1, 4 classified as at higher risk according to the RFI). In addition, the same healthy (T-score > -1) patient (patient 17) was located in an higher risk region according to the FS.

Unfortunately, these outcomes could not find any real evidence because of the lack of fracture status information for the considered cohort. The possibility to access follow-up information for these 28 patients would have allowed to go beyond speculation, although only two patients subjected to hip fracture following a fall could be used to test the predictive models performance. This might not be sufficient for a substantial validation, preventing further conclusions and deductions from the afore-mentioned outcomes. Some other limitations characterizing this study are worth being mentioned. HSA variables are determined on the basis of a simplistic model for the proximal femur cross-sectional geometry based on

elementary geometric shapes, which may be noticeably altered in reality [30]: although useful and able to discern different femurs geometries, two-dimensional scans of three-dimensional bones might indeed provide modest precision [30]. Furthermore, the sideways fall condition was reproduced imposing simplified boundary conditions, which have solely considered the proximal portion of the femur. Since the FE simulations outcomes represented the starting point for all the subsequent analyses, deductions and understanding, the imposed boundary conditions assumed a fundamental role. From this perspective, they were applied consistently with approaches adopted in other works [61, 63, 65, 66, 104], where a validation could be achieved through comparison with experimental data. The distal hinge, generally employed experimentally [66], has also been often included computationally [60, 61, 63]. The use of spring elements to account for acetabular cartilage is not usually found in literature, although cartilage has been accounted for in a number of studies [65, 67, 104]. Here, in this regard, the addition of springs instead of a full constraint is expected to have reduced the reaction force at the head. It must be said that substantially, all the studies on the topic could couple *ex-vivo* experimental and computational analyses on the same specimens, managing to achieve a straightforward validation beyond a perfect methodological correspondence between the two approaches. Herein, working on living patients' data, that was obviously not possible. The aim was not the reproduction of experimental tests, rather, the possibility to get further insights in the relative fracture probability of the cohort under study. The boundary conditions were applied in accordance with those afore-mentioned validated studies, but, though qualitatively the most critical regions were the same and the strength values were consistent, a direct comparison was not possible, also given the number of variables involved. As far as the RFI is concerned, it was extracted applying an impact load determined based on a 1 degree of freedom mass-spring-damper system, already proposed in [83]. Hence, trochanteric soft tissues effect could be accounted for in the impact force definition. However, this was not done in a patient-specific manner, since

springs and damper values were kept constant for all the patients; from this perspective, accounting for patient-specific trochanteric tissues impact attenuation might have affected the RFI-based results. Nevertheless, in [105] neither the stiffness nor the damping properties of the trochanteric soft tissues were found to be associated with soft tissues thickness. Besides, the pseudo-calibration procedure represented a further possible source of error included within the FE models. It might have indeed introduced a bias in the apparent density estimation form the HU and consequently in the strains. However, that is not deemed to have affected the outcomes as a whole. A relative fracture risk was indeed considered attempting to identify the HSA variables most meaningful to it, without the ambition of an absolute risk assessment. Furthermore, the simulated impact orientation reasonably has an effect on the corresponding outcomes both in terms of fracture outcomes and relevant geometric features. Therefore, a wider variety of orientation could have provided further insights.

In conclusion, this work has combined the development of three-dimensional patient-specific FE models and the subsequent use of clinical data aiming to support the present gold-standard for hip fracture risk estimation. Of course, this approach does not have the ambition to predict when and where a fracture will occur, rather, to assess the relative fracture risk among individuals.

Although CT images were necessary to build the three-dimensional FE models, in order to identify the training set of RFI and FS values, the identified predictive model only requires HSA variables, which are, at present, already provided together with DXA images. CT scanning is not indeed a first choice exam for osteoporotic patients, who only undergo DXA for diagnosis purposes. The fortuitous availability of both CT scans and DXA images for the whole patients set has here allowed to build accurate three-dimensional models which have eventually led to the definition of regression models able to provide a risk prediction. They are independent from the CT images themselves, uniquely based on DXA derived information, already in hands of clinicians at present.

Hence, the here adopted approach has explored the predictive ability of a HSA based hip fracture risk estimator which could support the current diagnostic standard. It has focused on the development of a predictive model combining the biomechanical approach followed in CT-based studies [62, 80, 89, 106] with clinical data, aiming to assess the HSA variables most relevant to the fracture risk and eventually to propose a regression model based on clinical parameters already provided to clinicians by the DXA imaging procedure. HSA parameters have been deeply investigated retrospectively [51], but rarely integrated in this kind of approaches. In conclusion, the method appears promising in supporting the clinical decision process to assess a relative fracture risk among individuals, and a larger amount of clinical data with available follow-up, combined with three-dimensional FE models, will help to achieve advances in the HSA variables role assessment.

Chapter 3

DXA FE Models for Hip Fracture Risk Prediction: a comparison with 3D Models

This chapter is partially based on the publication:

Terzini, M. & **Aldieri, A.**, Rinaudo L., Osella, G., Audenino, A.L. and Bignardi, C.

'Improving the Hip Fracture Risk Prediction through 2D Finite Element Models from DXA Images: Validation against 3D Models'

in *Frontiers in Bioengineering and Biotechnology*, 7, 220, 2019.

Abstract

Aiming to overcome the limitations which characterize the gold standard T-score measurement in the diagnosis of subjects at high risk of osteoporotic fractures, the possibility to develop 2D Finite Element (FE) analyses from DXA images would appear promising. DXA-based FE models indeed, in contrast to the CT-based ones, require the only availability of DXA images, on which the current diagnostic process of osteoporosis is based. From this perspective, the purpose of the work presented in this chapter was the investigation of the role that DXA-based two-dimensional patient-specific FE models of the proximal femur, in combination with T-score, could play in enhancing the risk of fracture relative assessment. With this aim, 2D FE models were built from DXA images of the 30 postmenopausal female subjects involved. A sideways fall condition was reproduced and the Risk of Fracture Index (RFI) and Femoral Strength (FS) were computed on the basis of principal strains criteria. The outcomes were then compared to those obtained in the previous chapter, where the corresponding CT-based FE models were developed. The identified RFI and FS turned out to be significantly correlated with the corresponding 3D-based predictors, although able to explain only partially their variance. The patients highlighted as at higher risk were the same. Moreover, the 2D predictors resulted significantly correlated with the T-score (RFI: $R = 0.48, p < 0.007$, FS $R = 0.54, p < 0.002$), and managed to better differentiate osteopenic patients, drawing the attention to some of them. In accordance with the three-dimensional outcomes, the most meaningful Hip Structural Analysis (HSA) variables were the buckling ratio and the cross-sectional moment of inertia, thus stressing the role of the bone resistance to bending. In conclusion, DXA-based FE models, despite not appearing equivalent to the corresponding CT-based ones, appeared to be able to provide further hints compared to the sole T-score.

3.1 Introduction

Aiming to overcome the limitations of the fracture risk clinical predictors currently in use, which have been previously tackled, researchers have turned their attention to biomechanical approaches able to integrate the gold-standard with biomechanical variables which actually are important determinants of bone strength [107]. As seen in the previous chapter, the development of Finite Element (FE) models from CT images has thoroughly been investigated [28, 108], due to the possibility to include patient-specific actual geometric features and material properties in a reliable way. However, as already pointed out, CT does not, at present, represent the routine imaging technique for osteoporosis and fracture risk identification purposes, primarily because of its high dosage of radiation and, above all, much higher costs with respect to DXA. Hence, to meet the clinical reality, two-dimensional DXA-based FE models have also been developed to investigate their potentialities as supportive risk predictors [107, 109–115]. In spite of DXA projective nature, which provides a two-dimensional simplified representation of a complex three-dimensional structure, DXA images are indeed routinely acquired and thus clinically available. Besides, DXA-based FE models outcomes, despite the number of assumptions and simplifications introduced in this kind of models, have been shown to potentially enhance fracture risk estimation, bringing additional information independently from BMD [107, 109, 113–115]. Therefore, aiming to get further insights in the role 2D FE simulations might play, the main purpose of the here presented study was, in the fist place, the comparison between the performances of the developed DXA-based FE models with those of the Hip Structural Analysis (HSA)-based regression models presented in the previous chapter; moreover, the DXA- and CT-derived (chapter 2) outcomes were compared as well. This could be achieved thanks to the simultaneous availability of CT and DXA images for the same patients, which rarely occurs.

3.2 Materials and Methods

3.2.1 Subject-specific FE model construction

The same 28 post-menopausal female subjects (55-81 years, treated in San Luigi Gonzaga Hospital in Orbassano, Italy) cohort considered in the previous chapter for the CT-based FE models development was here used. Clinical and DXA-derived data (acquired with a Discovery DXA system, Hologic), together with CT scans, were available for the whole cohort. Therefore, 2D FE models were set up starting from DXA images, with the purpose of comparing their predictive capabilities with those of the 3D models built from CT data. Follow-up information for these 28 patients was not available, so, it was not possible to know if they actually ever fractured. For this reason, two additional post-menopausal female patients aged 71 and 75 years, fractured at the proximal femur within 1 year after the DXA exam after a fall at home, were included in the cohort, although the related 3D models construction was prevented by the lack of the CT scans.
The two-dimensional geometric models extraction from DXA scans was performed through a semi-automatic segmentation procedure (Mimics, v17, Materialise, Leuven, Belgium) based on images grey values, assuming the femoral head to be circular (Figure 3.1).

Subsequently, in order to identify the optimal mesh density, a sensitivity analysis on mesh dimensions was carried out. In accordance with [112], a plane-stress approach was chosen, since proximal femur frontal plane dimensions are slightly larger than those in the anterior-posterior one. In the Appendix, at the end of this chapter, a brief discussion comparing the chosen plane stress approach with the plane strain one is provided. The femur was assumed to be a plate with subject-specific thickness[112, 115]: therefore, CP6S elements (6-node Abaqus triangular plane stress elements) were used, and the corresponding thickness determined on the

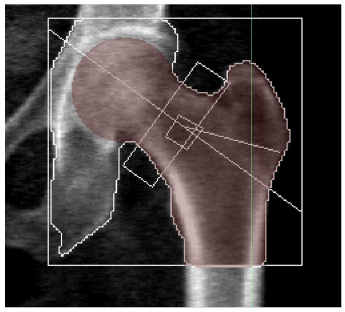

Figure 3.1: One example of geometric model of the proximal femur built on a DXA scan.

basis of the HSA femoral neck width W [112]. Specifically, the subject-specific element thickness t was calculated as such that, on average, the area and area moment of inertia (with respect to the longitudinal axis) of a rectangular cross section at the middle femoral neck (with a width W) matched those of a circular cross section with diameter W. Hence, the patient-specific thickness was defined as $t = \frac{3.5\pi W}{16}$ (further details in the Supplementary Material provided by [112]). Six different models with decreasing average edge length (3, 2, 1.5, 1, 0.5, 0.25 mm) were built and, as in the three-dimensional case, boundary conditions imposed to reproduce a simplified fall on the side (Figure 3.2). The sensitivity analysis was based on minimum (compressive) and maximum (tensile) principal strains extracted at the neck region, and, in particular, the lowest compressive principal strain and the highest tensile principal strain were identified in that region of interest for each mesh dimension. Errors were then computed for these two quantities with respect to the finest mesh. The 0.5 mm edge length mesh was chosen, producing an error lower then 3% (Figure 3.3). Once the optimal mesh dimensions were assessed, local heterogeneous material properties could be assigned. Pixel-by-pixel BMD values were extracted from DXA images, which carry this information; each mesh node was then assigned the BMD value of the pixel in which it was located and a node-based average BMD value was eventually assigned to

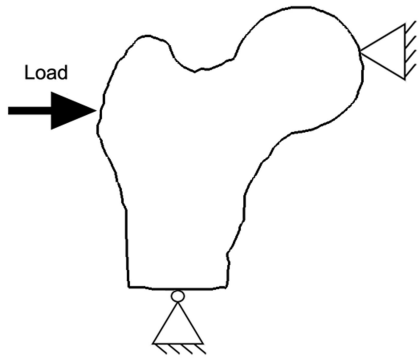

Figure 3.2: Boundary conditions employed to carry out the mesh dimensions sensitivity analysis.

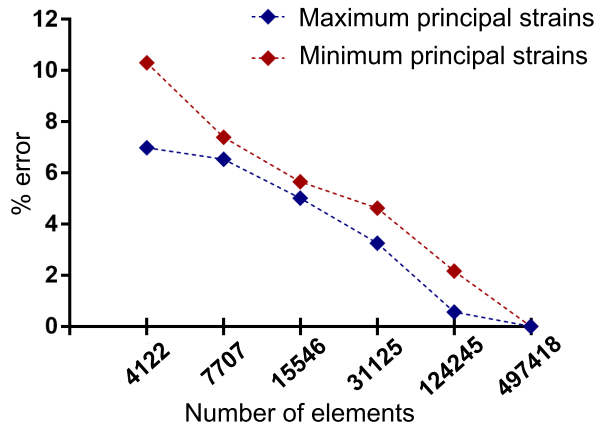

Figure 3.3: Mesh dimensions sensitivity analysis: % errors for tensile and compressive principal strains computed with respect to the finest mesh (0.25 mm edge length).

each mesh element. Similarly to the methodology explained in the previous chapter, the material properties assignment relied on the definition of a number of BMD-based bins characterized by a unique Young's modulus value identified from the bin central BMD value in this case. Therefore, a further sensitivity analysis was performed aiming to assess the number of

bins leading to sufficiently accurate results. Six different bin numbers (10, 20, 30, 40, 50, 60 bins) were investigated carrying out FE simulation of a sideways fall and considering maximum and minimum principal strains. Eventually, the 40 bins-based material properties assignment was chosen, with an error on both tensile and compressive principal strains inferior to 5% (Figure 3.4). Hence, elements could be grouped in the correspond-

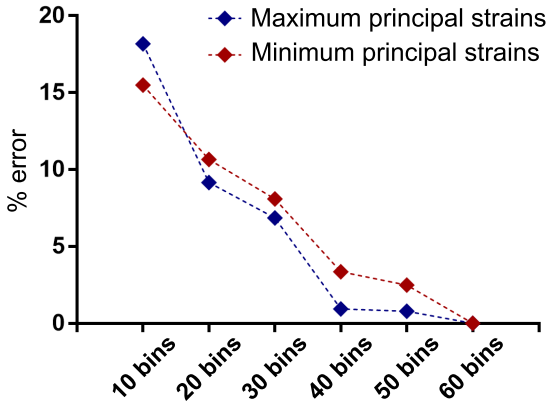

Figure 3.4: Material bins sensitivity analysis: % error for tensile and compressive principal strains computed with respect to the 60 bins-based material properties assignment.

ing bins according to their BMD, so that they were assigned with the bin-specific E value. In the case of DXA-derived models, Young's modulus definition started from the BMD values provided by DXA ($aBMD$). Having defined a patient-specific thickness from the femoral neck width ($t = \frac{3.5\pi W}{16}$), the volumetric BMD (ρ_v) could be derived according to [112]:

$$\rho_v = \frac{aBMD}{t} \frac{1.89}{1.05}, \tag{3.1}$$

where the $\frac{1.89}{1.05}$ ratio, referring to the bone tissue density-BMD ratio, was identified in [54]. In order to determine the corresponding apparent density

value (ρ_{app}), the volumetric density of Equation 3.1 was then converted according to [116, 117]:

$$\rho_{app} = \frac{\rho_v}{1.14 \cdot 0.598}. \tag{3.2}$$

Young's modulus values (GPa) could eventually be calculated using the same empirical relationships [71] used in the three-dimensional case:

$$E = 15.010\, \rho_{app}^{2.18},\ if\ \rho_{app} \leq 0.28\, g/cm^3, \tag{3.3}$$

$$E = 6.850\, \rho_{app}^{1.49},\ if\ \rho_{app} > 0.28\, g/cm^3. \tag{3.4}$$

3.2.2 FE analyses generation

Boundary conditions reproducing a sideways fall condition were applied coherently with those presented in the previous chapter. Briefly, in order to reproduce a sideways-fall condition, the impact force was applied on the greater trochanter surface in the frontal plane, the femoral head was bound to the ground by means of spring elements with a 10000 $\frac{N}{mm}$ stiffness in the impact load direction, while the model distal nodes were connected to a node located distally, with rotational degrees of freedom only (Figure 3.5). Analogously to the three-dimensional analyses, two different configurations were explored: in the former one the 2D model was aligned to the shaft axis, and the impact load applied perpendicularly to it; in the second one, on the other hand, the proximal femurs were medially rotated by 15° in the frontal plane (Figure 3.6). Due to the two-dimensionality of the problem, the femoral anteversion in the transversal plane was not possible.

3.2.3 FS and RFI estimates

Principal strain-based failure criteria [60, 63, 106] were adopted to predict fracture risk. In particular, at each element centroid, the Risk of Fracture (RF) was computed dividing the prevailing principal strain,

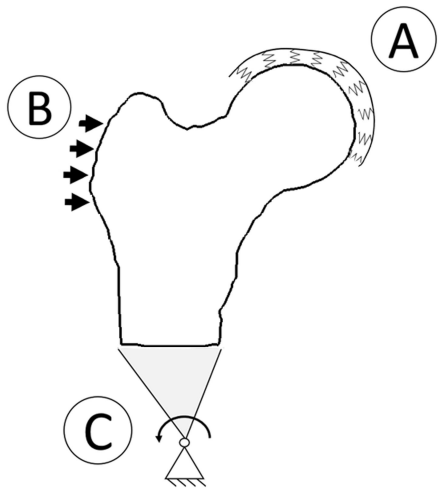

Figure 3.5: Boundary conditions applied to reproduce the sideways fall. A) head nodes were bounded to the ground through spring elements with $10000 \frac{N}{mm}$ stiffness; B) impact load was applied as a distributed force on the trochanteric surface; C) distal nodes of the proximal femur were connected to a spherical joint placed $0.1\,m$ distally by means of link elements. From [118].

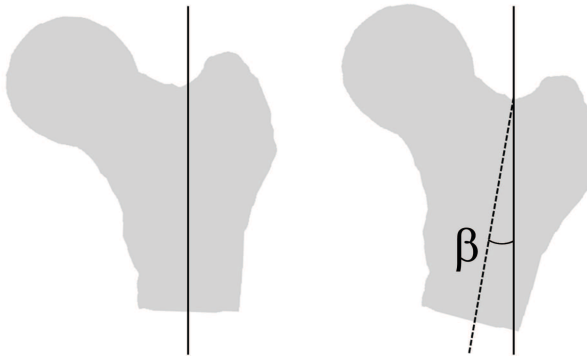

Figure 3.6: The two different configurations explored: the neutral (left) and tilted configuration. β was, as in the 3D case, 15°, while α could not be set due to the two-dimensionality of the problem.

evaluated comparing tensile and compressive principal strains, by the respective threshold values, i.e. -0.0104 in compression and 0.0073 in tension

[82]. The use of thresholds determined on a three-dimensional basis on two-dimensional-based outcomes is discussed in the Appendix section at the end of this chapter. The out-of-plane strain, which exists in the plane stress case, was not considered in the principal strains extraction. As done in the three-dimensional case, two different fracture risk predictors were measured based on principal strains: the Femoral Strength (FS) and the Risk Factor Index (RFI). The FS was identified increasing the impact load linearly until the number of failed ($RF > 1$) contiguous elements exceeded 0.15% of the total number of elements, in accordance with [112, 113]. Precisely, at each load increment (100 N), the elements characterized by a $RF > 1$ were identified, and they were considered contiguous if the mutual centroids distance was lower than 1.3 mm.
The RFI, instead, was defined as the highest RF value at the patient-specific impact load identified through the 1 degree-of-freedom mass-spring-damper model presented in the previous Chapter. Differently from the 3D case, where only cortex elements were considered when identifying both the risk indices, the whole elements set was here taken into account due to the projective nature of the DXA images and thus of the models [112, 113]. Head and trochanteric regions, where results could have been affected by boundary conditions, were not considered for sake of the FS and RFI computation [60, 119]. FS and RFI were computed in both the two different configurations explored, i.e. the neutral one (leading to the FS_{2Dn} and RFI_{2Dn} extraction) and the inclined one (leading to the FS_{2Di} and RFI_{2Di} extraction). Subsequently, comparing the two, the most critical values, simply called FS_{2D} and $RFIFS_{2D}$, were identified:

$$FS_{2D} = min(FS_{2Dn}, FS_{2Di}) \tag{3.5}$$

$$RFI_{2D} = max(RFI_{2Dn}, RFI_{2Di}). \tag{3.6}$$

For comparison purposes, HSA variables most relevant to the 2D risk indices RFI_{2D} and FS_{2D} were here identified as well. First of all, a collinearity diagnosis based on Variance Inflation Factor (VIF) [92] calculation was carried out, so that only independent HSA parameters were selected. Subsequently, Akaike Information Criterion (AIC) [93] was adopted to identify those accounted for within the best models.

3.3 Results

First of all, focusing on the sole 2D outcomes, the two different fracture risk predictors, the RFI_{2D} and FS_{2D}, are compared in Figure 3.7: as in the three-dimensional case, they turned out to be significantly correlated ($R = 0.75, p < 0.0001$), although a low FS_{2D} area can be identified spanning very different RFI values. In Figure 3.8, the outcomes related

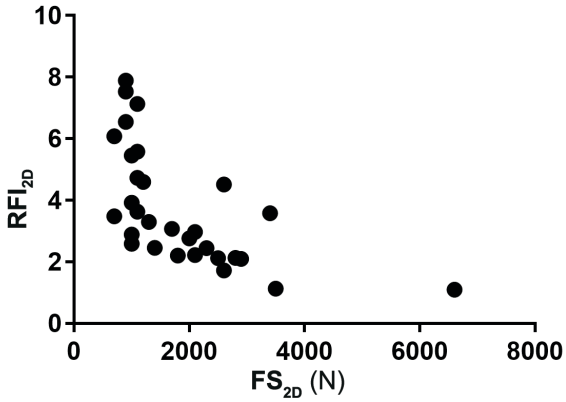

Figure 3.7: Comparison between the FE analyses-based RFI_{2D} and FS_{2D} values identified for the 30 patients included in the study.

to the neutral and inclined configurations respectively can be observed for the two risk predictors considered: as visible, a strong correlation exists in both cases ($R > 0.97$, $p < 0.0001$), and analogously to the 3D case, the

inclined configuration resulted the most critical.

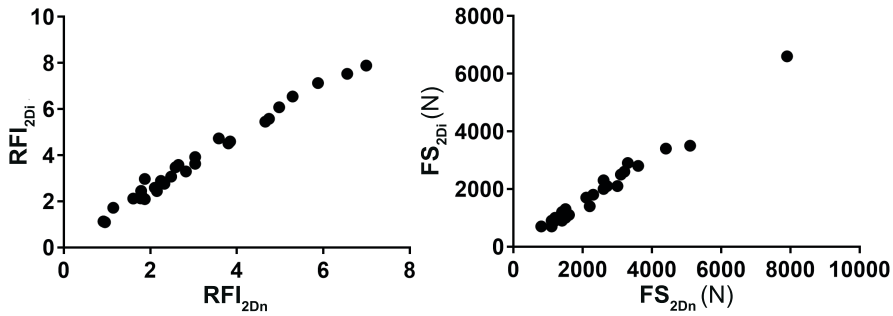

Figure 3.8: RFI_{2D} (left) and FS_{2D} (right) values in the neutral and inclined configurations explored through the FE analyses.

Figures 3.9 and 3.10 display the overall distribution of the *RF* for the 30 patients at the load-step when fracture was supposed to occur for the neutral (Figure 3.9) and inclined (Figure 3.10) femur orientations. For visualization purposes only, the cell-centered variable is shown as interpolated at the nodes and the *RF* higher than the 90^{th} percentile have been depicted, judged evidence of a considerable strain level. Some patients show high *RF* at the greater trochanter, but that area was not considered while identifying the contiguous failed elements because it might have been affected by the load application.

While in the three-dimensional case noticeable differences could be appreciated between the localization and distribution of the *RF* in the two analysed configurations, in the 2D case only slight alterations of the *RF* distribution between the neutral and tilted configuration at the estimated fracture load could be appreciated. Figure 3.11 offers an overview of the patient-specific FS_{2D} values as assessed from the FE analyses in the neutral and inclined femur orientation respectively. From this perspective, if it is compared to the corresponding one in the three-dimensional case (Figure 2.14), some patients can be found (e.g. patients 19 and 27), whose strength markedly overcomes the average values and conversely whose strength is

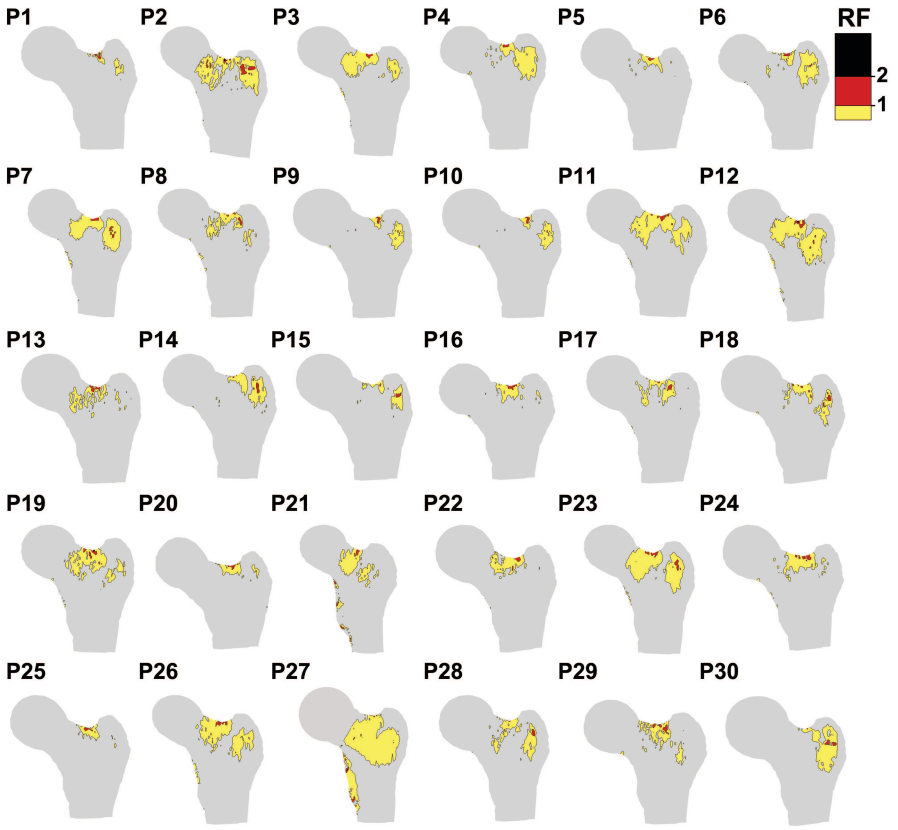

Figure 3.9: *RF* distribution for the 30 patient-specific models in the neutral configuration, shown at the load-step causing failure. Only *RF* values above the 90^{th} percentile (0.47) are shown.

well below them (e.g. patients 1, 2, 6, 22, 28) in both cases. Nevertheless, cases of considerable low (e.g. patients 4, 5, 10, 20, 25) or high (e.g. patients 7, 11, 12) FS_{2D} did not find a correspondence in the 3D one.

Moreover, Figure 3.12 compares the 28 patients *RF* distribution in the 3D and 2D models for the inclined configuration at the estimated patient-specific impact load. As visible, although a precise co-localization of the regions interested by the highest *RF* values cannot be found between the 3D and 2D models, it is still interesting to notice that the patients with

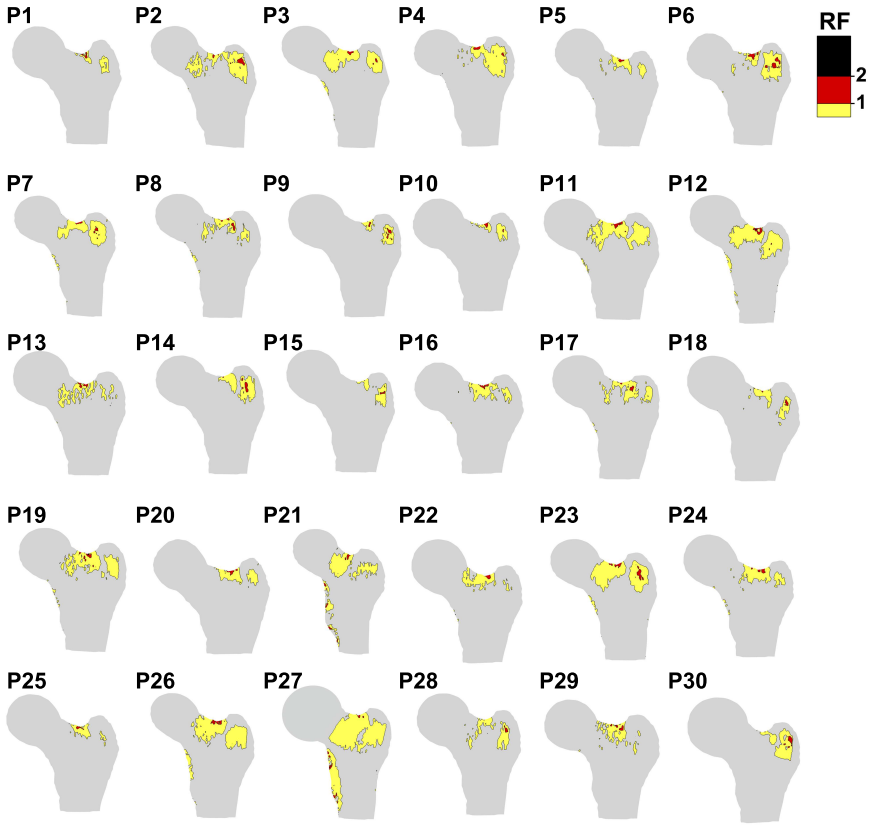

Figure 3.10: *RF* distribution for the 30 patient-specific models in the inclined configuration, shown at the load-step causing failure. Only *RF* values above the 90^{th} percentile (0.41) are shown.

the largest high *RF* regions or showing extremely high ($RF > 2$) *RF* values are often the same. In Figure 3.13, the comparison between the three- and two-dimensional-based outcomes is shown, both in terms of the RFI and FS. Regressing the 3D predictors on the 2D ones, the RFI_{2D} could explain only a small portion of the RFI_{3D} variance, R^2 being 0.26 ($p < 0.0057$). As for the FS_{2D}, it managed to explain nearly half of the variance of the corresponding FS_{3D} ($R^2 = 0.46, p < 0.0001$). Interestingly,

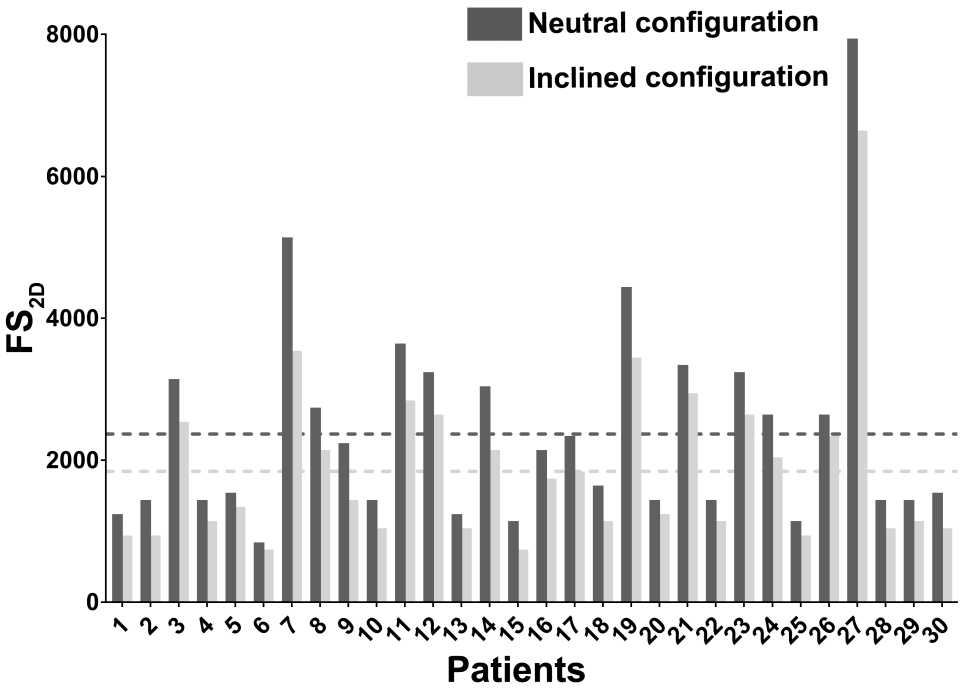

Figure 3.11: The patient-specific FS_{2D} values (N) in the inclined and neutral orientations. The corresponding mean values are shown as well.

the strength determined in the two-dimensional case was generally underestimated compared to CT-based strength (this might have been caused by the choice to model the femur as a plate with constant thickness, as shown in the Appendix). In particular, this occurred analogously considering the neutral and inclined configurations outcomes separately, and the few cases showing an opposite trend (2D strength higher than 3D strength) were the same. Although clearly distinctive features could not be identified characterizing those patients yielding an higher DXA-based strength, qualitatively they showed 2D shapes generally larger in size compared to the average, together with, looking at the three-dimensional geometry, smaller dimensions in the antero-posterior direction.

For sake of comparison with the three-dimensional case, an AIC-based

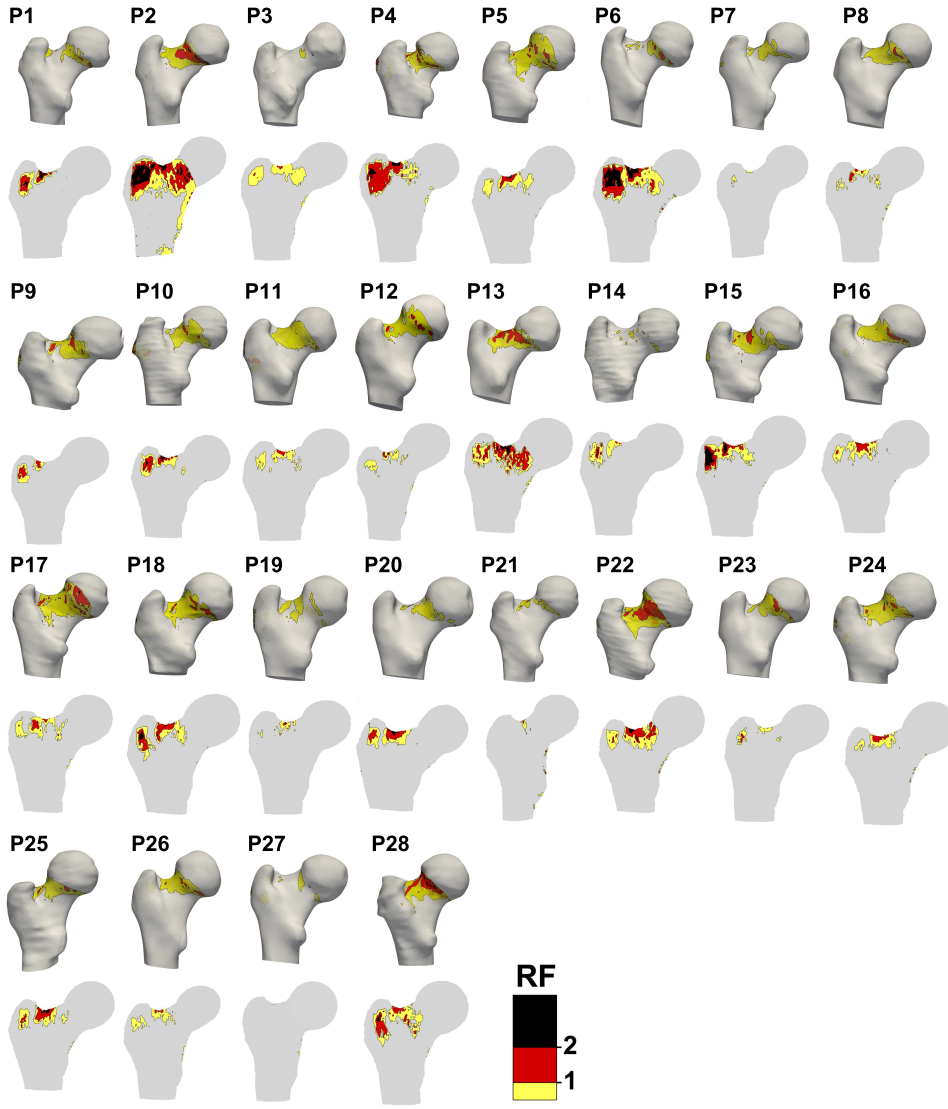

Figure 3.12: Comparison of the *RF* distribution for the 28 patients between the CT- and DXA-based models in the inclined configuration at the estimated patient-specific impact load. Only *RF* values above the 90^{th} percentile (0.51 for the 3D case, 0.6 for the 2D case) are shown.

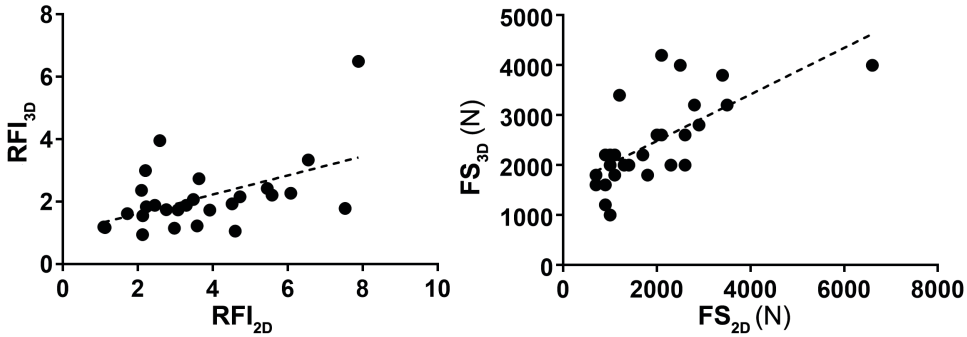

Figure 3.13: Comparison of the RFI and FS in the three-dimensional (RFI_{3D} and FS_{3D}) and two-dimensional (RFI_{2D} and FS_{2D}) case. The regression lines are displayed as well.

multivariate linear regression analysis was carried out, in order to identify the most relevant HSA variables with respect to the RFI_{2D} and FS_{2D} as well. The HSA variables included within the best 5 regression models according to the AIC are presented in Tables 3.1 and 3.2. As visible, the AIC-based optimal HSA descriptors were strongly related to the bone resistance to bending, which was reasonable and coherent with the three-dimensional outcomes. Nearly all the RFI_{2D}-based optimal combinations incorporated the BR, the CMSI at the narrow neck and the HAL, rather than the NSA, included in the 3D case. Moreover, taking the FS_{2D} as the dependent variable, the optimal 2D regression model turned out to be very similar to the 3D one, including the CSMI and BR at the narrow neck plus the BR at the femoral shaft. In addition, however, the NSA appeared within the model.
The coefficients of the optimal regression models for the RFI_{2D} and the FS_{2D}, which can be written as

$$\mathrm{RFI}_{2DHSA} = \beta_0 + \beta_1\, CSMI_{it} + \beta_2\, BR_{nn}, \tag{3.7}$$

$$\mathrm{FS}_{2DHSA} = \beta_0 + \beta_1\, NSA + \beta_2\, CSMI_{nn} + \beta_3\, BR_{nn} + \beta_4\, BR_{fs} \tag{3.8}$$

Table 3.1: The HSA variables included in the best five RFI_{2D} regression models according to AIC. R^2_{adj} and the Akaike weights w are provided as well.

Variables	R^2_{adj}	w
RFI_{2Dn}		
$\{CSMI_{nn}, BR_{nn}\}$	0.319	0.072
$\{HAL, BR_{nn}, BR_{it}, BR_{fs}\}$	0.393	0.061
$\{HAL, BR_{nn}, BR_{fs}\}$	0.329	0.036
$\{HAL, BR_{nn}\}$	0.288	0.036
$\{BR_{nn}, BR_{fs}\}$	0.281	0.031
RFI_{2Di}		
$\{CSMI_{it}, BR_{nn}\}$	0.289	0.064
$\{HAL, BR_{nn}\}$	0.284	0.058
$\{HAL, BR_{nn}, BR_{fs}\}$	0.319	0.052
$\{HAL, BR_{nn}, BR_{it}, BR_{fs}\}$	0.356	0.044
$\{BR_{nn}, BR_{fs}\}$	0.256	0.033
RFI2D		
$\{CSMI_{it}, BR_{nn}\}$	0.289	0.064
$\{HAL, BR_{nn}\}$	0.284	0.058
$\{HAL, BR_{nn}, BR_{fs}\}$	0.319	0.052
$\{HAL, BR_{nn}, BR_{it}, BR_{fs}\}$	0.356	0.044
$\{BR_{nn}, BR_{fs}\}$	0.256	0.033

are shown in Table 3.3, in their standardized version (beta weights) as well. Looking at the beta weights, the BR at the narrow neck might seem to have a stronger effect on both the RFI_{2D} and FS_{2D} with respect to the other HSA predictors included within the two optimal models, particularly as far as the RFI_{2D} is concerned. With the purpose of visualizing the goodness of the identified predictive models, Figure 3.14 offers the comparison between the true, i.e. as extracted from the FE analyses, and the predicted RFI and FS values for the whole dataset, which both resulted to be significantly correlated ($p < 0.0001$), with a better performance of the FS predictive model.

Table 3.2: The HSA variables included in the best five FS_{2D} regression models according to AIC. R^2_{adj} and the Akaike weights w are provided as well.

Variables	R^2_{adj}	w
FS_{2Dn}		
$\{NSA, CSMI_{nn}, BR_{nn}, BR_{fs}\}$	0.656	0.164
$\{HAL, NSA, CSMI_{nn}, BR_{nn}, BR_{fs}\}$	0.661	0.069
$\{NSA, CSMI_{nn}, BR_{nn}\}$	0.606	0.057
$\{NSA, CSMI_{nn}, CSMI_{it}, W_{it}, BR_{fs}\}$	0.657	0.056
$\{NSA, CSMI_{nn}, BR_{nn}, W_{it}, BR_{fs}\}$	0.654	0.049
FS_{2Di}		
$\{NSA, CSMI_{nn}, BR_{nn}, BR_{fs}\}$	0.619	0.119
$\{NSA, CSMI_{nn}, BR_{fs}\}$	0.577	0.068
$\{NSA, CSMI_{nn}, CSMI_{it}, W_{it}, BR_{fs}\}$	0.6307	0.064
$\{NSA, CSMI_{nn}, W_{it}, BR_{fs}\}$	0.597	0.052
$\{HAL, NSA, CSMI_{nn}, BR_{nn}, BR_{fs}\}$	0.623	0.047
FS2D		
$\{NSA, CSMI_{nn}, BR_{nn}, BR_{fs}\}$	0.619	0.119
$\{NSA, CSMI_{nn}, BR_{fs}\}$	0.577	0.068
$\{NSA, CSMI_{nn}, CSMI_{it}, W_{it}, BR_{fs}\}$	0.6307	0.064
$\{NSA, CSMI_{nn}, W_{it}, BR_{fs}\}$	0.597	0.052
$\{HAL, NSA, CSMI_{nn}, BR_{nn}, BR_{fs}\}$	0.623	0.047

Table 3.3: The regression coefficients β_i and standardized regression coefficients β_{Si} for the optimal multivariate models.

y	β_0	β_1	β_2	β_3	β_4	β_{S0}	β_{S1}	β_{S2}	β_{S3}	β_{S4}
RFI	1.597	-0.57	0.24	-	-	-	-0.21	0.52	-	-
FS	-8875.6	91.51	777.86	-83.60	-331.87	-	0.39	0.46	-0.27	-0.32

Eventually, Table 3.4 contains the HSA variables ranked according to their Akaike cumulative weights w_+, acting as surrogates of their relevance, with respect to the RFI_{2D} and FS_{2D} regressions. Interestingly, the

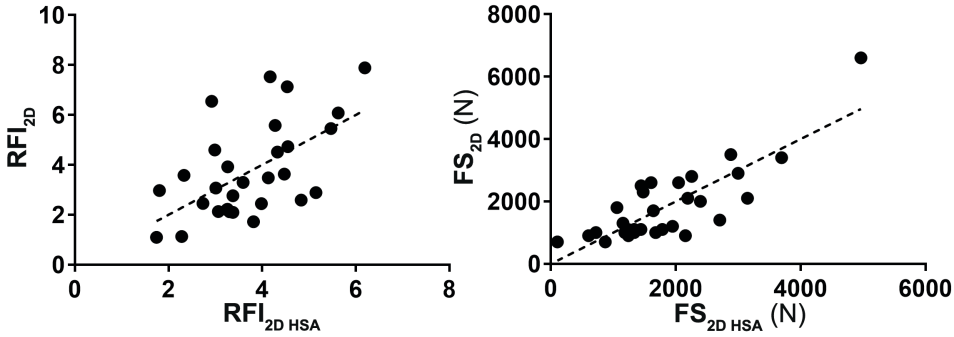

Figure 3.14: Comparison between FS_{2D}, $FS_{2D\ HSA}$ (left) and RFI_{2D}, $RFI_{2D\ HSA}$ (right) for each patient. The true and estimated values were significantly correlated ($R^2 = 0.34$ for the RFI and $R^2 = 0.67$, $p < 0.0001$ for the FS). The corresponding regression lines are reported as well.

first ones in importance, i.e. the BR and the CSMI at the narrow neck relatively to the RFI_{2D} and FS_{2D} respectively, were the same as in the three-dimensional case. On top that, also the BR at the femoral shaft turned out to be a meaningful variable, in agreement with the findings of the three-dimensional case. The HAL and NSA were also classified as the second most relevant variables with respect to the RFI_{2D} and FS_{2D}, even though they had not been highlighted as such by the 3D outcomes.
In Figure 3.15, the predictive abilities of the RFI_{HSA} and FS_{HSA} are compared to those of the T-score for all the patients. RFI_{2D} and FS_{2D} values are displayed as obtained from the DXA-based FE models. The two fractured patients are displayed as empty circles, while patients who may seem highlighted as at higher risk have been depicted with empty diamonds. As visible, while the RFI_{2D} predicts as at higher risk only one of the two fractured patients, the FS_{2D} manages to locate both in the low strength area. The RFI_{2D} also spreads the osteoporotic patients in a pretty wide RFI_{2D} interval, so that it might seem some are at a lesser degree of risk with respect to others. This does not occurr if the FS_{2D} is considered, which locates all the osteoporotic patients in the low strength region. Among

Table 3.4: The eight HSA variables ranked according to their cumulative Akaike weights w_+ related to the RFI_{2D} and FS_{2D} regression analyses.

RFI_{2D}		**FS_{2D}**	
HSA Variables	w_+	**HSA Variables**	w_+
BR_{nn}	0.8782	$CSMI_{nn}$	0.9583
HAL	0.4959	NSA	0.930
BR_{fs}	0.4382	BR_{fs}	0.7623
$CSMI_{nn}$	0.3688	BR_{nn}	0.4452
BR_{it}	0.3048	W_{it}	0.399
W_{it}	0.2404	HAL	0.3009
$CSMI_{it}$	0.2313	$CSMI_{it}$	0.2566
NSA	0.2024	BR_{it}	0.2514

the non-osteoporotic patients, on the other hand, some would be judged at higher risk of fracture. If the osteopenic patients are taken into account, patients 1, 4, 20 would be classified as at higher risk by both predictors, patients 5, 9 and 10 only according to the FS_{2D}. The healthy patients, eventually, do not locate in high risk region, although they would seem characterized by different risk level: looking at the RFI_{2D}, 2 patients (14 & 19) have slightly higher values, while considering the FS_{2D}, two patients can be identified (14 & 17) with lower strength than those in the same BMD range.

3.4 Discussion

In the last decades there has been a great effort towards a more accurate and reliable assessment of the fracture risk in elderly osteoporotic individuals. From this perspective, as mentioned in the previous chapter, three-dimensional FE models developed from CT and QCT scans have been shown to have excellent strains and fracture load predictive abilities with respect to *in vitro* experiments [63, 69, 106]. Thanks to the availability of CT scans for a cohort of 28 patients indeed, in the previous chapter,

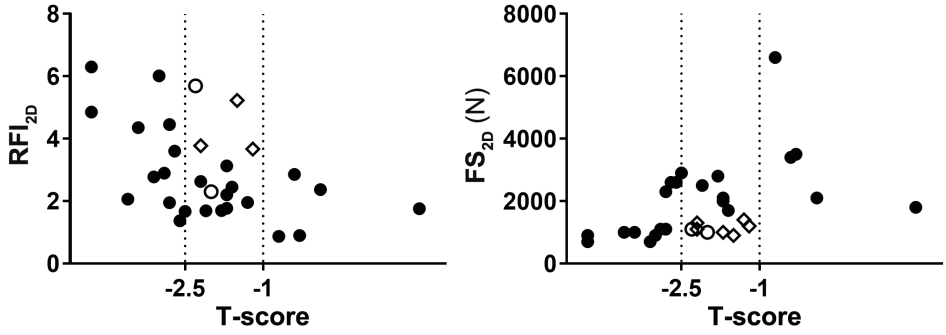

Figure 3.15: Comparison between the RFI_{2D} and FS_{2D} with the T-score outcomes. The three standard ranges of the T-score based criterion are highlighted: no osteoporosis/osteopenia: T-score > -1; osteopenia: $-2.5 <$ T-score > -1; osteoporosis: T-score < -2.5. Empty circles refer to the two fractured patients predicted values, while empty diamond show the non-osteoporotic patients looking at higher risk. Both RFI_{2D} and FS_{2D} turned out to be significantly correlated with the T-score (RFI_{2D}: $R = 0.48$, $p < 0.007$, FS_{2D} $R = 0.54$, $p < 0.002$).

3D FE models were developed aiming to explore their performances in the proximal femur fracture risk assessment. However, because CT does not represent the standard imaging technique for osteoporosis screening purposes, patient-specific three-dimensional FE models do not represent a clinically attainable risk assessment tool. This is the main reason why there has been growing interest in 2D FE models derived from DXA as well, which, on the contrary, represents the gold standard imaging technique for osteoporosis diagnosis. Hence, the main purpose of this study was the comparison between the outcomes of 2D and 3D FE models built from DXA and CT images of the same patients. The interest was in the investigation on how DXA-derived data and analyses, clinically achievable, could integrate the current standard for an enhanced fracture risk assessment. To accomplish this goal, two fracture predictors, the RFI and FS, analogously computed from the 3D models, were extracted as outcomes of the two-dimensional FE analyses. The availability of CT and DXA images for the same set of individuals is not straightforward and

only Dall'Ara et al. [115] would seem to have dealt with the comparison, *ex vivo*, of DXA and QCT FE models predictive capabilities. Other studies focused on DXA derived FE models [107, 109, 111–114], although mainly retrospectively or comparing DXA and CT in terms of geometric features computation [120].

Dall'Ara and co-workers [115] achieved better accordance between QCT- and DXA-based FE strength outcomes than ours, with the 2D strength being able to predict about 70% of the 3D-based one. Here, the 2D-based predictors could only explain from 26 to 46% of the corresponding 3D predictors variance. In [115], nonetheless, the minimum number of failed elements to be considered for fracture assessment in the 2D case was optimized with respect to the experimental data, while the 3D strength was estimated on the basis of the femoral head displacement coupled with an elastic-damage constitutive law rather than on a number of failed elements. From this perspective, the different approach employed to determine the 3D strength might also explain why, contrary to the here obtained outcomes, in [115] the DXA-based strength was generally higher than the QCT-based one. Herein, although the correlation between the DXA- and CT-based strength was significant, the modest R^2 values would hardly support the conclusion that the CT- and DXA-based analyses were equivalent. This might have been expected, since a two-dimensional model constraints the forces and the whole analysis to the frontal plane, unable to capture the realistic three-dimensionality of the problem. From this perspective, this could also be appreciated looking at Figure 3.8, where a markedly linear relation exists between the neutral- and inclined-related results. In the three-dimensional case, where the inclined configuration also involved the anteversion angle, the differences between the two distinct orientations investigated were indeed deeper. Moreover, DXA, *in vivo*, might be subjected to inconsistent positioning during the scanning, thus introducing errors into both the projected BMD and projected femoral geometry [121].

Despite the weak correlation found, paying attention to the comparison

between T-score and the RFI_{2D} and FS_{2D} (Figure 3.15), the osteopenic patients highlighted as at considerable risk of fracture with respect to the others belonging to the same T-score range were the same pointed out by the three-dimensional risk predictors: only patient 20, here highlighted by both the RFI_{2D} and FS_{2D}, was not identified as at higher risk according to the 3D results. Patient 17, healthy (T-score > -1), here showed a relatively low strength value, but not a severely high RFI, as in the 3D case. The two fractured patients, the only ones whose follow-up was known, were correctly classified by the FS_{2D}, but only one was correctly located in the high RFI_{2D} region. The other fractured patient had indeed an extremely low BMI, and the applied impact load, which was patient-specific and BMI-dependent, was consequently moderate. Hence, if the femoral strength computation, by definition, does not involve a subject-specific impact force which encompasses patient-specific anthropometric parameters [107], it here allowed to achieve a better relative risk assessment. This misclassification result, in spite of the independence between soft tissues thickness and their damping and stiffness properties found in [105], might also be due to the fact that patient-specific trochanteric soft tissues thickness was not embedded within the impact force calculation.
As far as the most relevant HSA variables are concerned, the crucial role of the CSMI and BR was here stressed as well, in accordance with the 3D outcomes. In addition, the NSA and the HAL resulted meaningful with respect to the FS_{2D} and RFI_{2D} respectively, distancing from the 3D results, where the NSA was included in the optimal RFI regression model but the HAL was not considered. The HAL, which is indeed recognized to be a sensible predictor [51, 122], is biomechanically connected to the bending moment at the neck, where, in the 2D case, the majority of the high strained elements gathered. In this regard, the two-dimensionality of the models, opposed to the CT-based ones where the inclined configuration included an anteversion angle as well, is undoubtedly presumed to have had an effect. After all, the HSA variables were computed on the same geometry which was then used for the 2D FE analyses.

If the BMD computed at the femoral neck was included in the multivariate model, the increase in the explained variance was modest (4.4% increase for the RFI_{2D} and 7.4% for the FS_{2D} respectively). However, as far as the RFI_{2D} regression model is concerned, the BMD itself was not significant within the model, and the BR at the narrow neck was the only variable with a 5% significance level. On the contrary, all the variables included in the FS_{2D} model kept their 5% significance level also after the addition of the BMD.

Follow-up information unavailability and the limited number of subjects involved represent the main limitations of this study, since they prevented the validation of the implemented models as well as the performance of more robust statistical tests. Of course, the inclusion of the two additional patients did not allow a real validation of the proposed methods, and consequently further investigations would be needed.

Herein, the CT- and DXA-based analyses did not turn out to be perfectly equivalent. This would seem to be evidence of the fact that the mechanical response of a complex three-dimensional structure cannot be accurately depicted by an equivalent two-dimensional model. Compared to CT-based three-dimensional models, 2D DXA-based FE models certainly have a number of limitations, starting from DXA projective nature, resulting in the overlapping of cortical and trabecular bone on the image plane, going to the approximation of the femur geometry to a plate with constant thickness and boundary conditions applied on the unique image plane. As a consequence, stress and strain distributions may be altered. Nevertheless, the most relevant HSA variables identified were not discordant and interestingly, the non-osteoporotic patients highlighted as at higher risk did not differ noticeably from the 3D case. In this light, Figure 3.16 stresses the synergical effect of geometry and local material properties within the bone load bearing capabilities which is captured by the 2D FE analyses. RFI_{2D} and FS_{2D} were indeed able to highlight some osteopenic patients as being at higher risk of fracture, and thus to better differentiate patients belonging to the other T-score ranges. Therefore,

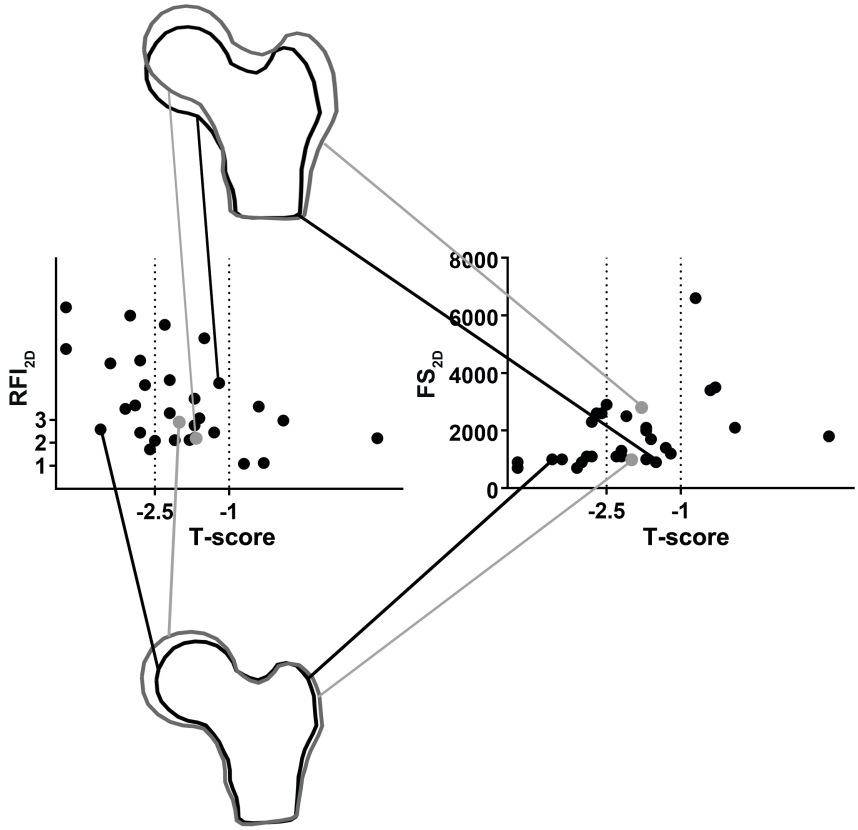

Figure 3.16: Juxtaposition of shapes related to patients with comparable T-score but different RFI/FS and vice-versa.

these results also prospectively emphasize how the T-score predictive ability could be enhanced accounting for the role played by the proximal femur shape and geometrical features in general: T-score, which accounts for the material properties alone, might indeed be supported by the inclusion of the HSA variables highlighted as the most relevant with respect to an estimated fracture risk indicator. Without any substantial modifications in the diagnostic procedure, HSA variables, already in hands of clinicians but not used practically, could be thus immediately employed, with the

potentiality of integrating and improving the current standards for risk of fracture estimation.

Appendix

When dealing with the two-dimensional modelling of solids, the plane stress and plane strain approaches are available. Within the DXA-based femur modelling, the plane stress approach is usually preferred over the plane strain one in the literature [112, 113, 115, 121]. While the plane strain approach assumes a structure has dimensions in the non-planar direction significantly larger compared to the in-plane ones, and that the strain in the out-of-plane direction is thus negligible, the plane stress assumes the opposite. In this latter, the dimensions in the out-of-plane direction, smaller with respect to those in-plane, allows to consider the stress in the out-of-plane direction negligible. Although the proximal femur does not have different orders of magnitude in its 3 dimensions, the frontal plane dimensions might be considered marginally larger than the anterior-posterior dimension, leading to the choice of a plane stress approach. Due to the different hypotheses on which the two different approaches are based, the strains formulations differ, with of course an influence on the results obtained if the two are used to solve a unique problem. Considering the reference system shown in Figure 3.17, where the out-of-plane direction is represented by the y-direction, the strain formulations in the case of plane strain would be:

$$\varepsilon_x = \frac{\sigma_x}{E} - \frac{\nu\,\sigma_y}{E} - \frac{\nu\,\sigma_z}{E} \tag{3.9}$$

$$\varepsilon_z = \frac{\sigma_z}{E} - \frac{\nu\,\sigma_x}{E} - \frac{\nu\,\sigma_y}{E} \tag{3.10}$$

$$\gamma_{xy} = \frac{2\,(1+\nu)\,\tau_{xy}}{E} \tag{3.11}$$

with $\varepsilon_y = 0$.
Differently, in the plane stress case:

$$\varepsilon_x = \frac{\sigma_x}{E} - \frac{\nu\,\sigma_z}{E} \tag{3.12}$$

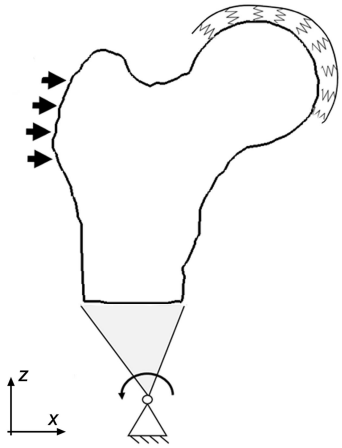

Figure 3.17: Two-dimensional profile of the proximal femur with highlighted the boundary conditions imposed as well as the considered reference system.

$$\varepsilon_y = -\frac{\nu}{E}\left(\sigma_x + \sigma_z\right) \tag{3.13}$$

$$\varepsilon_z = \frac{\sigma_z}{E} - \frac{\nu\,\sigma_x}{E} \tag{3.14}$$

$$\gamma_{xy} = \frac{2\left(1+\nu\right)\tau_{xy}}{E} \tag{3.15}$$

In this case, $\sigma_y = 0$, but the strain in the y direction is not 0.
Comparing ε_x, the strain in the loading direction, in the two cases, it is visible that in the plane strain case there is the additional contribution of the term $\frac{\nu\,\sigma_y}{E}$. Given that $\varepsilon_y = 0, \sigma_y = \nu\left(\sigma_x + \sigma_z\right)$ in the plane strain case. Hence, considering the specific boundary conditions applied, the contribution of σ_y, negative in the regions of interest, i.e. neck and intertrochanter, will make ε_x (which will be negative due to compressive state) smaller in modulus in the plane strain case with respect to the plane stress. On the other hand, σ_y will yield an higher ε_z in the plane strain case with respect to the plane stress one. Therefore, if the principal strains are taken into account, the minimum principal strain will be higher in the plane stress

case, while the maximum principal strain will be higher in the plane strain case. Given the prevailing compressive strains observable in our analyses, the adoption of the plane stress approach will then result conservative, yielding higher minimum principal strains with respect the plane strain, and therefore presumably higher RF.

Moreover, the adoption of the 3D-based failure thresholds on the 2D-based FE analyses outcomes might be considered to be conservative. The proximal femur was indeed modelled as a plate with a constant subject-specific thickness such that its cross-sectional area and area moment of inertia were as close as possible to those of a circular cross-section with diameter equal to the HSA neck width. Therefore, in the neck region, stress and strain values might be considered to be comparable to the corresponding 3D-based ones. However, in the intertrochanteric region, which represented the other highly loaded region, the real cross-section is presumably larger that that at the neck. Here, stress and strain values as computed from the 2D analyses might thus result to be over-estimated, making the adopted criteria more conservative.

Chapter 4

Statistical Shape Modelling to disclose the role of proximal femur geometry

Abstract

The role played by proximal femur morphology, despite widely investigated in the literature, has not been fully clarified yet. Hip Structural Analysis (HSA) variables, which are extracted directly from DXA images, are actually discrete and correlated measures which do not describe proximal femur geometry as a whole; on top of that, many of them are essentially derived from the image pixels intensity, and thus tightly related to the Bone Mineral Density (BMD) itself. Therefore, aiming to explore how geometry and BMD interact and contribute to the femur bone resistance to loading, statistical models of the shape, the intensity, i.e. the BMD distribution across the bone, and their combination have been here developed. First, Principal Component Analysis (PCA) was carried out, which yielded the main geometric and intensity features observable in the population. Besides, aiming to identify the most meaningful features detectable both in the morphology and BMD distribution but relevant to a fracture risk index as well, Partial Least Square (PLS) algorithm was used. The Femoral Strength (FS) computed thanks to the three-dimensional FE analyses previously presented was used as the fracture risk index. While no significant correlation was found between the FS and the main PCA shape modes, the first PCA intensity mode was strongly correlated to the FS ($R = 0.79$, $p = 0.0001$). Similarly, PLS outcomes underlined the stronger relation between intensity and FS: the first PLS intensity modes were indeed the most relevant with respect to both the intensity itself and to the FS. The first shape intensity combined PLS mode was considerably correlated with the FS ($R = 0.82$, $p < 0.0001$) and compared to the T-score, allowed a better stratification of the patients, also locating the two fractured patients in the higher risk area. Canonical Correlation Analysis eventually allowed, based on combined PLS outcomes, to predict shapes and BMD distribution associated to an increased/decreased strength: as the strength increases the femur is characterized by higher

BMD and thicker cortices and shows a wider intertrochater and a decreased neck-shaft angle.

4.1 Introduction

A fracture occurs when the external load manages to exceed the bone strength. As mentioned in the previous chapters, several factors, the bone shape among them, do represent strength vital components and might be potential fracture risk predictors [51, 123, 124]. However, in clinics, Bone Mineral Density (BMD) is currently the only variable taken into account for sake of fracture risk prediction in osteoporotic patients, although it has been shown not to be sufficient, alone, to explain the fracture occurrence. From this perspective, three-dimensional Finite Element (FE) models have been considered extremely promising, able to include patient-specific density and geometrical properties together. However, their cost-effectiveness has not been demonstrated yet [28], and their clinical employment has not taken place. Hence, with the purpose of defining the morphological features playing a role in the femur strength definition, Hip Structural Analysis (HSA) variables have been considered. They are indeed easily extracted from the routine DXA images and those most relevant to the fracture risk might be readily be integrated in the clinical decision process to integrate the T-score predictive abilities [51]. Nevertheless, HSA variables are highly correlated with each other and, in addition, they are correlated to the BMD itself, being extracted from DXA bone mineral mass distribution [51, 124]. In addition, if it is known that femur geometry might provide further insights regarding the fracture risk [125] beyond the gold standard BMD, the results in terms of the most influential HSA variables are not always consistent [51, 126].

Therefore, in order to assess the anatomical features most relevant to the risk of a fracture, Statistical Shape Models (SSMs) have been employed [124, 127]. Primarily used for segmentation [128], they have been demonstrated, together with Statistical Intensity Models (SIMs), to represent powerful tools for reconstruction and classification as well [127]. Basically, given a set of training images, statistical shape modelling allows the development of a linear model which is able to describe any new shape as the

sum of a mean and a linear weighted combination of independent modes of variation identified within the population. The corresponding weights, also called shape parameters, carry patient-specific information, providing a compact description of the patient-specific shape. Analogously, statistical intensity models are able to describe the image pixel intensities of any new image according to the same scheme.

The adoption of SSMs alone [123, 129] or in combination with SIMs [130–134] in the context of osteoporotic fracture risk estimation [124, 127] has already been proved promising, retrospectively improving the fracture risk prediction and classification compared to the sole BMD alone.
Herein, the aim was to describe the main morphological and densitometric variations in our population and particularly to establish the most crucial ones with respect to the fracture risk. In spite of the availability of the CT-based three-dimensional models, SSMs and SIMs were here developed on the DXA-derived shapes, having in mind that DXA images are what is clinically available at present.

4.2 Materials and Methods

4.2.1 The Statistical Shape Modelling framework: shapes representations as currents and template computation

The starting point for the here performed shape analysis was the mathematical framework proposed by Durrleman et al. [135], which has been published as "Deformetrica" (http://www.deformetrica.org/), an open-source code. Usually, the most common methods adopted for shapes representation prior to Statistical Shape Analysis (SSA) of anatomical districts are parametric. Hence, they rely on landmarking, which requires point-to-point correspondences between shapes, tending to be error-prone and time-consuming [136]. The here employed framework, on the contrary, does not require prior landmarking nor point-to-point correspondence of the input

shapes as it relies on mathematical currents [137] to model shapes. The method is therefore particularly attractive for landmark-poor as well as for highly variable morphologies.

The current of a generic surface S (or curve L) is defined as the flux of a test vector field $\omega \in W$ across that surface (or curve). The resulting shape T of the surface S (or of curve L) is then uniquely characterised by the variations of the flux as the test vector field varies. W, in which ω varies, is a vector space generated by a Gaussian kernel K_W with width λ_W: $K_W(\mathbf{x}, \mathbf{y}) = \exp(\frac{|\ \mathbf{x} - \mathbf{y}\ |^2}{\lambda_W^2})$ for any points $(\mathbf{x}, \mathbf{y})$. It is formally a reproducible kernel Hilbert space (r.k.h.s.).

The current of a surface (or curve) can be decomposed into an infinite set of Dirac delta currents, defined at each point of the surface (or curve) and oriented along the surface normal (or line tangent). Because computationally the surfaces (or curves) can be represented by discrete meshes (or polygonal lines), their current representation can be approximated by the finite sum

$$S^i = \sum_k \delta_{\mathbf{x}_k^i}^{\mathbf{a}_k^i} \tag{4.1}$$

with $\delta_{\mathbf{x}_k}^{\mathbf{a}_k}$ being the so called Dirac delta current. A Dirac delta current can be seen as an infinitesimal vector that is concentrated at the barycentres of the mesh faces (or at the center of each segment) $\mathbf{x}_k$ oriented along $\mathbf{a}_k$, the normal of the surface (or tangent to the line). The resolution of the currents representation is controlled by the above mentioned parameter λ_W, the width of the kernel K_W. The larger λ_W, the higher the spatial variation in the vector field and the coarser the resolution of the shape representation. Therefore, λ_W here defines the level of the shape details studied. Smaller λ_W values will allow to capture smaller differences between shapes, while larger values will discard them. Currents thus actually act as surrogate representations of shapes, characterizing them as distributions of shape features rather than as collections of points.

Once the input shapes have been modelled by means of currents, the

shape modelling framework then involves, according to the *forward* approach [138], the computation of the so called template $\overline{T}$, which represents the mean anatomical shape, and the simultaneous extraction of the transformation functions Φ^i, which map it towards each i^{th} patient-specific shape [139, 140]. Each observation T^i, i.e. each subject-specific shape, is indeed described as a deformation of the template $\overline{T}$ plus some residuals ϵ^i, accounting for features not captured by the template nor by deformations:

$$T^i = \Phi^i \cdot \overline{T} + \epsilon^i. \tag{4.2}$$

The function Φ^i is defined using the Large Deformation Diffeomorphic Metric Mapping (LDDMM) approach [136, 141], and it is parametrized by a time-varying velocity field uniquely characterized by an initial vector speed $\mathbf{v}_0^i$:

$$\mathbf{v}_0^i(\mathbf{x}) = \sum_k K_V(\mathbf{x}_k, \mathbf{x}) \boldsymbol{\beta}_{\mathbf{x}_k}^i. \tag{4.3}$$

$\mathbf{v}_0^i$ also belongs to a reproducible kernel Hilbert space V with kernel $K_V(\mathbf{x}_k, \mathbf{x}) = \exp(\frac{|\ \mathbf{x}_k - \mathbf{x}\ |^2}{\lambda_V^2})$ for any pair $(\mathbf{x}, \mathbf{x}_k)$. λ_V is the kernel width, the x are the nodes of the surface mesh (or polygonal line), x_k the point positions of the template Delta currents (also called control points). Hence, $\mathbf{v}_0^i$ is completely defined by the moment vectors $\boldsymbol{\beta}_{\mathbf{x}_k}^i$ centred at the positions $\mathbf{x}_k$ of the template delta currents, which drive the transformations of the template towards each shape and which contain the initial kinetic energy that is necessary to cover the path of a transformation from one Dirac delta current to the other. All the shape information present in the patients population, expressed as a unique deformation of the template shape, is thus contained in the patient-specific transformation functions $\Phi^i = f(\beta^i)$. The template $\overline{T}$ and the deformations Φ^i towards each patient are estimated simultaneously by means of an alternate two-step minimization strategy [140]. λ_V, the width of the kernel K_V, defines the size of the area which is deformed consistently, i.e. the rigidity of the template

deformation: the larger λ_V is, the stiffer the transformation will be, able to capture only the overall shape features variations.
Deformetrica, taking the shapes and the kernel widths λ_W and λ_V as inputs, computes and outputs the template shape, the reconstructed input shapes, the control point $\boldsymbol{x}_k$ coordinates and the corresponding moment vectors set mapping the template towards each patient-specific input shape.

4.2.2 Pre-processing

In spite of the availability of both CT-derived 3D surfaces and DXA-derived 2D profiles of the same patients, the choice was not to consider the CT-based shapes, having in mind that only 2D shapes are currently already in hands of clinicians. Therefore, the statistical shape and intensity modelling was carried out on the two-dimensional proximal femur profiles. This choice was also dictated by the possibility to better control and interpret the outcomes associated to simpler shapes with respect to the three-dimensional ones.

From the geometrical 2D models used for the previously presented FE models, the external profiles of the proximal femurs were extracted. Only the external profile was considered, since it is not straightforward to identify the cortical thickness in DXA images. Then, prior to the use of Deformetrica, shapes had to be realigned and the two kernel widths, λ_W and λ_V, needed for the shapes representation using mathematical currents and for the calculation of the transformation functions Φ , had to be set. For that purpose, a sensitivity analysis procedure similar to that presented in [142] was adopted, which basically consisted in running Deformetrica several times altering λ_W and λ_V values to achieve an optimal reconstruction of the input shapes from the moment vectors output by the software. Primarily, the 2D profiles were aligned to their shaft axis using rotation, and subsequently translated so that their distal portions of the profile were superimposed. Figure 4.1 displays the patient-specific 2D

profiles realigned and superimposed. Subsequently, the sensitivity analysis

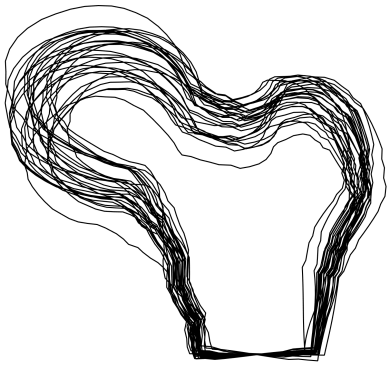

Figure 4.1: Superimposition of the patient-specific two-dimensional profiles given as input to Deformetrica after the alignment procedure.

was performed in order to assess the optimal Kernel widths. Two starting values for λ_W and λ_V were estimated as a percentage of the smallest proximal femur area [142], which yielded an initial λ_W of 17 mm and a λ_V of 68 mm. So, an initial template was computed from those values and each i^{th} patient-specific shape reconstructed from the output transformation function Φ^i, mapping the template to the input shapes. Then, λ_W and λ_V were progressively varied while evaluating the overall reconstruction error, which was computed comparing the input shapes with the reconstructed ones. Specifically, λ_W was progressively varied between 12 and 20 mm; each time, λ_V was incrementally decreased (from 68 to 35 mm) while keeping λ_W fixed. Being the input shapes two-dimensional, the computational time was always limited. Eventually, this procedure yielded the optimal λ_W and λ_V values of 17 and 38 mm respectively, which were therefore input to Deformetrica with the input shapes for the final analysis.
Furthermore, aiming to assess the final template shape was not strongly modified if one of the shapes was included or discarded, a k-fold cross-validation was carried out [142]. The whole dataset was divided into

k=14 random subsets: hence, the template was computed k times, discarding each time one different subset (i.e. 2 subjects). There were 14 resulting different templates and the relative distances among them were computed, paying attention to both the largest and the average distance value computed for each template. The highest values were 1.9 mm and 0.53 mm for the largest and average distances respectively, which were judged satisfactory to say that no subject did affect the template construction. Therefore, after Deformetrica was run, the template shape and the moment vectors set, encompassing the patient-specific shape-features, were ready to be used for the statistical shape analysis. Prior to the post-processing phase, the presence of shapes yielding a reconstruction error higher than 4 times the average reconstruction error was verified in order to assess the presence of potential outliers.

4.2.3 Post-processing

Statistical Shape Models (SSMs) and Statistical Intensity Models (SIMs) are modelling frameworks which are both based on the achievement of the average shape or intensity (here represented by the pixel-by-pixel BMD map) computed from a specific population, together with the corresponding main modes of variation of the shape or intensity from the mean. The idea is that by selecting a limited number of modes, the shape and the intensity distribution of any individual belonging to a specific population can be described.
Herein, two different approaches were employed to build SSMs ans SIMs. First of all, Principal Component Analysis (PCA) was carried out, which allowed to extract the main shape and BMD distribution features observable in the input population. However PCA by itself is only able to extract the directions, or modes, of higher variability, without accounting for an external variable of interest. This is the reason why also Partial Least Square (PLS) algorithm was adopted. PLS takes indeed one predictors matrix and one response variable matrix as inputs, identifying the main

features of the predictors matrix being relevant to the response variable as well. Hence, it was able to identify the main (shape and BMD distribution) features which were simultaneously also the most relevant to the fracture risk, taken as the response variable. Below (Figure 4.2), a schematic pipeline is presented, which shows the statistical modelling procedure which will be more deeply tackled in the following sections. Within

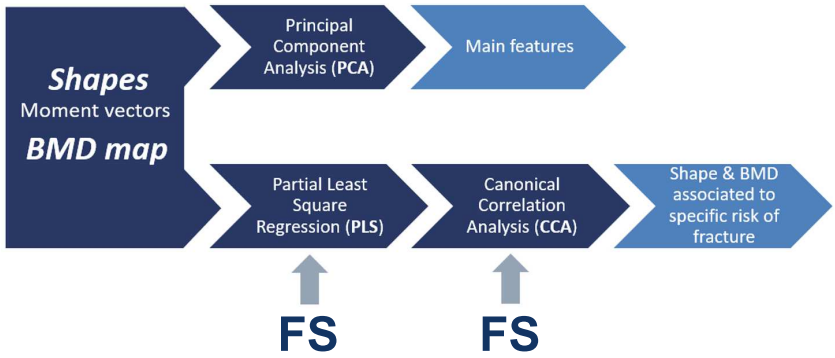

Figure 4.2: The SSM and SIM pipeline: using PCA, only the main features in terms of morphology and BMD distribution were extracted. PLS, instead, getting an external variable as input as well, yielded the main features most relevant to it too. Subsequently, Canonical Correlation Analysis, based on PLS results, allowed the prediction of the shape and intensity (BMD) distribution based on a decreased/increased FS value.

PLS, the Femoral Strength (FS) value extracted from the CT-based FE analyses (FS_{3D}) was chosen as the response variable. Being extracted from more comprehensive and realistic models compared to those based on DXA, it was indeed judged more reliable. However, because it could be computed for the 28 patients only, the overall statistical shape and intensity modelling was carried out neglecting the two additional fractured patients both within PCA and PLS, for sake of consistency.

Principal Component Analysis (PCA)

PCA is a statistical technique which allows highly dimensional datasets to be represented in a space where their variance is maximal and thus

to be decomposed into their most significant components, yielding a reduced order model of the original data. Conceptually, PCA performs a variance maximizing rotation of the original variable space, identifying the bases of a new space of the variables where their variance is maximised (Figure 4.3) [143]. Starting from the variance maximisation objec-

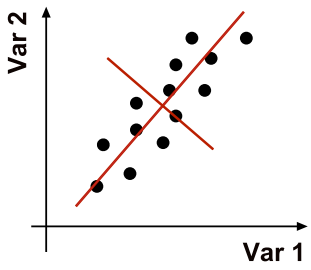

Figure 4.3: Simple graphical example of a 2D dataset PCA: in red, the first two principal directions along which the dataset variance is maximal.

tive ($\max_{|\boldsymbol{q}|=1} var(\mathbf{X}\boldsymbol{q})$, $\boldsymbol{q}$ being the sought basis and $\mathbf{X}$ a generic input variable), the problem can be converted to an eigenproblem to be solved with respect to the covariance matrix $\mathbf{S}$ of $\mathbf{X}$ ($\mathbf{S}\,\boldsymbol{q} = \lambda\,\boldsymbol{q}$) [128]. Gathering the input variables in a $N \times n$ matrix $\mathbf{X}$, with N being the number of observations and k the number of variables, PCA then involves the computation of the eigenvectors $\boldsymbol{q}$ and eigenvalues λ of its coviariance matrix. The former represent the principal modes of variation (also called PCA loadings), i.e. the orthogonal directions, or bases, along which the variance is maximised; the latter indicate the fraction of the total variance explained by each mode. The PCA modes are automatically ordered according to a decreasing explained variance. Usually, only the most influential modes, i.e. those together explaining a specific percentage $\pi\%$ of the total variance, are retained, discarding the others, and therefore yielding a reduced representation of the original dataset.

Having available not only information about the proximal femur shape

of our population, output by Defometrica, but also the local BMD map, PCA was here applied both on the shape and on the density distribution.

PCA-based statistical models of shape Aiming at the extraction of the main geometrical attributes observed in the cohort, a SSM was developed using PCA. Specifically, PCA was performed on the moment vectors $\boldsymbol{\beta}$ output by Deformetrica, which, as previously explained, contain patient-specific anatomical information referred to the template. PCA was directly applied on the centred moment vectors matrix $\mathbf{X}_\beta$ expressed as $\mathbf{X}_\beta = [\widetilde{\boldsymbol{\beta}^1}; ...; \widetilde{\boldsymbol{\beta}^N}]$, with N being the number of observations, i.e. the total number of patients included, and $\widetilde{\boldsymbol{\beta}^i} = \boldsymbol{\beta}^i - \overline{\boldsymbol{\beta}}$ the centred moment vectors set of the i^{th} patient. Hence, the i^{th} row of the matrix $\mathbf{X}$ contains the $1 \times 2k$ sized centred i^{th} moment vectors expressed as pairs of x, y coordinates: $\widetilde{\boldsymbol{\beta}^i} = [\widetilde{\beta^i_{x1}}, \widetilde{\beta^i_{y1}}, ..., \widetilde{\beta^i_{xk}}, \widetilde{\beta^i_{yk}}]$, where k is the λ_V-dependent number of control points on which the k moment vectors, 25 in this case, were centred.
PCA was performed solving the eigenvalue problem relative to the $2k \times 2k$ covariance matrix of the $\mathbf{X}_\beta$ matrix. It resulted in a set of $N-1$ eigenvalues λ^S and corresponding eigenvectors $\boldsymbol{q}^S$, where the apex S is used to refer to the shape modelling distinguishing it from the subsequent intensity modelling. The eigenvectors $\boldsymbol{q}^S$, i.e. the deformation modes, represent the bases of the space where the moment vectors variance is maximal, and their corresponding eigenvalues λ^S are equivalent to the variance described by each deformation mode [128]. The principal modes are ordered in descending order according to the percentage of shape variation explained. Hence, as previously mentioned, only the first c PCA modes, explaining a specific $\pi^S\%$ of the total shape variability, were considered in the subsequent analysis. The cumulative explained variance was simply calculated as $\pi^S = \dfrac{\sum_{m=1}^{c} \lambda^S_m}{\sum_{m=1}^{N-1} \lambda^S_m} \cdot 100$, λ^S_m being the variance explained by each m^{th} mode.
In this way, any set of subject-specific moment vectors $\widetilde{\boldsymbol{\beta}^i}$ parametrizing

the deformation of the template towards the i^{th} shape can be expressed as the sum of the average moment vector $\overline{\boldsymbol{\beta}}$ and the weighted linear combination of the deformation modes according to Equation 4.4:

$$\boldsymbol{\beta}^i = \overline{\boldsymbol{\beta}} + \boldsymbol{\Phi}^S \mathbf{b}^{S,i} = \overline{\boldsymbol{\beta}} + \sum_{m=1}^{c} b_m^{S,i} \boldsymbol{q}_m^S, \tag{4.4}$$

where the weighting factors $b_m^{S,i}$, also called shape parameters, can be gathered in the subject-specific vector $\mathbf{b}^{S,i}$ with length c, which will be addressed as shape vector, and each deformation mode $\boldsymbol{q}_m^S$ can be gathered in the matrix of eigenvectors $\boldsymbol{\Phi}^S$. Each shape vector can be obtained projecting the subject-specific moment vectors array $\boldsymbol{\beta}^i$ onto the PCA subspace defined by the selected c deformation modes: it will then have c components (or shape parameters), one for each PCA mode. Each shape vector m^{th} component describes the extent to which the template has to be deformed along each m^{th} mode to match the i^{th} subject shape, and can therefore be considered as a quantitative representation of the subject-specific shape attributes encompassed in each mode. As a whole, the i^{th} shape vector might be regarded as a low-dimensional representation of the i^{th} subject-specific shape.

To visualize the effect of each individual m^{th} specific deformation mode on the proximal femur template separately, the equivalent set of moment vectors $\boldsymbol{\beta}^m$, parametrizing the corresponding template transformation only along the m^{th} mode can be determined. Each m^{th} mode $\boldsymbol{q}_m^S$ can indeed be considered, and its corresponding weighting factor b_m^S arbitrarily varied in the range $-l\sqrt{\lambda_m^S}$, $l\sqrt{\lambda_m^S}$, with l generally equal to 1-3 (Equation 4.5) [139, 142].

$$\boldsymbol{\beta}^m = \overline{\boldsymbol{\beta}} \pm l\sqrt{\lambda_m^S}\boldsymbol{q}_m^S, \tag{4.5}$$

Hence, substituting $\boldsymbol{\beta}^m$ of Equation 4.5 in Equation 4.3, the initial velocity to be used in order to deform the template along the mode of interest can be determined.

PCA-based statistical models of intensity SSMs yield information regarding the anatomical variations within a population, but do not consider the other crucial determinant of bone strength, which is represented by the density distribution within bones. SIMs, on the other hand, analogously to SSMs, allow to obtain the average density distribution together with the main modes of variations of the density distribution itself.
To generate a SIM, local density information is needed, as well as a consistent spatial correspondence of the locations where the BMD is sampled among the input patients. With this aim, the outcomes derived from Deformetrica were used in order to morph the meshed template towards each patient and therefore to obtain correspondent elements on which the BMD values sampling was based. The template, i.e. the mean anatomical shape yielded by Deformetrica, was meshed with 1 mm edge triangular elements. Subsequently, each node of the template was mapped to each different patient-specific shape so that the template mesh could be morphed towards each patient. To do so, the patient-specific moment vectors $\boldsymbol{\beta}$, output by Deformetrica with the template, were used to compute the initial velocity $\mathbf{v}_0^i$ values (Equation 4.3) to displace each template node. In this way, a unique mesh was morphed towards each patient and could be exploited to build consistent patient-specific BMD arrays. As only one single mesh node was identified in every pixel, the BMD of each pixel was simply assigned to the corresponding node.
Hence, the patient-specific BMD arrays $\boldsymbol{g}$ were organized in a $N \times n$ matrix $\mathbf{G}$, N being the number of observations (i.e. the patients), n the number of variables, i.e. the total number of nodes ($n = 16208$). No density values normalization procedure [124] was performed, since the intensity values were actually BMD values instead of grey values. After centring the matrix with respect to the average BMD values array ($\overline{\boldsymbol{g}}$), the PCA was carried out following the procedure suggested and demonstrated by Cootes et al., [128], owing to the much higher number of variables than observations. Basically, instead of solving the eigenproblem for the $n \times n$

covariance matrix $\mathbf{S}= \mathbf{G}\cdot\mathbf{G}'$, the eigenproblem can be solved for the covariance matrix $\mathbf{T}= \mathbf{G}'\cdot\mathbf{G}$ which is much smaller ($N \times N$). The eigenvalues of $\mathbf{T}$ are exactly the same as those of $\mathbf{S}$, and therefore they already represent the variance λ^G explained by the sought appearance modes $\boldsymbol{q}^G$ (where the apex G refers to the SIM); conversely, the main modes of variation of the BMD distribution $\boldsymbol{q}^G$ can be identified as $\boldsymbol{q}^G = \frac{\mathbf{G}'\boldsymbol{e}^G}{\sqrt{N-1}\,\lambda^G}$, where $\boldsymbol{e}^G$ represent the eigenvectors of the matrix $\mathbf{T}$.

Analogously to the statistical shape modelling approach, any i^{th} patient-specific BMD distribution will then be described as a linear combination of the c modes explaining a certain percentage π^G of the total intensity variance:

$$\boldsymbol{g}^i = \overline{\boldsymbol{g}} + \boldsymbol{\Phi}^G \boldsymbol{b}^{G,i} = \overline{\boldsymbol{g}} + \sum_{m=1}^{c} b_m^{G,i}\, \boldsymbol{q}_m^G, \tag{4.6}$$

where, coherently with the previous SSM, the weighting terms (or intensity parameters) $b_m^{G,i}$ can be gathered in the intensity vector $\boldsymbol{b}^{G,i}$, describing the contribution of each principal mode of variation of BMD to the patient-specific i^{th} BMD distribution. $\boldsymbol{\Phi}^G$ is the matrix where the eigenvectors $\boldsymbol{q}^G$ (the principal modes of intensity variations) are collected.

Eventually, the effect of each individual m^{th} mode on the whole BMD distribution can be visualized considering only that mode and letting the weighting factor vary in the range $-l\sqrt{\lambda_m^G}$, $l\sqrt{\lambda_m^G}$:

$$\boldsymbol{g}^m = \overline{\boldsymbol{g}} \pm l\sqrt{\lambda_m^G}\boldsymbol{q}_m^G. \tag{4.7}$$

PCA-based combined models of shape and density In the previous sections, where SSMs and SIMs have been presented, it has been shown that they allow the construction of any shape or intensity instance using a set of shape and intensity parameters $\boldsymbol{b}^S$ and $\boldsymbol{b}^G$. Aiming to make the representation more compact and complete, the two can be unified, achieving a so called Statistical Shape Intensity Model (SSIM) [144].

The shape and intensity vectors can indeed be gathered in two matrices $\mathbf{B}^S$

and $\mathbf{B}^G$, containing all the available patient-specific shape and intensity vectors as rows, and concatenated into the matrix $\mathbf{B}$:

$$\mathbf{B} = \begin{pmatrix} \mathbf{W}_s \, \mathbf{B}^S \\ \mathbf{B}^G \end{pmatrix} = \begin{pmatrix} \mathbf{W}_s \, \mathbf{\Phi}^{S\prime} \, \mathbf{X}'_\beta \\ \mathbf{\Phi}^{G\prime} \, \mathbf{G}' \end{pmatrix}. \tag{4.8}$$

$\mathbf{W}_s$, which is needed as a weighting factor between $\mathbf{B}^S$ and $\mathbf{B}^G$, which have different units, can be computed as $\mathbf{W}_s = r\,\boldsymbol{I}$, r being the ratio $\frac{\sum_i \lambda_i^G}{\sum_i \lambda_i^S}$ [144] between the total variance in intensity and the total variance in shape.
If a third PCA on the matrix $\mathbf{B}$ is carried out, the relation

$$\mathbf{B} = \mathbf{\Phi}^C \, \mathbf{W} \tag{4.9}$$

is obtained, where $\mathbf{W}$ is the matrix gathering the patient-specific combined shape-intensity vectors $\boldsymbol{w}$, and $\mathbf{\Phi}^C$ represents the eigenvectors matrix. Therefore, a complete model instance covering the shape and the texture can be created using $\boldsymbol{w}$:

$$\boldsymbol{\beta} = \overline{\boldsymbol{\beta}} + \mathbf{\Phi}^S \mathbf{W}_S^{-1} \mathbf{\Phi}^{C,S} \boldsymbol{w} \tag{4.10}$$

$$\boldsymbol{g} = \overline{\boldsymbol{g}} + \mathbf{\Phi}^G \mathbf{\Phi}^{C,G} \boldsymbol{w} \tag{4.11}$$

where

$$\mathbf{\Phi}^C = \begin{pmatrix} \mathbf{\Phi}^{C,S} \\ \mathbf{\Phi}^{C,G} \end{pmatrix}. \tag{4.12}$$

Partial Least Square (PLS)

PCA allows the identification of the main modes of variation of the shape and of the intensity detectable in the input population, without any

association to an external variable, such as the fracture risk. Actually, it allowed to describe the population in terms of the shape and BMD distribution variability, without being able to relate the two to the fracture risk and thus to identify those possibly playing a role within it. Nonetheless, this work mainly aimed at the identification of fracture-prone morphological attributes of the proximal femur. Hence, in order to overcome the aforementioned PCA limitations and account for shape and material features relevant to an external response variable too, Partial Least Square (PLS) Regression was carried out [145]. The method, similarly to PCA, identifies new bases of the space of predictors, which, nonetheless, are relevant to an external response variable as well. To do so, given two sets of centred variables, a generic predictors matrix $\mathbf{X}_C$ and a response variables matrix $\mathbf{Y}_C$, the space of maximal covariance between them is computed. Mathematically, PLS estimates the weights vectors $\mathbf{r}$ and $\mathbf{s}$ which satisfy:

$$\max_{|\boldsymbol{r}|=|\boldsymbol{s}|=1} cov(\mathbf{X}_C\,\boldsymbol{r}, \mathbf{Y}_C\,\boldsymbol{s}) = \max_{|\boldsymbol{r}|=|\boldsymbol{s}|=1} var(\mathbf{X}_C\,\boldsymbol{r}) corr(\mathbf{X}_C\,\boldsymbol{r}, \mathbf{Y}_C\,\boldsymbol{s})^2 var(\mathbf{Y}_C\,\boldsymbol{s}), \tag{4.13}$$

as opposed to PCA, which solves $\max_{|\boldsymbol{r}|=1} var(\mathbf{X}_C\,\boldsymbol{r})$. The PLS modes $\boldsymbol{t}$ and $\boldsymbol{u}$ are then found weighting $\mathbf{X}_C$ and $\mathbf{Y}_C$ by $\boldsymbol{r}$ and $\boldsymbol{s}$ within an iterative process (Table 4.1) which loops until all the PLS modes are extracted and where, at each step, the variance explained by $\boldsymbol{r}$ and $\boldsymbol{s}$ is removed from the original data (deflation). Mathematically, this can be written as:

$$\mathbf{X}_C = \mathbf{T}\mathbf{P}^T + \mathbf{E} \tag{4.14}$$

$$\mathbf{Y}_C = \mathbf{U}\mathbf{Q}^T + \mathbf{F}. \tag{4.15}$$

$\mathbf{T}$ and $\mathbf{U}$ are the PLS components matrices, $\mathbf{P}$ and $\mathbf{Q}$ contain the PLS modes, or loadings (contrary to PCA loadings, the PLS ones are not necessary orthogonal); $\mathbf{E}$ and $\mathbf{F}$ are residual matrices. The PLS components also need to satisfy the regression equation $\mathbf{U} = \mathbf{T}\mathbf{D} + \mathbf{G}$, $\mathbf{D}$ being a diagonal matrix of weights and $\mathbf{G}$ the matrix of residuals.

Herein, PLS was performed both on the centred moment vectors matrix

Table 4.1: PLS space decomposition (PLS1 algorithm).

Inputs: $\mathbf{X}_C$, $\mathbf{Y}_C$, number of PLS modes p to extract ($p = N - 1$)

for $n = 1$ to p **do**

$\boldsymbol{r}^n \leftarrow$ *first eigenvector of* $\mathbf{X}_C^{n\,T}\mathbf{Y}_C^n\mathbf{Y}_C^{n\,T}\mathbf{X}_C^n$ (*from* [145])

$\mathbf{t}^n \leftarrow \mathbf{X}_C^n\boldsymbol{r}^n/|\boldsymbol{r}^n| \quad n^{th}$ *PLS component of* $\mathbf{X}_C$

$\mathbf{s}^n \leftarrow \mathbf{Y}_C^n\boldsymbol{t}^n/(t^{n\,T}t^n)$

$\mathbf{u}^n \leftarrow \mathbf{Y}_C^n\boldsymbol{s}^n/|\boldsymbol{s}^n| \quad n^{th}$ *PLS component of* $\mathbf{Y}_C$

$\mathbf{p}^n \leftarrow \mathbf{X}_C^n\boldsymbol{t}^n/(\boldsymbol{t}^{n\,T}\boldsymbol{t}^n) \quad n^{th}$ *PLS loading of* $\mathbf{X}_C$

$\mathbf{q}^n \leftarrow \mathbf{Y}_C^n\boldsymbol{u}^n/(\boldsymbol{u}^{n\,T}\boldsymbol{u}^n) \quad n^{th}$ *PLS loading of* $\mathbf{Y}_C$

$\mathbf{X}_C^{n+1} \leftarrow \mathbf{X}_C^n - \boldsymbol{t}^n\boldsymbol{p}^{n\,T} \quad$ *deflation of* $\mathbf{X}_C$

$\mathbf{Y}_C^{n+1} \leftarrow \mathbf{Y}_C^n - \boldsymbol{t}^n[\boldsymbol{t}^{n\,T}\mathbf{Y}_C^n/(\boldsymbol{t}^{n\,T}\boldsymbol{t}^n)] \quad$ *deflation of* $\mathbf{Y}_C$

end

$\mathbf{X}_\beta$ and the centred BMD vectors matrix $\mathbf{G}$, taken as predictor matrices, with the centred Femoral Strength (FS_{3D}) vector taken as the response variable. The purpose was indeed the extraction of the dominant shape and intensity features most correlated to the risk of proximal femur fracture. Because the response variable was only one, the PLS1 algorithm, summarized in Table 4.1, was implemented [146].

The choice of the sole FS_{3D} as the external variable was made aiming to assess the morphological and intensity features relevant to the bone mechanical strength. Therefore, the Risk Factor Index (RFI), which also involved a patient-specific impact load, was not included in the PLS-based models. Moreover, the FS_{3D}, extracted from the three-dimensional CT-based FE analyses instead of the DXA-based ones was used. Indeed, not only was it the outcome of more realistic models, but the FS_{2D} would also have been naturally correlated to the 2D shape and BMD information used herein. In the following, the notation FS will be thus always referred to the FS_{3D}.

PLS-based statistical models of shape Aiming to investigate the main shape features most relevant to the FS as a surrogate of the risk of fracture, PLS was performed considering it as the response variable and taking the $N \times 2k$ moment vectors matrix $\mathbf{X}_\beta$ as the predictors matrix. The PLS1 algorithm allowed the extraction of the PLS shape modes $\mathbf{P}^S$, which are automatically ordered by decreasing variance and covariance with respect to the response variable. Therefore, the first c PLS components, explaining simultaneously $\pi_{\mathbf{X}_\beta}\%$ of the variance in $\mathbf{X}_\beta$ and $\pi_{FS}\%$ of the total FS variance could be selected. In analogy with the PCA-based statistical shape modelling, any i^{th} moment vectors set guiding the template deformation towards a new shape could be seen as:

$$\boldsymbol{\beta}^i_{PLS} = \overline{\boldsymbol{\beta}} + \mathbf{P}^S \boldsymbol{t}^{S,i} = \overline{\boldsymbol{\beta}} + \sum_{n=1}^{c} t^{S,i}_n \boldsymbol{p}^S_n. \tag{4.16}$$

where the shape vectors $\boldsymbol{t}^{S,i}$ are actually represented by the $\boldsymbol{t}^{i\prime}s = t^i_{n\ n=1\ldots c}$ of PLS1 algorithm (Table 4.1). Again, each component $t^{S,i}_n$ of $\boldsymbol{t}^{S,i}$ is a PLS shape parameter and delineates the contribution of each PLS mode on the patient-specific shape. As visible from equation 4.14, they do represent indeed the projection of the predictors matrix $\mathbf{X}_\beta$ on the new space defined by the PLS modes (or loadings) contained in the matrix $\mathbf{P}^S$. The visualization of the n^{th} PLS deformation mode, eventually, is achieved deforming the template using the moment vectors determined as:

$$\boldsymbol{\beta}^n_{PLS} = \overline{\boldsymbol{\beta}} \pm l\sqrt{\lambda^S_{PLS,n}}\boldsymbol{p}^S_n, \tag{4.17}$$

$\lambda^S_{PLS,n}$ being the variance explained by the n^{th} PLS mode.

PLS-based statistical models of intensity Interested in the main BMD distribution features most related to the fracture risk too, PLS was performed taking as the predictors matrix the patient-specific BMD vectors $\mathbf{g}$ gathered in the matrix $\mathbf{G}$. Hence, the PLS modes $\mathbf{p}^G$ together with the corresponding PLS components $\mathbf{t}^G$ (PLS intensity vectors) could be

identified. This then yielded the possibility to represent the i^{th} intensity instance as the linear combination of the c modes explaining simultaneously $\pi_{\mathbf{G}}\%$ of the variance in $\mathbf{G}$ and $\pi_{FS}\%$ of that of the FS:

$$\boldsymbol{g}^{i}_{PLS} = \overline{\boldsymbol{g}} + \mathbf{P}^{G}\boldsymbol{t}^{G,i} = \overline{\boldsymbol{g}} + \sum_{n=1}^{c} t^{G,i}_{n}\,\boldsymbol{p}^{G}_{n}. \tag{4.18}$$

Also, each n^{th} PLS intensity mode could be visualized individually:

$$\boldsymbol{g}^{n}_{PLS} = \overline{\boldsymbol{g}} \pm l\sqrt{\lambda^{G}_{PLS,n}}\,\boldsymbol{p}^{G}_{n}, \tag{4.19}$$

with $\lambda^{G}_{PLS,n}$ the variance explained by the n^{th} PLS mode.

PLS-based combined models of shape and density Eventually, in order to unify the PLS-based shape and intensity models in a unique SSIM, coherently with the PCA-based SSIM, a third PLS was carried out on the concatenated shape and intensity shape vectors

$$\mathbf{T}^{C} = \begin{pmatrix} \mathbf{W}_{PLS,\,s}\,\mathbf{T}^{S} \\ \mathbf{T}^{G} \end{pmatrix} = \begin{pmatrix} \mathbf{W}_{s}\,\mathbf{P}^{S\prime}\,\mathbf{X}'_{\beta} \\ \mathbf{P}^{G\prime}\,\mathbf{G}'. \end{pmatrix} \tag{4.20}$$

$\mathbf{W}_{PLS,\,s}$, the weighting factor between $\mathbf{P}^{S}$ and $\mathbf{P}^{G}$, characterized by different units, was computed as illustrated before: $\mathbf{W}_{PLS,\,s} = r\,\boldsymbol{I}$, r being the ratio $\dfrac{\sum_i \lambda^{G}_{PLS,i}}{\sum_i \lambda^{S}_{PLS,i}}$ [144] between the total variance in intensity and the total variance in shape.

As in the PCA SSIM, relation 4.21 is obtained performing a third PLS on the matrix $\boldsymbol{T}^{C}$, :

$$\mathbf{T}^{C} = \mathbf{P}^{C}\,\mathbf{W}_{PLS}, \tag{4.21}$$

where $\mathbf{W}_{PLS}$ is the matrix of combined model vectors $\boldsymbol{w}_{PLS}$, and $\mathbf{P}^{C}$ is the loadings matrix of the combined shape and intensity vectors. Therefore, a PLS-based complete model instance unifying the shape and the intensity

can be created using the PLS combined shape-intensity vectors $\boldsymbol{w}_{PLS}$:

$$\boldsymbol{\beta} = \overline{\boldsymbol{\beta}} + \mathbf{P}^{S}\mathbf{W}_{PLS,s}^{-1}\mathbf{P}^{C,S}\boldsymbol{w}_{PLS} \tag{4.22}$$

$$\boldsymbol{g} = \overline{\boldsymbol{g}} + \mathbf{P}^{G}\mathbf{P}^{C,G}\boldsymbol{w}_{PLS} \tag{4.23}$$

where

$$\mathbf{P}^{C} = \begin{pmatrix} \mathbf{P}^{C,S} \\ \mathbf{P}^{C,G} \end{pmatrix}. \tag{4.24}$$

Canonical Correlation Analysis (CCA)

With the purpose of predicting the shape associated to an increased or decreased risk of fracture (i.e. to different values of the FS), Canonical Correlation Analysis (CCA) was implemented, having in mind the possibility to build a dataset of different shapes with different BMD distributions associated to different levels of the fracture risk, to be used within a clinical context, where they would be compared to the patient-specific DXA.
Given two sets of variables, the technique computes the bases of a new space, addressed as the canonical space, where the correlation between the two is maximal. In this study, the idea was to estimate the extent to which the template had to be altered in term of both the shape and the BMD distribution along each PLS mode as the FS value was increased or decreased with respect to its mean.
To achieve this goal, i.e. the development of new instances both in terms of moment vectors and intensity vectors, the PLS subspace previously determined within the PLS shape-intensity model was used. Recalling Equations 4.22 and 4.23 indeed, any new instance could be generated varying the $\boldsymbol{w}_{PLS}$ vector entries. Hence, taking advantage of the shape-intensity PLS subspace, only the shape-intensity parameter values w_{PLS}^{n} for each n^{th} mode corresponding to increased and decreased FS values had to be

assessed.
Then, CCA was applied on the centred PLS combined shape-intensity vectors matrix $\mathbf{W}_{PLS}$ and the FS vector. CCA allowed the identification of the space of maximal correlation between $\mathbf{W}_{PLS}$ and FS and consequently, of their representation in the canonical space, where they were maximally correlated:

$$\mathbf{Z} = \mathbf{W}_{PLS} \cdot \mathbf{A}, \tag{4.25}$$

$$\mathbf{V} = Y \cdot \mathbf{B}. \tag{4.26}$$

$\mathbf{Z}$ and $\mathbf{V}$ represent the canonical variates, i.e. the original variables in the canonical space; $\mathbf{A}$, $\mathbf{B}$ are the canonical directions, i.e. the canonical space bases. In this specific case, being FS one single variable, only the shape vectors matrix $\mathbf{W}_{PLS}$ needed to be transferred to the canonical space through the matrix $\mathbf{A}$ to achieve maximal correlation. Once in the canonical space, a regression analysis allowing the estimation of $\mathbf{Z}$ from the FS was performed. Hence, given a new FS value, the sought corresponding shape vector $\boldsymbol{z}$ could be identified. Eventually, inverting Equation 4.25, $\boldsymbol{z}$ could eventually be brought back to the original space. The desired $\boldsymbol{w}_{PLS}^{CCA}$ is therefore identified and a new set of moment vectors $\boldsymbol{\beta}^{CCA}$ together with a new intensity vector $\boldsymbol{g}^{CCA}$ can be determined substituting the newly identified shape vectors within Equations 4.22 and 4.23.

4.3 Results

Deformetrica, run with the optimal identified λ_W and λ_V parameters, output the template, the control points coordinates, as well as the corresponding patient-specific sets of moment vectors β. Due to the specific λ_V value used, 25 moment vectors ($\boldsymbol{x}$, $\boldsymbol{y}$ pairs) per patient were obtained. Therefore, the moment vectors matrix $\mathbf{X}_\beta$ was a 28×50 matrix. Because of the choice to use the 3D-based FS as the external variable within PLS, which was available only for the 28 patients, and for sake of consistency between PLS and PCA, the whole analysis was indeed carried out only on

28 patients, thus neglecting the two fractured ones. Besides, patient 27 was excluded from the whole statistical modelling since the shape reconstruction error was 4 times higher than the average error.

4.3.1 PCA

PCA was first performed on the 27×50 $\mathbf{X}_\beta$ matrix. The first 7 PCA modes were selected, able to explain 96.34% of the total shape variance (Figure 4.4). The shape variability captured by the 7 modes can be visualized in Figure 4.5, as deformation of the template along each mode between $-c\sqrt{\lambda^S}$, $c\sqrt{\lambda^S}$, with $c = 3$. Mode 1, which embodies the most variable features within the considered population, appears to be related to the size; in addition, together with mode 2, it results significantly correlated with the HAL (mode 1: $R = -0.54$, $p = 0.0035$; mode 2: $R = 0.66$, $p = 0.0002$), thus suggesting HAL is a highly variable feature as well. The first two modes together were indeed able to gather 80% of the total shape variance. Interestingly, the only mode correlated to one of two available fracture risk indices was mode 6, showing a significant correlation with the RFI ($R = -0.43$, $p = 0{,}26$) only. This mode, although suggesting slight variations in the neck width and greater trochanter asperity, did

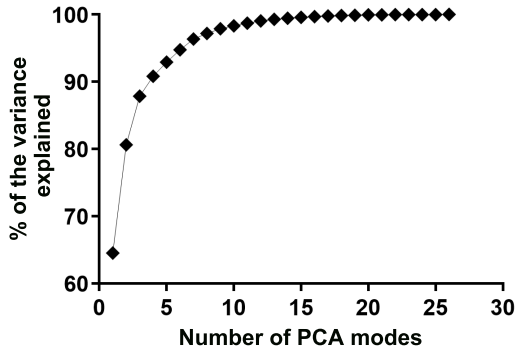

Figure 4.4: Cumulative percentage of variance explained by the PCA shape modes. 7 components explained more then 95% of the total shape variance.

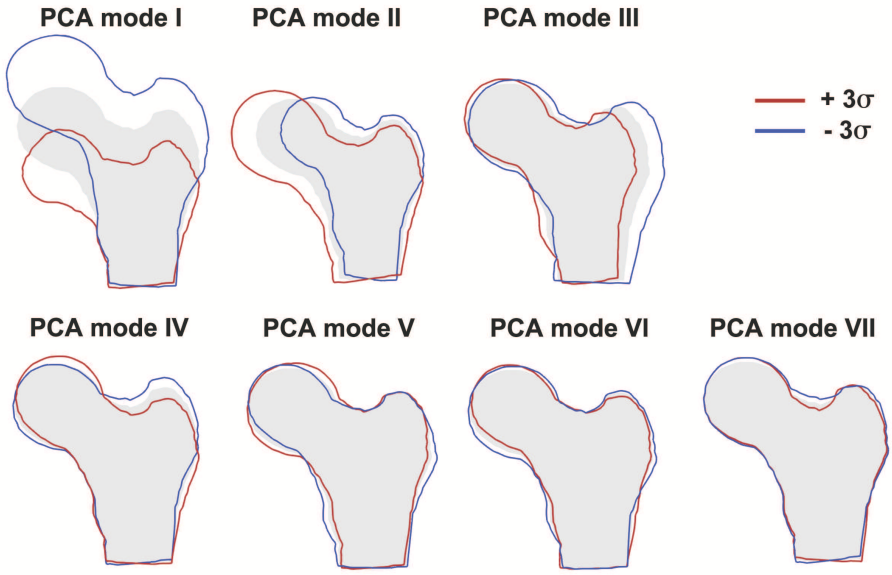

Figure 4.5: Visualization of the first 7 PCA deformation modes.

not highlight clearly distinctive features.

As far as the BMD distribution is concerned, the subject specific BMD arrays were gathered in the 27×16208 matrix $\mathbf{G}$. A total of 21 PCA modes were necessary to explain at least 95% of the density distribution variability, 9 modes managed to explain 75% of it (Figure 4.6). The first 8 in-

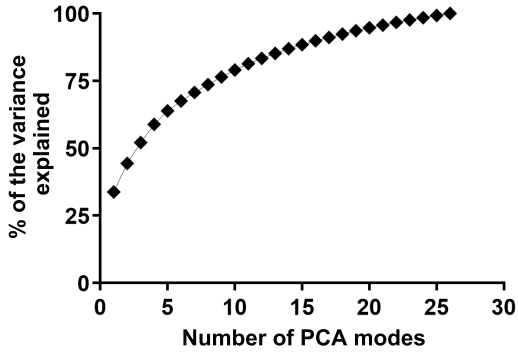

Figure 4.6: Cumulative percentage of variance explained by the PCA intensity modes. 9 components explained 75% of total BMD distribution variance, 21 modes were necessary to account for 95% of it.

tensity modes are displayed in Figure 4.7, where also the template shape with the average BMD map is shown. Accounting for the first 4 PCA intensity modes only, 60% of the intensity variation could be explained. The first mode, which highlights a general increase/decrease of the BMD within the whole proximal femur, was, as expected, thus significantly correlated ($R > 0.5$, $p < 0.01$) with the T-score (total femur) and BMD (HSA-derived BMD, see Table 1.3), but also to BR and CSMI, stressing their tight link with the intensity distribution on which their computation relies. At the same time, it was also correlated to both the RFI and FS ($R = 0.6264$, -0.6915 and $p = 0.0006$, 0.0001, respectively), pointing out the crucial role of the material properties. Mode 2 highlights a decreased BMD in the trochanteric fossa region, which also comes with a thicker cortex layer medially in the femur distal portion. Similarly, mode 3 points out a decreased BMD area in the greater trochanter region. Interestingly,

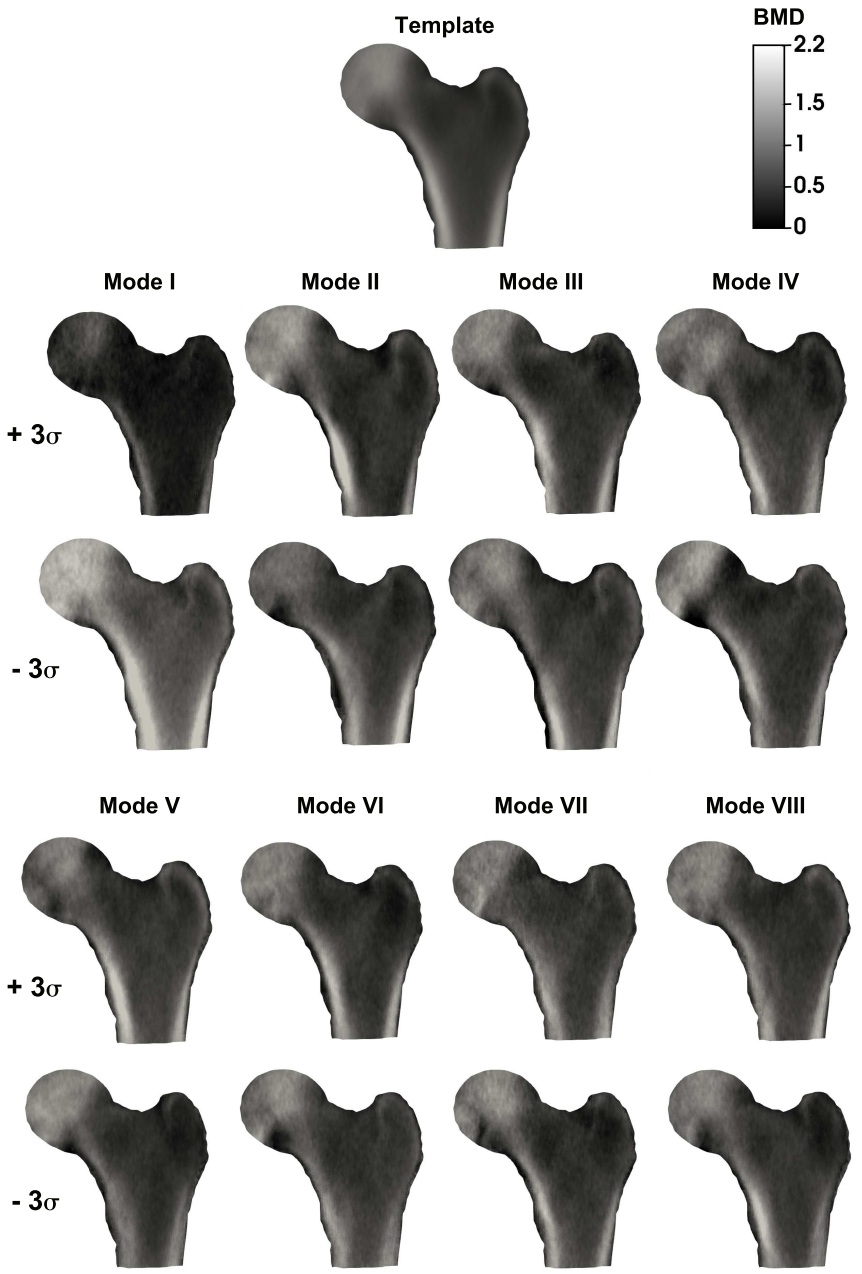

Figure 4.7: Visualization of the first 8 PCA modes of the BMD distribution. BMD is expressed in $\frac{g}{cm^2}$.

these two modes were both correlated with the HAL (mode 2: $R = 0.42$, $p = 0.032$; mode 2: $R = -0.61$, $p < 0.0001$). Following the performance of the correlation analysis between the PCA intensity and shape modes, it was also remarkable to find significant correlations between them (Table 4.2). Looking at the strongest, the II intensity mode tuned out to be correlated ($R = 0.63$) with the II shape mode, and the IV intensity mode with the first shape mode ($R = -0.60$).

Eventually, Figure 4.8 shows the combined Shape-Intensity Model (SIM)

Table 4.2: Correlation analysis between intensity and shape modes.

Intensity mode	**Shape mode**	p	R
I Mode	III mode	0.017	0.46
II Mode	I mode	0.034	-0.41
	II mode	0.0004	0.63
	III mode	0.036	-0.40
III Mode	I mode	0.009	0.49
	III mode	0.035	-0.41
VII Mode	VII mode	0.031	0.42

outputs. A total of 18 modes explained 95% of the combined intensity and shape variance, and the 6 modes displayed described 75% of it. Among them, only the second mode was significantly correlated to the RFI and FS. Analogously to the first mode of the intensity PCA, it was here the mode carrying the majority of the intensity-related information, strongly correlated to the T-score ($R = 0.9344$, $p < 0.0001$). Figure 4.9 shows the relation between the shape-intensity parameters (each patient-specific entry of $\boldsymbol{w}$ in Equation 4.10 and 4.11 for the mode 2) of the II mode with the RFI and FS.

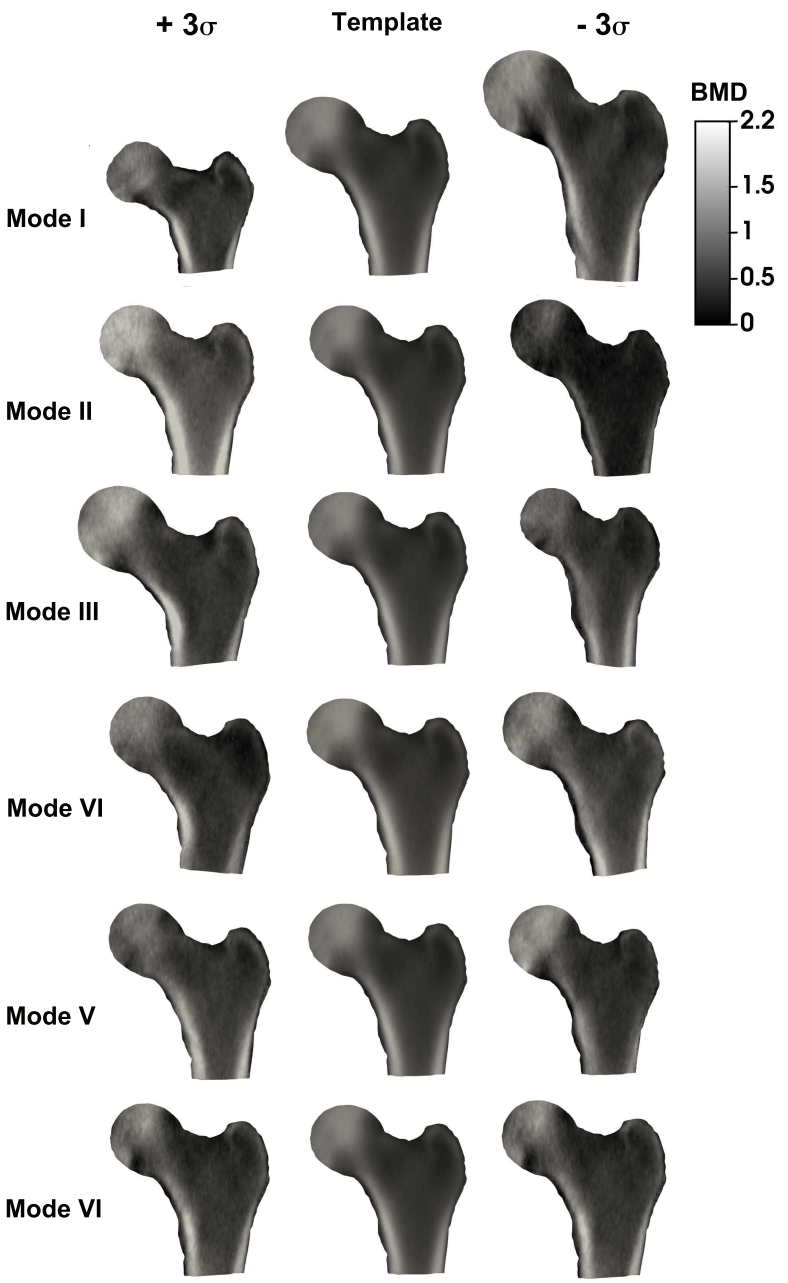

Figure 4.8: Visualization of the first 6 PCA combined shape-intensity modes. BMD is expressed in $\frac{g}{cm^2}$.

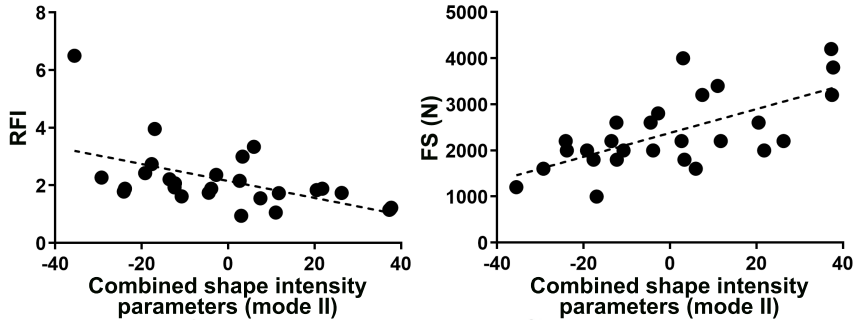

Figure 4.9: The RFI (left) and FS (right) compared to the patient-specific shape-intensity parameters associated to the second shape intensity combined PCA mode. RFI: $R^2 = 0.35$, $p = 0.001$; FS: $R^2 = 0.43$, $p = 0.0002$. The regression lines are displayed as well. Decreasing the weighting term of mode 2, the fracture risk increases: hence, the RFI boosts and the FS decreases.

4.3.2 PLS

With a deep interest in the features most meaningful with respect to the fracture risk in terms of both shape and intensity, PLS was performed ensuing PCA. As mentioned before, only the FS was considered, with the aim to identify those features strictly connected to the proximal femur resistance to loading.
A total of 11 PLS modes managed to explain at least 75% of the variance observed in the FS (Figure 4.10). In order to achieve 95% of the FS variability explained through shape-based modes, 15 modes were necessary (explaining 99.2% of the shape variance). Figure 4.11 presents the first

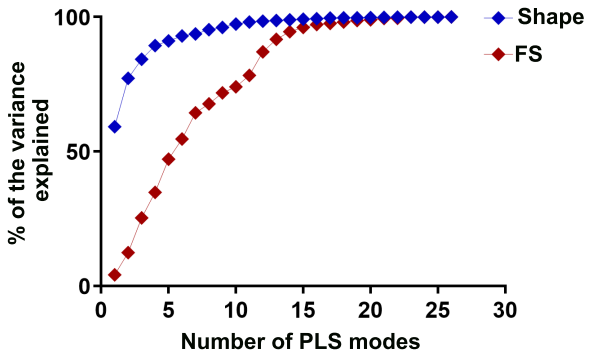

Figure 4.10: Cumulative percentage of variance explained by the PLS deformation modes. 11 modes described 98.16% of the shape and 78.27% of the FS variability.

6 modes. Although it is mode 1 which was found to include most of the shape variance, mode 3, which combines alterations in the intertrochanter and neck width, as well as in the length and inclination of the neck (HAL: $R = 0.48$, $p = 0.011$; NSA: $R = -0.56$, $p = 0.003$; narrow neck width: $R = 0.45$, $p = 0.02$; intetrochanter width: $R = 0.47$, $p = 0.01$), was the mode explaining the majority of the variability in the FS ($R = 0.36$, $p = 0.049$, Figure 4.14). Because in this case only one external variable was included within PLS, the PLS modes were automatically ordered with the requirement to have decreasing variance in the shape as well as decreasing

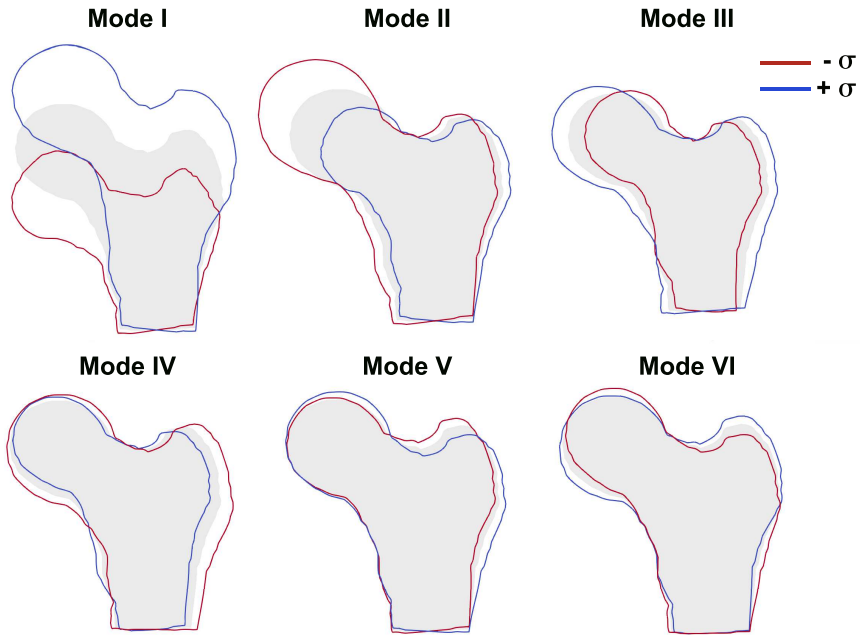

Figure 4.11: The first 6 PLS shape modes disclosing 93% of the shape and 54.6% of the FS variance. By construction, each mode moves towards $+\sigma$ when the FS increases. Hence, the $-\sigma$ deformation mode is here evidence of an increased risk of fracture.

covariance between shape and FS. The inconsistent decrease in the disclosed shape and FS variability by the PLS shape modes therefore appears to advocate a limited role of the femur shape in explaining the variations observed in the FS.

As far as the intensity-based PLS is concerned, in contrast to the previous one, 4 modes alone managed to describe 97.71% of the FS variability, but only 51.71% of the intensity variability. These 4 modes are also dis-

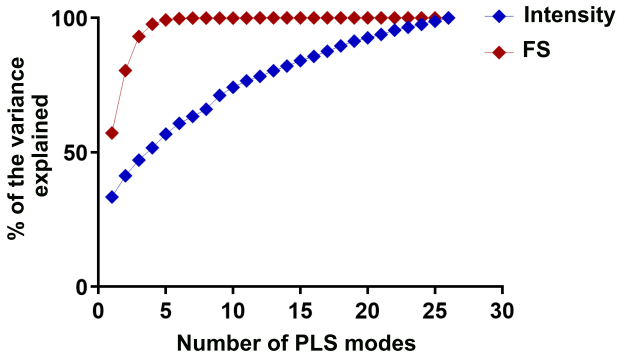

Figure 4.12: Cumulative percentage of variance disclosed by the PLS intensity modes. 4 modes managed to explain 97.71% of the FS variance while explaining 51.71% of the intensity variability.

played in Figure 4.13. Interestingly, the PLS main intensity modes turned out to be very similar to the corresponding PCA ones, stressing again, beyond the increased/decreased BMD as a whole, the variations at the intertrochanteric fossa and greater trochanter. In analogy with the previously obtained outcomes, the first mode was found strongly related to the BMD altogether and to the BMD distribution-based HSA parameters (e.g. T-score: $R = 0.95$; narrow neck BMD: $R = 0.93$; narrow neck buckling ratio: $R = -0.78$; intetrochanteric BMD: $R = 0.80$, $p < 0.0002$ for all); consequently, a strong relation was found with the FS as well ($R = 0.76$, $p < 0.0001$). Furthermore, the second mode resulted significantly correlated with the FS as well ($R = 0.48$, $p = 0.01$), while the

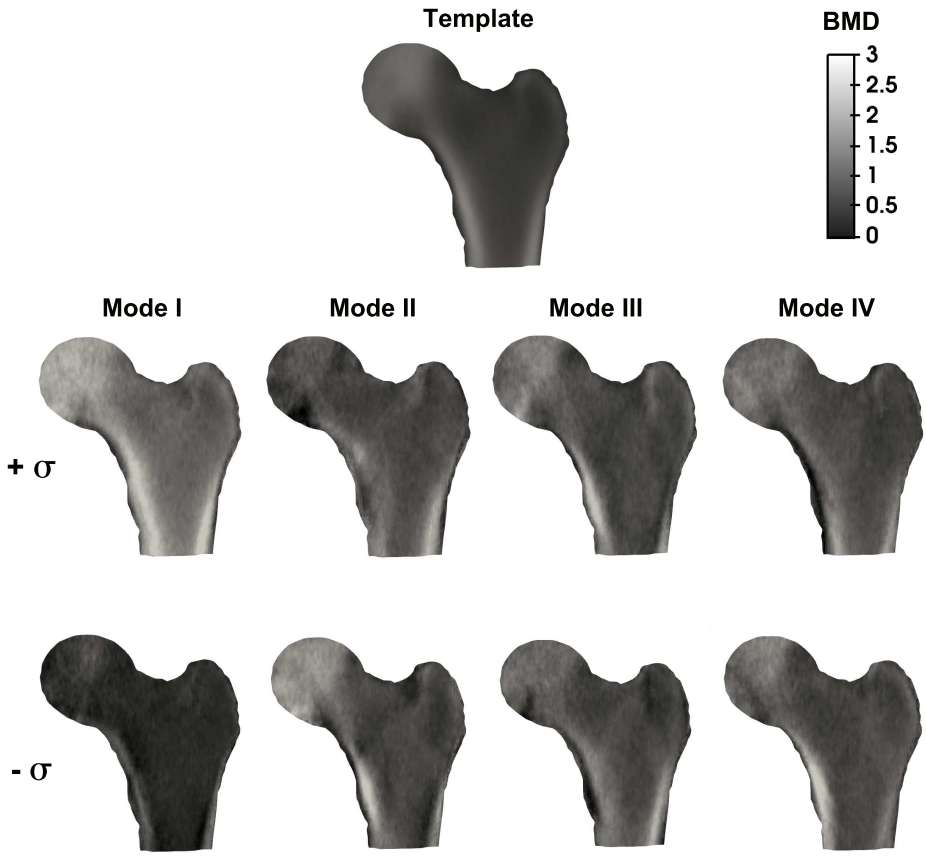

Figure 4.13: Visualization of the 4 PLS intensity modes. BMD is expressed in $\frac{g}{cm^2}$.

IV one was correlated to the HAL ($R = -0.46$, $p = 0.02$). Figure 4.14 compares the third PLS shape mode, i.e. the shape mode disclosing the highest percentage of the FS variability, and the first PLS intensity mode in terms of their relation with the FS itself.

Moreover, considering the presence of meaningful relations with the PLS

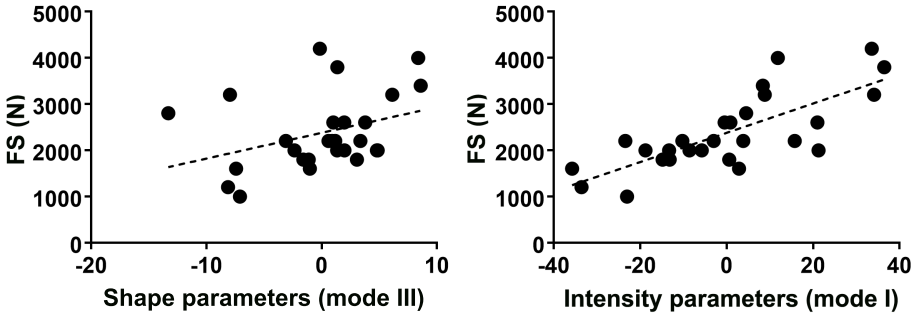

Figure 4.14: The third PLS shape parameters (left) and the first PLS intensity parameters (right) displayed with respect to the FS. Shape: $R^2 = 0.13$, $p = 0.049$; Intensity: $R^2 = 0.57$, $p < 0.0001$.

shape modes, Table 4.3 shows the statistically significant ones.

Table 4.3: Correlation analysis between PLS intensity and shape modes.

Intensity mode	Shape mode	p	R
II Mode	I mode	0.04	0.40
	IV mode	0.0037	0.54
III Mode	I mode	0.01	-0.47
	III mode	0.005	0.52
IV Mode	IV mode	0.009	0.50

Lastly, the PLS-based SSIM allowed to consider the shape-intensity unified modes most relevant to the FS. Three modes alone explained 96.72% of the FS variance and 56.75% of the combined intensity and shape variability. The first two, moreover, already achieved 83% of the variance

found in the FS. They are shown in Figure 4.15. The first two modes were

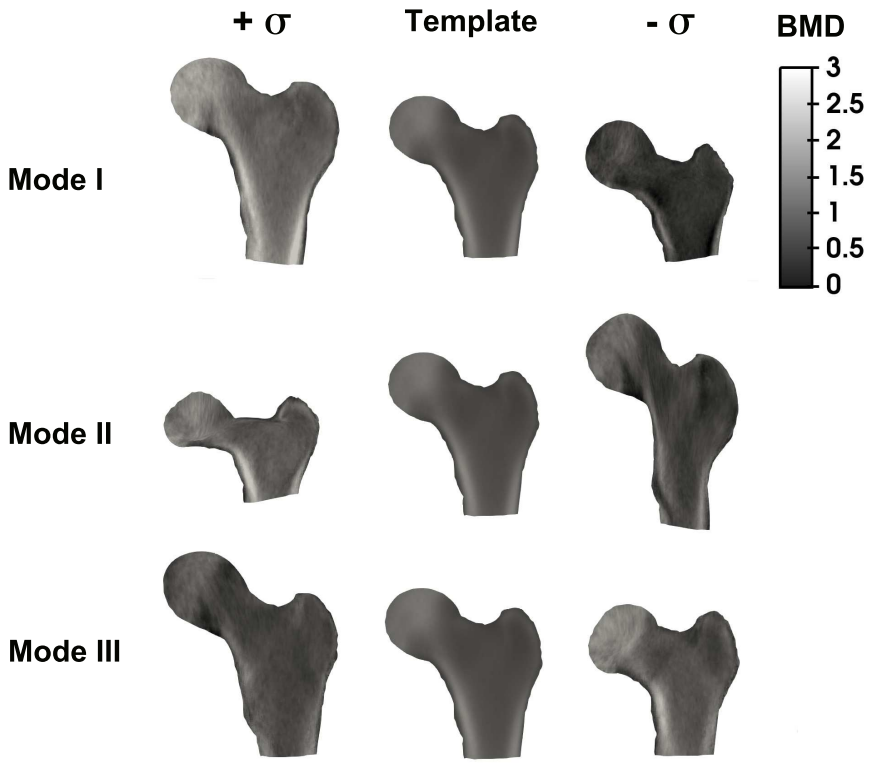

Figure 4.15: The first 3 combined shape intensity PLS modes. The $-\sigma$ direction, associated to a decreased strength, is that at higher risk. BMD is expressed in $\frac{g}{cm^2}$.

both significantly correlated to the FS (I mode: $R = 0.82$, $p < 0.0001$; II mode: $R = 0.40$, $p = 0.037$). From this perspective, the comparison between the patient-specific shape-intensity parameters related to the first mode and the FS itself is offered in Figure 4.16. In addition, Figure 4.17 offers the comparison between the T-score and the first PLS combined shape-intensity parameters. By projecting their patient-specific moment vectors and BMD values on the previously identified PLS combined space,

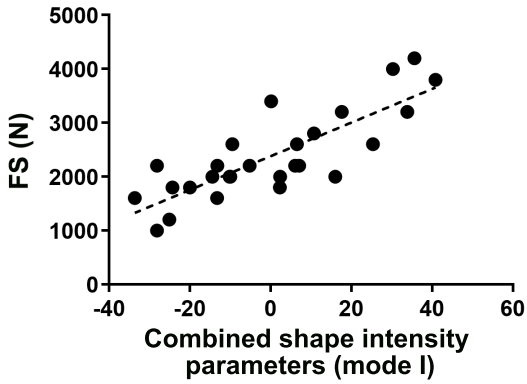

Figure 4.16: The first mode combined shape-intensity parameters and the FS. The regression lines are displayed as well ($R^2 = 0.67$, $p < 0.0001$). Decreasing the weighting term of mode 1 the fracture risk increases.

the shape-intensity parameters of the two fracture patients could be computed. As visible, there is a good stratification as far as the osteopenic patients are concerned; one of the two fractured patients (patient 29) in undoubtedly located in the highest risk region, the other, on the other hand, though not at the same degree, is still placed in the higher risk half. In addition to patient 29, also patients 1, 5, 10, 24, ostepenic, would be judged at an increased risk of fracture.

At last, CCA allowed to unify the modes which have been presented

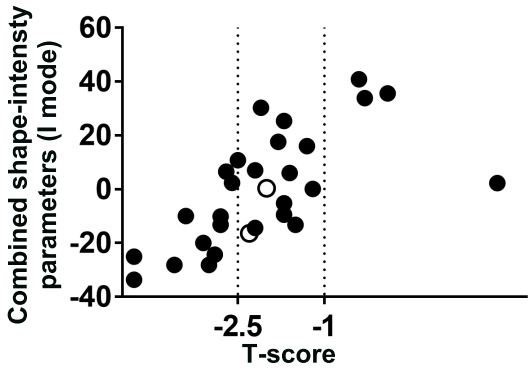

Figure 4.17: Comparison between the first combined shape-intensity PLS parameters and T-score classification performances. The two fractured patients, whose shape-intensity parameters have been determined *a posteriori* based on the previously determined PLS space, are represented with empty circles.

individually in Figure 4.15 and to predict new shape and intensity instances associated to a decreased or increased FS, shown in Figure 4.18. A more resistant proximal femur thus results characterized, as expected, by higher BMD values on the whole, with thicker and more defined cortex layers distally. It would then seem characterized by a markedly increased intertrochanteric width as well as by a less deep trochanteric fossa, yielding a wider neck cross-section. In addition, the neck inclination appears less pronounced.

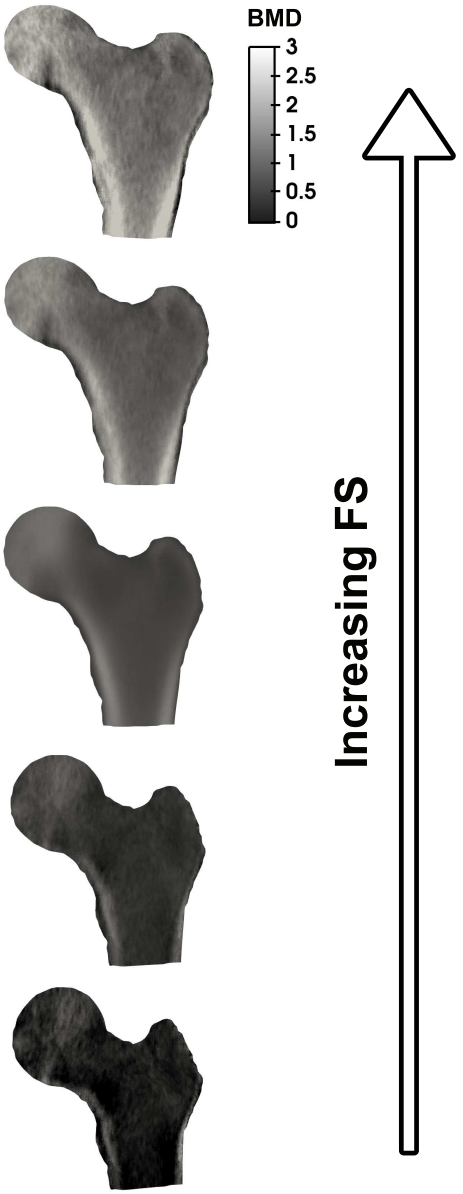

Figure 4.18: Shapes and intensities predicted by a decreased/increased FS with respect to its average value. In the CCA space, $R^2 = 0.96$, $p < 0.0001$. BMD is expressed in $\frac{g}{cm^2}$.

4.4 Discussion

In this chapter, the role of proximal femur geometry and BMD local distribution with respect to the previously estimated femoral strength has been explored through statistical shape and intensity modelling. In contrast to HSA parameters, which were employed in the previous chapters but represent discrete and highly correlated measures of geometry, SSM allowed indeed to capture all the global geometric variations in the population of input proximal femur shapes. Furthermore, the geometric and intensity features dependence, caused by the bone tissue adaptation process [147], prompted the need to account for them together.

In the first part of the study PCA was carried out. It yielded the most meaningful features both in terms of geometry and BMD distribution, and those disclosing most of the variability in the input population were considered. When accounting for the main anatomical features alone, only one among them was found to be significant to the RFI, while none of them was relevant to the FS. This is consistent with the fact that PCA, by definition, identifies features which are optimal for representing information, though not necessarily optimal for classification, and, at the same time, may hint that the most meaningful morphological features cannot explain, alone, the fracture risk level variability. From this perspective, when only the intensity distribution was considered, in order to assess how the BMD distribution mainly varied within the population, the first mode turned out be strongly correlated to both the FS and RFI, which might point out a much stronger link of the BMD distribution with the fracture risk variation, together with the fact that density might be able to explain the majority of the fracture risk variance. Moreover, the considerable number of PCA intensity modes necessary to disclose almost all of the intensity variability suggests more complex inter-subjects variability patterns in the BMD distribution compared to the morphological ones. Interestingly, noticeable correlation degrees were found between the II, III and IV main intensity modes and the first three shape modes (Table

4.2), witnessing a profound and complex interrelation existing between the shape and the density distribution in a living and continuously loaded tissue [147]. In this light, unifying the two in a combined SSIM, it was still the combined II mode, the most related to a thorough change in BMD -corroborated by its strong correlation with the T-score and BMD-, which explained most of the RFI and FS variability. The first combined mode, indeed, showed clearer alteration in the femur shape, while carrying much less BMD variation. It can also be appreciated, however, that in spite of its prevalent BMD role, the second shape-intensity PCA mode also encompassed changes in the femoral neck angle, width and length (Figure 4.8). Comparable results were shown in [132], accomplished developing statistical shape and intensity individual modes in a retrospective cohort.

The PLS, which was performed to overcome PCA limitations and therefore to draw attention to the main shape and intensity features most relevant to the FS, highlighted the inferiority of the shape modes to explain the FS variability: as visible in Figure 4.10, the first shape PLS mode, which alone was able to describe more the 50% of the total variance in the shape, covered, on the other hand, a very small percentage of the FS variability. Furthermore, to achieve a 50% explanation of the FS, 6 PLS modes were required, which were basically able to totally cover the shape variance. The third shape PLS mode was the one explaining the largest portion of the FS variance (13%), combining, from a morphological perspective, alterations in the neck inclination and length as well as in the intertrochanteric and shaft width mainly. A shorter HAL associated to an increased fracture risk might result odd and contrasting with the literature [51], although it is important to recall that each mode will contribute to the 'final' shape within a weighted linear combination, and that mode 2, undoubtedly showing HAL changes too, depicts an opposite trend. Focusing on the intensity PLS analysis, Figure 4.12 depicts a situation which appears reversed if compared to the shape PLS analysis: only few modes, although able to disclose only about 50% of the BMD distribution variability, managed to explain a considerable percentage of

the FS variability. This is evidence of the pivotal role which appears to be played by the material properties against the FS, which would then seem more decisive than that of shape. It is therefore not surprising that the main intensity PLS modes appear extremely similar to the PCA ones, given that the intensity variability in itself was already tightly related to that of the FS.

Besides, the combined PLS model, together with the subsequent associated CCA, yielded interesting result. First of all, as shown in Figure 4.17, the I PLS shape-intensity mode parameters allowed a good stratification of the patients within the three T-score categories (osteoporosis: T-score < -2.5; osteopenia: $-2.5 <$ T-score < -1; osteoporosis: T-score > -21). The two fracture patients, whose shape-intensity parameters were computed projecting their moment vectors and BMD array onto the PLS subspace identified previously with the 28 patients, were reasonably located in the higher risk half (lower half of the shape/intensity parameters values). Moreover, the osteopenic patients highlighted as being at higher risk did not contrast with those identified as so performing the CT- and DXA-based FE analyses. On top of that, the combination of shape and intensity did yield an improvement in the proportion of FS variance explained with respect to the intensity alone. Comparing Figures 4.16 and 4.14 indeed, the improved relation with the FS is visible: the first PLS intensity mode explained 57.18% of the FS variability, while the combined shape-intensity PLS mode achieved, merging shape and intensity, 66.9% of it. Therefore, although intensity appeared predominant in explaining most of the estimated femur strength and although it resulted correlated to the most meaningful shape features, the inclusion of the PLS deformation modes still led to an improvement.

Thanks to CCA, the three combined PLS modes depicted singularly in Figure 4.15 could be unified to predict shapes corresponding to a progressively increasing FS. As the strength increases, beyond the general BMD increase on the whole, with the thickening, especially medially, of the cortex layers, some changes in shape can be appreciated as well. The

proximal femur progressively increases its size, considerably widening the width at the intertrochanter. Besides, the neck-shaft angle decreases and the trochanteric fossa appears less hollow.

A number of limitations affected the here presented work, and are thus worth being stressed. First of all, the limited number of patients involved: dealing with the construction of statistical models, the outcomes would have undoubtedly benefited from a larger cohort, which might have also disclosed features here not accounted for. Moreover, the fact the PLS was carried out on an estimated variable needs to be mentioned. Nonetheless, in spite of the uncertainties it encloses, FS allowed to relatively estimate a patient-specific fracture risk level and thus to obtain, from a relative intra-cohort perspective, reasonable results. In addition, DXA images, on which the shape and intensity definitions were based, are known to be strongly affected by positioning inaccuracy and imprecision: if the patient's leg is not positioned correctly the DXA image might carry wrong information especially in terms of geometry. Ultimately, the intrinsic projective nature of DXA causes the head region, where the pelvis and femur bones overlap, to be erroneously characterized by a high density, which could have interfered with the statistical analyses. In this regard, aiming to assess the influence of the high BMD at the head, PCA and PLS were further performed excluding the BMD information at the head. As visible in Figures 4.19 and 4.20 (Appendix), the achieved outcomes do not highlight noticeable differences in the main densitometric features if compared to those considering the head density in the analyses. Although the density information at the head is not truly representative, this might not appear to negatively affect the obtained outcomes.

Despite the afore-mentioned limitations however, the herein presented approaches appeared to be extremely promising from the perspective of the current fracture risk assessment enhancement. Once, based on a training set, the PLS combined shape-intensity space is built determining its bases (i.e. the PLS modes) indeed, any new patient could be simply projected

on this space in order to assess the patient-specific shape-intensity parameter, gathering shape and BMD information together. This procedure would require information currently attainable: the proximal femur 2D profile extraction from DXA and the use of the pixel-by-pixel BMD map instead of the average BMD values used at present, which, however, is already computed by DXA scanners. Similarly, the possibility to build a dataset of shapes and corresponding BMD distributions associated to a progressively increasing risk of fracture might be attractive: given the patient-specific shape indeed and BMD distribution, they could be compared to the afore-mentioned instances collection to find the closest one and therefore to assess the patient-specific fracture risk. This of course would require, first of all, a training set much larger than that used here. In the end, larger cohorts and the availability of follow-up information would undoubtedly help to more deeply exploit the herein presented methods which, so far, have proved promising and attractive. Other studies, as mentioned previously, have explored the use of statistical shape and intensity models on retrospective cohorts DXA images, aiming to achieve an improved osteoporotic fracture risk prediction [123, 129, 132]. Nonetheless, PCA was generally adopted, and the interaction and inter-dependency between shape and density rarely investigated. Herein, due to the lack of follow-up information, an estimated patient-specific strength had to be considered; its relation with shape and intensity features was not only investigated through PCA, but also through PLS, which allowed to better focus on the features most meaningful to the fracture risk. In addition, the development of shape-intensity combined models allowed to consider the interplay between shape and BMD distribution.

Appendix

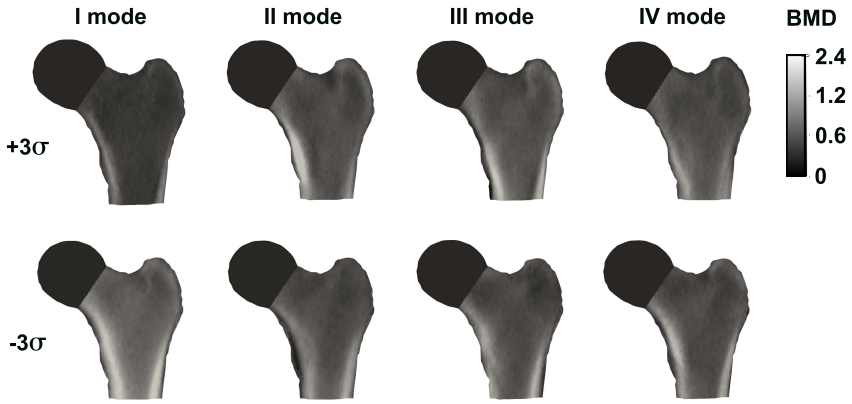

Figure 4.19: Visualization of the first 4 PCA intensity modes obtained neglecting BMD values in the head region. BMD is expressed in $\frac{g}{cm^2}$.

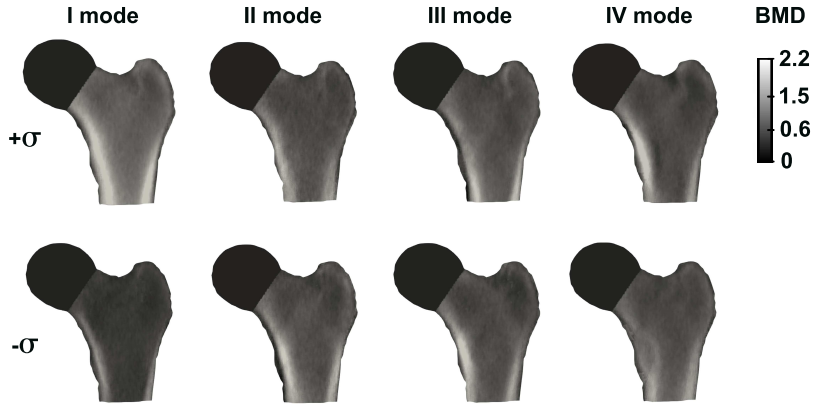

Figure 4.20: Visualization of the first 4 PLS intensity modes obtained neglecting BMD values in the head region. BMD is expressed in $\frac{g}{cm^2}$.

Chapter 5

Conclusions

In light of the T-score limited sensitivity in drawing attention to patients who actually are at considerable risk of fracture, this thesis was mainly focused on investigating how the current osteoporotic fracture risk assessment could be enhanced. It represented an exploratory study, since the lack of follow-up information prevented the validation of the obtained outcomes. Therefore, the ambition was not to assess the absolute fracture risk level of the included patients, rather to identify, from a relative perspective, additional features leading to an enhanced fracture risk estimation. Particular attention was paid to data being already clinically available though without any practical application. From this perspective, the aim was indeed to detect clinically attainable improvements, able to be integrated in the current diagnostic process.

Although the attention was directed towards HSA variables at first, widely considered in literature, it was not found straightforward to assess if the information they carry is primarily morphological or predominantly associated to the mineral mass distribution contained in the DXA image. The HSA Buckling Ratio and Cross-Sectional Moment of Inertia, found relevant with respect to the fracture risk indices (RFI and FS) in both the CT- and DXA-based cases, enclose indeed geometric information, being

deeply related to the bone mass as well. Only the neck-shaft angle, which was also found to be meaningful, is not strictly related to the mineral mass. In this context, statistical shape and intensity analysis allowed to shed light on the synergic contribution of the shape and BMD distribution as fracture risk determinants. BMD appeared to be able to explain most of the variation found in the three-dimensional FS, while the main shape features appeared to play a more marginal role, not clearly related to it. The addition of the shape features to the intensity ones, however, did improve the percentage of the FS variance explained. The main shape and BMD distribution features were also interestingly found to be correlated to one another, thus suggesting a reciprocal influence. Therefore, the analysis of the shape or intensity features taken independently would not seem optimal. It is still worth stressing that the main geometrical and intensity features were here assessed with respect to a femoral strength determined on the basis of three-dimensional FE analyses. Nevertheless, although based on a relative perspective, the here adopted methods suggested further investigation of the prevailing role of BMD distribution, considering that the pixel-by-pixel BMD map is currently provided by DXA scans. As a whole, focusing on the combination of the main shape and intensity features most related to the estimated strength with approaches, such the PLS, rarely adopted within this field, these methods also appeared promising with a view to better interpret the main fracture determinants.

References

[1] Christopher M Bono and Thomas A Einhorn. "Overview of osteoporosis: pathophysiology and determinants of bone strength". In: *The aging spine*. Springer, 2005, pp. 8–14.

[2] Fuller Albright, Patricia H Smith, and Anna M Richardson. "Postmenopausal osteoporosis: its clinical features". In: *Journal of the American Medical Association* 116.22 (1941), pp. 2465–2474.

[3] World Health Organization et al. "Assessment of fracture risk and its application to screening for postmenopausal osteoporosis: report of a WHO study group [meeting held in Rome from 22 to 25 June 1992]". In: (1994).

[4] Julie T Lin and Joseph M Lane. "Osteoporosis: a review". In: *Clinical Orthopaedics and Related Research®* 425 (2004), pp. 126–134.

[5] M Lunt, Dieter Felsenberg, J Adams, Lidia Benevolenskaya, J Cannata, J Dequeker, C Dodenhof, JA Falch, Olof Johnell, Kay-Tee Khaw, et al. "Population-based geographic variations in DXA bone density in Europe: the EVOS study". In: *Osteoporosis international* 7.3 (1997), pp. 175–189.

[6] Cyrus Cooper. "Epidemiology and public health impact of osteoporosis". In: *Baillière's clinical rheumatology* 7.3 (1993), pp. 459–477.

[7] O Ström, F Borgström, John A Kanis, Juliet Compston, Cyrus Cooper, Eugene V McCloskey, and Bengt Jönsson. "Osteoporosis: burden, health care provision and opportunities in the EU". In: *Archives of osteoporosis* 6.1-2 (2011), pp. 59–155.

[8] RP Heaney. "Pathophysiology of osteoporosis: Implications for treatment." In: *Texas medicine* 70.12 (1974), p. 37.

[9] Emma Hernlund, A Svedbom, M Ivergård, J Compston, Cyrus Cooper, J Stenmark, Eugene V McCloskey, Bengt Jönsson, and John A Kanis. "Osteoporosis in the European Union: medical management, epidemiology and economic burden". In: *Archives of osteoporosis* 8.1-2 (2013), p. 136.

[10] M Rossini, S Adami, F Bertoldo, D Diacinti, D Gatti, S Giannini, A Giusti, N Malavolta, S Minisola, G Osella, et al. "Guidelines for the diagnosis, prevention and management of osteoporosis". In: *Reumatismo* (2016), pp. 1–39.

[11] JA Kanis, Olof Johnell, A Oden, Ingemar Sernbo, Inga Redlund-Johnell, A Dawson, C De Laet, and B Jonsson. "Long-term risk of osteoporotic fracture in Malmö". In: *Osteoporosis international* 11.8 (2000), pp. 669–674.

[12] John A Kanis, Eugene V McCloskey, Helena Johansson, and Anders Oden. "Approaches to the targeting of treatment for osteoporosis". In: *Nature Reviews Rheumatology* 5.8 (2009), p. 425.

[13] JA Kanis, C Cooper, René Rizzoli, J-Y Reginster, et al. "European guidance for the diagnosis and management of osteoporosis in postmenopausal women". In: *Osteoporosis International* 30.1 (2019), pp. 3–44.

[14] Olof Johnell and JA Kanis. "An estimate of the worldwide prevalence and disability associated with osteoporotic fractures". In: *Osteoporosis international* 17.12 (2006), pp. 1726–1733.

[15] LJ Melton Iii, Terry M Therneau, and DR Larson. "Long-term trends in hip fracture prevalence: the influence of hip fracture incidence and survival". In: *Osteoporosis International* 8.1 (1998), pp. 68–74.

[16] JJW Roche, Russell T Wenn, Opinder Sahota, and Christopher G Moran. "Effect of comorbidities and postoperative complications on mortality after hip fracture in elderly people: prospective observational cohort study". In: *Bmj* 331.7529 (2005), p. 1374.

[17] Nicholas Harvey, Elaine Dennison, and Cyrus Cooper. "Osteoporosis: impact on health and economics". In: *Nature Reviews Rheumatology* 6.2 (2010), p. 99.

[18] Sydney Lou Bonnick. "Hsa: Beyond bmd with dxa". In: *Bone* 41.1 (2007), S9–S12.

[19] Cyrus Cooper, Stephen H Gehlbach, and Robert Lindsay. *Prevention and Treatment of Osteoporosis in the High-Risk Patient: A Clinician's Guide*. CRC Press, 2005.

[20] Thomas Beck. "Measuring the structural strength of bones with dual-energy X-ray absorptiometry: principles, technical limitations, and future possibilities". In: *Osteoporosis International* 14.5 (2003), pp. 81–88.

[21] RM Lorente Ramos, J Azpeitia Armán, N Arévalo Galeano, A Munoz Hernández, JM García Gómez, and J Gredilla Molinero. "Dual energy X-ray absorptimetry: fundamentals, methodology, and clinical applications". In: *Radiología (English Edition)* 54.5 (2012), pp. 410–423.

[22] Deborah Marshall, Olof Johnell, and Hans Wedel. "Meta-analysis of how well measures of bone mineral density predict occurrence of osteoporotic fractures". In: *Bmj* 312.7041 (1996), pp. 1254–1259.

[23] JA Kanis, Olof Johnell, Anders Odén, Helena Johansson, and EFRAX McCloskey. "FRAX and the assessment of fracture probability in men and women from the UK". In: *Osteoporosis international* 19.4 (2008), pp. 385–397.

[24] Sanford Baim and William D Leslie. "Assessment of fracture risk". In: *Current osteoporosis reports* 10.1 (2012), pp. 28–41.

[25] Ethel S Siris, Steven T Harris, Richard Eastell, Jose R Zanchetta, Stefan Goemaere, Adolfo Diez-Perez, John L Stock, Jingli Song, Yongming Qu, Pandurang M Kulkarni, et al. "Skeletal effects of raloxifene after 8 years: results from the continuing outcomes relevant to Evista (CORE) study". In: *Journal of Bone and Mineral Research* 20.9 (2005), pp. 1514–1524.

[26] Pierre D Delmas and Ego Seeman. "Changes in bone mineral density explain little of the reduction in vertebral or nonvertebral fracture risk with anti-resorptive therapy". In: *Bone* 34.4 (2004), pp. 599–604.

[27] Nelson B Watts, Piet Geusens, Ian P Barton, and Dieter Felsenberg. "Relationship between changes in BMD and nonvertebral fracture incidence associated with risedronate: reduction in risk of nonvertebral fracture is not related to change in BMD". In: *Journal of Bone and Mineral Research* 20.12 (2005), pp. 2097–2104.

[28] Marco Viceconti, Muhammad Qasim, Pinaki Bhattacharya, and Xinshan Li. "Are CT-based finite element model predictions of femoral bone strengthening clinically useful?" In: *Current osteoporosis reports* 16.3 (2018), pp. 216–223.

[29] M Di Stefano, Giovanni Carlo Isaia, D Cussa, and Gian Luigi Panattoni. "Preliminary result on trabecular bone score (TBS) in lumbar vertebrae with experimentally altered microarchitecture". In: *Journal of Biological Research-Bollettino della Società Italiana di Biologia Sperimentale* 86.1 (2013).

[30] Stephen Kaptoge, Thomas J Beck, Jonathan Reeve, Katie L Stone, Teresa A Hillier, Jane A Cauley, and Steven R Cummings. "Prediction of incident hip fracture risk by femur geometry variables measured by hip structural analysis in the study of osteoporotic fractures". In: *Journal of Bone and Mineral Research* 23.12 (2008), pp. 1892–1904.

[31] Benjamin CC Khoo, Joshua R Lewis, K Brown, and Richard L Prince. "Evaluation of a simplified hip structure analysis method for the prediction of incident hip fracture events". In: *Osteoporosis International* 27.1 (2016), pp. 241–248.

[32] Andrea Z LaCroix, Thomas J Beck, Jane A Cauley, Cora E Lewis, Tamsen Bassford, Rebecca Jackson, Guanglin Wu, and Zhao Chen. "Hip structural geometry and incidence of hip fracture in postmenopausal women: what does it add to conventional bone mineral density?" In: *Osteoporosis International* 21.6 (2010), pp. 919–929.

[33] Fernando Rivadeneira, M Carola Zillikens, Chris EDH De Laet, Albert Hofman, André G Uitterlinden, Thomas J Beck, and Huibert AP Pols. "Femoral neck BMD is a strong predictor of hip fracture susceptibility in elderly men and women because it detects cortical bone instability: the Rotterdam Study". In: *Journal of Bone and Mineral Research* 22.11 (2007), pp. 1781–1790.

[34] P Szulc, F Duboeuf, AM Schott, P Dargent-Molina, PJ Meunier, and PD Delmas. "Structural determinants of hip fracture in elderly women: re-analysis of the data from the EPIDOS study". In: *Osteoporosis international* 17.2 (2006), pp. 231–236.

[35] S Gnudi, C Ripamonti, G Gualtieri, and N Malavolta. "Geometry of proximal femur in the prediction of hip fracture in osteoporotic women." In: *The British journal of radiology* 72.860 (1999), pp. 729–733.

[36] Joyce H Keyak, Stephen A Rossi, Kimberly A Jones, and Harry B Skinner. "Prediction of femoral fracture load using automated finite element modeling". In: *Journal of biomechanics* 31.2 (1997), pp. 125–133.

[37] Dianna D Cody, Gary J Gross, Fu J Hou, Horace J Spencer, Steven A Goldstein, and David P Fyhrie. "Femoral strength is better predicted by finite element models than QCT and DXA". In: *Journal of biomechanics* 32.10 (1999), pp. 1013–1020.

[38] E DallAra, D Pahr, P Varga, F Kainberger, and P Zysset. "QCT-based finite element models predict human vertebral strength in vitro significantly better than simulated DEXA". In: *Osteoporosis International* 23.2 (2012), pp. 563–572.

[39] Dan Dragomir-Daescu, Christina Salas, Susheil Uthamaraj, and Timothy Rossman. "Quantitative computed tomography-based finite element analysis predictions of femoral strength and stiffness depend on computed tomography settings". In: *Journal of biomechanics* 48.1 (2015), pp. 153–161.

[40] Zainab Altai, Muhammad Qasim, Xinshan Li, and Marco Viceconti. "The effect of boundary and loading conditions on patient classification using finite element predicted risk of fracture". In: *Clinical Biomechanics* (2019).

[41] Philippe K Zysset, Enrico Dall'Ara, Peter Varga, and Dieter H Pahr. "Finite element analysis for prediction of bone strength". In: *BoneKEy reports* 2 (2013).

[42] PK Basu, AG Beall, DJ Simmons, and M Vannier. "3-D femoral stress analysis using CT scans and p-version FEM". In: *Biomaterials, medical devices, and artificial organs* 13.3-4 (1985), pp. 163–186.

[43] Patrick Haentjens, Philippe Autier, Martine Barette, and Steven Boonen. “The economic cost of hip fractures among elderly women: a one-year, prospective, observational cohort study with matched-pair analysis”. In: *JBJS* 83.4 (2001), p. 493.

[44] Jacqueline R Center, Tuan V Nguyen, Diane Schneider, Philip N Sambrook, and John A Eisman. “Mortality after all major types of osteoporotic fracture in men and women: an observational study”. In: *The Lancet* 353.9156 (1999), pp. 878–882.

[45] Jari Parkkari, Pekka Kannus, Mika Palvanen, A Natri, J Vainio, H Aho, I Vuori, and M Järvinen. “Majority of hip fractures occur as a result of a fall and impact on the greater trochanter of the femur: a prospective controlled hip fracture study with 206 consecutive patients”. In: *Calcified tissue international* 65.3 (1999), pp. 183–187.

[46] Teppo LN Järvinen, Harri Sievänen, Karim M Khan, Ari Heinonen, and Pekka Kannus. “Shifting the focus in fracture prevention from osteoporosis to falls”. In: *Bmj* 336.7636 (2008), pp. 124–126.

[47] Robert G Cumming and Robin J Klineberg. “Fall frequency and characteristics and the risk of hip fractures”. In: *Journal of the American Geriatrics Society* 42.7 (1994), pp. 774–778.

[48] Peter M de Bakker, Sarah L Manske, Vincent Ebacher, Thomas R Oxland, Peter A Cripton, and Pierre Guy. “During sideways falls proximal femur fractures initiate in the superolateral cortex: evidence from high-speed video of simulated fractures”. In: *Journal of biomechanics* 42.12 (2009), pp. 1917–1925.

[49] Piet Geusens, Tineke van Geel, and Joop van den Bergh. “Can hip fracture prediction in women be estimated beyond bone mineral density measurement alone?” In: *Therapeutic advances in musculoskeletal disease* 2.2 (2010), pp. 63–77.

[50] Stacey A Wainwright, Lynn M Marshall, Kristine E Ensrud, Jane A Cauley, Dennis M Black, Teresa A Hillier, Marc C Hochberg, Molly T Vogt, Eric S Orwoll, and Study of Osteoporotic Fractures Research Group. "Hip fracture in women without osteoporosis". In: *The Journal of Clinical Endocrinology & Metabolism* 90.5 (2005), pp. 2787–2793.

[51] Jennifer S Gregory and Richard M Aspden. "Femoral geometry as a risk factor for osteoporotic hip fracture in men and women". In: *Medical engineering & physics* 30.10 (2008), pp. 1275–1286.

[52] S Gnudi, E Sitta, and E Pignotti. "Prediction of incident hip fracture by femoral neck bone mineral density and neck–shaft angle: a 5-year longitudinal study in post-menopausal females". In: *The British journal of radiology* 85.1016 (2012), e467–e473.

[53] TJ Beck. "Hip structural analysis (HSA) program (BMD and structural geometry methodology) as used to create NHANES III dataset". In: *Baltimore, MD: Johns Hopkins University, School of Medicine* 11 (2002).

[54] R Bruce Martin and David B Burr. "Non-invasive measurement of long bone cross-sectional moment of inertia by photon absorptiometry". In: *Journal of biomechanics* 17.3 (1984), pp. 195–201.

[55] Philippe Zysset, Ling Qin, Thomas Lang, Sundeep Khosla, William D Leslie, John A Shepherd, John T Schousboe, and Klaus Engelke. "Clinical use of quantitative computed tomography–based finite element analysis of the hip and spine in the management of osteoporosis in adults: the 2015 ISCD official positionspart II". In: *Journal of clinical densitometry* 18.3 (2015), pp. 359–392.

[56] Steven R Cummings and L Joseph Melton. "Epidemiology and outcomes of osteoporotic fractures". In: *The Lancet* 359.9319 (2002), pp. 1761–1767.

[57] Masahiko Bessho, Isao Ohnishi, Juntaro Matsuyama, Takuya Matsumoto, Kazuhiro Imai, and Kozo Nakamura. "Prediction of strength and strain of the proximal femur by a CT-based finite element method". In: *Journal of biomechanics* 40.8 (2007), pp. 1745–1753.

[58] L Duchemin, D Mitton, E Jolivet, V Bousson, JD Laredo, and W Skalli. "An anatomical subject-specific FE-model for hip fracture load prediction". In: *Computer methods in biomechanics and biomedical engineering* 11.2 (2008), pp. 105–111.

[59] Joyce H Keyak, Tadashi S Kaneko, Jamshid Tehranzadeh, and Harry B Skinner. "Predicting proximal femoral strength using structural engineering models". In: *Clinical Orthopaedics and Related Research®* 437 (2005), pp. 219–228.

[60] Enrico Schileo, Luca Balistreri, Lorenzo Grassi, Luca Cristofolini, and Fulvia Taddei. "To what extent can linear finite element models of human femora predict failure under stance and fall loading configurations?" In: *Journal of biomechanics* 47.14 (2014), pp. 3531–3538.

[61] Dan Dragomir-Daescu, Jorn Op Den Buijs, Sean McEligot, Yifei Dai, Rachel C Entwistle, Christina Salas, L Joseph Melton, Kevin E Bennet, Sundeep Khosla, and Shreyasee Amin. "Robust QCT/FEA models of proximal femur stiffness and fracture load during a sideways fall on the hip". In: *Annals of biomedical engineering* 39.2 (2011), pp. 742–755.

[62] Janne EM Koivumäki, Jérôme Thevenot, Pasi Pulkkinen, Volker Kuhn, Thomas M Link, Felix Eckstein, and Timo Jämsä. "Cortical bone finite element models in the estimation of experimentally measured failure loads in the proximal femur". In: *Bone* 51.4 (2012), pp. 737–740.

[63] Lorenzo Grassi, Enrico Schileo, Fulvia Taddei, Lorenzo Zani, Mateusz Juszczyk, Luca Cristofolini, and Marco Viceconti. "Accuracy

of finite element predictions in sideways load configurations for the proximal human femur". In: *Journal of biomechanics* 45.2 (2012), pp. 394–399.

[64] Sven van den Munckhof and Amir Abbas Zadpoor. "How accurately can we predict the fracture load of the proximal femur using finite element models?" In: *Clinical Biomechanics* 29.4 (2014), pp. 373–380.

[65] Felix Eckstein, Caecilia Wunderer, Holger Boehm, Volker Kuhn, Mathias Priemel, Thomas M Link, and Eva-Maria Lochmüller. "Reproducibility and side differences of mechanical tests for determining the structural strength of the proximal femur". In: *Journal of Bone and Mineral Research* 19.3 (2004), pp. 379–385.

[66] AC Courtney, EF Wachtel, ER Myers, and WC Hayes. "Effects of loading rate on strength of the proximal femur". In: *Calcified tissue international* 55.1 (1994), pp. 53–58.

[67] Kyle K Nishiyama, Seth Gilchrist, Pierre Guy, Peter Cripton, and Steven K Boyd. "Proximal femur bone strength estimated by a computationally fast finite element analysis in a sideways fall configuration". In: *Journal of biomechanics* 46.7 (2013), pp. 1231–1236.

[68] Azhar A Ali, Luca Cristofolini, Enrico Schileo, Haixiang Hu, Fulvia Taddei, Raymond H Kim, Paul J Rullkoetter, and Peter J Laz. "Specimen-specific modeling of hip fracture pattern and repair". In: *Journal of Biomechanics* 47.2 (2014), pp. 536–543.

[69] Enrico Schileo, Fulvia Taddei, Andrea Malandrino, Luca Cristofolini, and Marco Viceconti. "Subject-specific finite element models can accurately predict strain levels in long bones". In: *Journal of biomechanics* 40.13 (2007), pp. 2982–2989.

[70] Mateusz Maria Juszczyk, Luca Cristofolini, and Marco Viceconti. "The human proximal femur behaves linearly elastic up to failure

under physiological loading conditions". In: *Journal of biomechanics* 44.12 (2011), pp. 2259–2266.

[71] Elise F Morgan, Harun H Bayraktar, and Tony M Keaveny. "Trabecular bone modulus–density relationships depend on anatomic site". In: *Journal of biomechanics* 36.7 (2003), pp. 897–904.

[72] Mohamad Ridzwan. "A computational orthopaedic biomechanics study of osteoporotic hip fractures". PhD thesis. Imperial College London, 2016.

[73] Mohamad Ikhwan Zaini Ridzwan, Chamaiporn Sukjamsri, Bidyut Pal, Richard J van Arkel, Andrew Bell, Monica Khanna, Aroon Baskaradas, Richard Abel, Oliver Boughton, Justin Cobb, et al. "Femoral fracture type can be predicted from femoral structure: A finite element study validated by digital volume correlation experiments". In: *Journal of Orthopaedic Research®* 36.3 (2018), pp. 993–1001.

[74] Catherine M Ford, Tony M Keaveny, and Wilson C Hayes. "The effect of impact direction on the structural capacity of the proximal femur during falls". In: *Journal of Bone and Mineral Research* 11.3 (1996), pp. 377–383.

[75] Enrico Schileo, Enrico DallAra, Fulvia Taddei, Andrea Malandrino, Tom Schotkamp, Massimiliano Baleani, and Marco Viceconti. "An accurate estimation of bone density improves the accuracy of subject-specific finite element models". In: *Journal of biomechanics* 41.11 (2008), pp. 2483–2491.

[76] Masahiko Bessho, Isao Ohnishi, Takuya Matsumoto, Satoru Ohashi, Juntaro Matsuyama, Kenji Tobita, Masako Kaneko, and Kozo Nakamura. "Prediction of proximal femur strength using a CT-based nonlinear finite element method: differences in predicted fracture load and site with changing load and boundary conditions". In: *Bone* 45.2 (2009), pp. 226–231.

[77] CG Armstrong, AS Bahrani, and DL Gardner. “In vitro measurement of articular cartilage deformations in the intact human hip joint under load.” In: *JBJS* 61.5 (1979), pp. 744–755.

[78] HL Fermor, SWD McLure, SD Taylor, SL Russell, S Williams, J Fisher, and E Ingham. “Biological, biochemical and biomechanical characterisation of articular cartilage from the porcine, bovine and ovine hip and knee”. In: *Bio-medical materials and engineering* 25.4 (2015), pp. 381–395.

[79] Alessandra Aldieri, Mara Terzini, Giangiacomo Osella, Adriano M Priola, Alberto Angeli, Andrea Veltri, Alberto L Audenino, and Cristina Bignardi. “Osteoporotic hip fracture prediction: is t-score-based criterion enough? A hip structural analysis-based model”. In: *Journal of biomechanical engineering* 140.11 (2018), p. 111004.

[80] M Qasim, G Farinella, Ju Zhang, X Li, L Yang, R Eastell, and Marco Viceconti. “Patient-specific finite element estimated femur strength as a predictor of the risk of hip fracture: the effect of methodological determinants”. In: *Osteoporosis International* 27.9 (2016), pp. 2815–2822.

[81] He Gong, Ming Zhang, Yubo Fan, Wai Leung Kwok, and Ping Chung Leung. “Relationships between femoral strength evaluated by nonlinear finite element analysis and BMD, material distribution and geometric morphology”. In: *Annals of biomedical engineering* 40.7 (2012), pp. 1575–1585.

[82] Harun H Bayraktar, Elise F Morgan, Glen L Niebur, Grayson E Morris, Eric K Wong, and Tony M Keaveny. “Comparison of the elastic and yield properties of human femoral trabecular and cortical bone tissue”. In: *Journal of biomechanics* 37.1 (2004), pp. 27–35.

[83] Masoud Nasiri Sarvi and Yunhua Luo. “A two-level subject-specific biomechanical model for improving prediction of hip fracture risk”. In: *Clinical biomechanics* 30.8 (2015), pp. 881–887.

[84] Stephen N Robinovitch, Thomas A McMahon, and Wilson C Hayes. “Force attenuation in trochanteric soft tissues during impact from a fall”. In: *Journal of Orthopaedic Research* 13.6 (1995), pp. 956–962.

[85] Andrew C Laing and Stephen N Robinovitch. “The force attenuation provided by hip protectors depends on impact velocity, pelvic size, and soft tissue stiffness”. In: *Journal of biomechanical engineering* 130.6 (2008), p. 061005.

[86] M Nasiri Sarvi, Yunhua Luo, Peidong Sun, and Jun Ouyang. “Experimental validation of subject-specific dynamics model for predicting impact force in sideways fall”. In: *Journal of Biomedical Science and Engineering* 7.07 (2014), pp. 405–18.

[87] Stephen N Robinovitch, Wilson C Hayes, and Thomas A McMahon. “Distribution of contact force during impact to the hip”. In: *Annals of biomedical engineering* 25.3 (1997), pp. 499–508.

[88] AJ Van den Kroonenberg, Wilson C Hayes, and TA McMahon. “Dynamic models for sideways falls from standing height”. In: *Journal of biomechanical engineering* 117.3 (1995), pp. 309–318.

[89] Cristina Falcinelli, Enrico Schileo, Luca Balistreri, Fabio Baruffaldi, Barbara Bordini, Marco Viceconti, Ugo Albisinni, Francesco Ceccarelli, Luigi Milandri, Aldo Toni, et al. “Multiple loading conditions analysis can improve the association between finite element bone strength estimates and proximal femur fractures: a preliminary study in elderly women”. In: *Bone* 67 (2014), pp. 71–80.

[90] Thomas J Beck, Chrisopher B Ruff, Karen E Warden, Jr WW Scott, and Gopala U Rao. “Predicting femoral neck strength from

bone mineral data. A structural approach." In: *Investigative radiology* 25.1 (1990), pp. 6–18.

[91] Mary L Bouxsein. "Technology insight: noninvasive assessment of bone strength in osteoporosis". In: *Nature Reviews Rheumatology* 4.6 (2008), p. 310.

[92] Esteban Walker. "Detection of collinearity-influential observations". In: *Communications in Statistics-Theory and Methods* 18.5 (1989), pp. 1675–1690.

[93] Hirotugu Akaike. "A new look at the statistical model identification". In: *Selected Papers of Hirotugu Akaike*. Springer, 1974, pp. 215–222.

[94] SCE Schuit, M Van der Klift, AEAM Weel, CEDH De Laet, H Burger, E Seeman, A Hofman, AG Uitterlinden, JPTM Van Leeuwen, and HAP Pols. "Fracture incidence and association with bone mineral density in elderly men and women: the Rotterdam Study". In: *Bone* 34.1 (2004), pp. 195–202.

[95] John A Kanis, Frederik Borgstrom, Chris De Laet, Helena Johansson, Olof Johnell, Bengt Jonsson, Anders Oden, Niklas Zethraeus, Bruce Pfleger, and Nikolai Khaltaev. "Assessment of fracture risk". In: *Osteoporosis international* 16.6 (2005), pp. 581–589.

[96] Lisa Langsetmo, David Goltzman, Christopher S Kovacs, Jonathan D Adachi, David A Hanley, Nancy Kreiger, Robert Josse, Alexandra Papaioannou, Wojciech P Olszynski, and Sophie A Jamal. "Repeat low-trauma fractures occur frequently among men and women who have osteopenic BMD". In: *Journal of Bone and Mineral Research* 24.9 (2009), pp. 1515–1522.

[97] Thomas J Beck, Katie L Stone, Tammy L Oreskovic, Marc C Hochberg, Michael C Nevitt, Harry K Genant, and Steven R Cummings. "Effects of current and discontinued estrogen replacement

therapy on hip structural geometry: the study of osteoporotic fractures". In: *Journal of Bone and Mineral Research* 16.11 (2001), pp. 2103–2110.

[98] Thomas J Beck. "Extending DXA beyond bone mineral density: understanding hip structure analysis". In: *Current osteoporosis reports* 5.2 (2007), pp. 49–55.

[99] HJ Häuselmann and R Rizzoli. "A comprehensive review of treatments for postmenopausal osteoporosis". In: *Osteoporosis International* 14.1 (2003), pp. 2–12.

[100] Marcus P Watkins, Jin Yi Norris, Susan K Grimston, Xiaowen Zhang, Roger J Phipps, Frank H Ebetino, and Roberto Civitelli. "Bisphosphonates improve trabecular bone mass and normalize cortical thickness in ovariectomized, osteoblast connexin43 deficient mice". In: *Bone* 51.4 (2012), pp. 787–794.

[101] S El-Kaissi, JA Pasco, MJ Henry, S Panahi, JG Nicholson, GC Nicholson, and MA Kotowicz. "Femoral neck geometry and hip fracture risk: the Geelong osteoporosis study". In: *Osteoporosis international* 16.10 (2005), pp. 1299–1303.

[102] Havva Talay Calis, Merih Eryavuz, and Mustafa Calis. "Comparison of femoral geometry among cases with and without hip fractures". In: *Yonsei medical journal* 45.5 (2004), pp. 901–907.

[103] Kx? M Karlsson, Ingemar Sernbo, Kx? J Obrant, Inga Redlund-Johnell, and Olof Johnell. "Femoral neck geometry and radiographic signs of osteoporosis as predictors of hip fracture". In: *Bone* 18.4 (1996), pp. 327–330.

[104] Janne EM Koivumäki, Jérôme Thevenot, Pasi Pulkkinen, Volker Kuhn, Thomas M Link, Felix Eckstein, and Timo Jämsä. "Ct-based finite element models can be used to estimate experimentally measured failure loads in the proximal femur". In: *Bone* 50.4 (2012), pp. 824–829.

[105] WJ Choi, CM Russell, CM Tsai, S Arzanpour, and SN Robinovitch. "Age-related changes in dynamic compressive properties of trochanteric soft tissues over the hip". In: *Journal of biomechanics* 48.4 (2015), pp. 695–700.

[106] Enrico Schileo, Fulvia Taddei, Luca Cristofolini, and Marco Viceconti. "Subject-specific finite element models implementing a maximum principal strain criterion are able to estimate failure risk and fracture location on human femurs tested in vitro". In: *Journal of biomechanics* 41.2 (2008), pp. 356–367.

[107] Yunhua Luo, Sharif Ahmed, and William D Leslie. "Automation of a DXA-based finite element tool for clinical assessment of hip fracture risk". In: *Computer methods and programs in biomedicine* 155 (2018), pp. 75–83.

[108] M Viceconti. "Predicting bone strength from CT data: Clinical applications". In: *Morphologie* (2019).

[109] Y Luo, Z Ferdous, and WD Leslie. "A preliminary dual-energy X-ray absorptiometry-based finite element model for assessing osteoporotic hip fracture risk". In: *Proceedings of the Institution of Mechanical Engineers, Part H: Journal of Engineering in Medicine* 225.12 (2011), pp. 1188–1195.

[110] Jorn Op Den Buijs and Dan Dragomir-Daescu. "Validated finite element models of the proximal femur using two-dimensional projected geometry and bone density". In: *Computer methods and programs in biomedicine* 104.2 (2011), pp. 168–174.

[111] JAM MacNeil, JD Adachi, D Goltzman, RG Josse, CS Kovacs, JC Prior, W Olszynski, KS Davison, SM Kaiser, CaMos Research Group, et al. "Predicting fracture using 2D finite element modelling". In: *Medical engineering & physics* 34.4 (2012), pp. 478–484.

[112] Kim E Naylor, Eugene V McCloskey, Richard Eastell, and Lang Yang. "Use of DXA-based finite element analysis of the proximal femur in a longitudinal study of hip fracture". In: *Journal of Bone and Mineral Research* 28.5 (2013), pp. 1014–1021.

[113] Lang Yang, Lisa Palermo, Dennis M Black, and Richard Eastell. "Prediction of incident hip fracture with the estimated femoral strength by finite element analysis of DXA scans in the study of osteoporotic fractures". In: *Journal of Bone and Mineral Research* 29.12 (2014), pp. 2594–2600.

[114] S Yang, WD Leslie, Y Luo, AL Goertzen, S Ahmed, LM Ward, I Delubac, and LM Lix. "Automated DXA-based finite element analysis for hip fracture risk stratification: a cross-sectional study". In: *Osteoporosis International* 29.1 (2018), pp. 191–200.

[115] E DallAra, R Eastell, M Viceconti, D Pahr, and L Yang. "Experimental validation of DXA-based finite element models for prediction of femoral strength". In: *Journal of the mechanical behavior of biomedical materials* 63 (2016), pp. 17–25.

[116] RW Goulet, Steven A Goldstein, Michael J Ciarelli, Janet L Kuhn, MB Brown, and LA Feldkamp. "The relationship between the structural and orthogonal compressive properties of trabecular bone". In: *Journal of biomechanics* 27.4 (1994), pp. 375–389.

[117] JH Keyak, IY Lee, and HB Skinner. "Correlations between orthogonal mechanical properties and density of trabecular bone: use of different densitometric measures". In: *Journal of biomedical materials research* 28.11 (1994), pp. 1329–1336.

[118] Mara Terzini, Alessandra Aldieri, Luca Rinaudo, Giangiacomo Osella, Alberto L Audenino, and Cristina Bignardi. "Improving the hip fracture risk prediction through 2D finite element models from DXA images: validation against 3D models". In: *Frontiers in bioengineering and biotechnology* 7 (2019), p. 220.

[119] Pinaki Bhattacharya, Zainab Altai, Muhammad Qasim, and Marco Viceconti. “A multiscale model to predict current absolute risk of femoral fracture in a postmenopausal population”. In: *Biomechanics and modeling in mechanobiology* 18.2 (2019), pp. 301–318.

[120] Michelle E Danielson, Thomas J Beck, Arun S Karlamangla, Gail A Greendale, Elizabeth J Atkinson, Yinjuan Lian, Alia S Khaled, Tony M Keaveny, David Kopperdahl, Kristine Ruppert, et al. “A comparison of DXA and CT based methods for estimating the strength of the femoral neck in post-menopausal women”. In: *Osteoporosis International* 24.4 (2013), pp. 1379–1388.

[121] Yunhua Luo, Zannatul Ferdous, and William D Leslie. “Precision study of DXA-based patient-specific finite element modeling for assessing hip fracture risk”. In: *International journal for numerical methods in biomedical engineering* 29.5 (2013), pp. 615–629.

[122] Ramon D Boudreaux and Jean D Sibonga. “Advanced Hip Analysis: Simple Geometric Measurements Predict Hip Fracture Beyond Bone Mineral Density”. In: *TOJ* 1.2 (2015), pp. 109–122.

[123] Jennifer Susan Gregory, D Testi, Alison Stewart, Peter Edward Undrill, David M Reid, and Richard Malcolm Aspden. “A method for assessment of the shape of the proximal femur and its relationship to osteoporotic hip fracture”. In: *Osteoporosis International* 15.1 (2004), pp. 5–11.

[124] Nazli Sarkalkan, Harrie Weinans, and Amir A Zadpoor. “Statistical shape and appearance models of bones”. In: *Bone* 60 (2014), pp. 129–140.

[125] P Pulkkinen, J Partanen, P Jalovaara, and T Jämsä. “BMD T-score discriminates trochanteric fractures from unfractured controls, whereas geometry discriminates cervical fracture cases from unfractured controls of similar BMD”. In: *Osteoporosis international* 21.7 (2010), pp. 1269–1276.

[126] V Ercan Dinçel, Meltem Şengelen, Vesile Sepici, Turgay Çavuşoğlu, and Behçet Sepici. "The association of proximal femur geometry with hip fracture risk". In: *Clinical Anatomy: The Official Journal of the American Association of Clinical Anatomists and the British Association of Clinical Anatomists* 21.6 (2008), pp. 575–580.

[127] Isaac Castro-Mateos, Jose M Pozo, Timothy F Cootes, J Mark Wilkinson, Richard Eastell, and Alejandro F Frangi. "Statistical shape and appearance models in osteoporosis". In: *Current osteoporosis reports* 12.2 (2014), pp. 163–173.

[128] Timothy F Cootes, Christopher J Taylor, David H Cooper, and Jim Graham. "Active shape models-their training and application". In: *Computer vision and image understanding* 61.1 (1995), pp. 38–59.

[129] Julie C Baker-LePain, Kali R Luker, John A Lynch, Neeta Parimi, Michael C Nevitt, and Nancy E Lane. "Active shape modeling of the hip in the prediction of incident hip fracture". In: *Journal of Bone and Mineral Research* 26.3 (2011), pp. 468–474.

[130] Todd L Bredbenner, Robert L Mason, Lorena M Havill, Eric S Orwoll, Daniel P Nicolella, and Osteoporotic Fractures in Men (MrOS) Study. "Fracture risk predictions based on statistical shape and density modeling of the proximal femur". In: *Journal of Bone and Mineral Research* 29.9 (2014), pp. 2090–2100.

[131] Benedikt Schuler, Karl D Fritscher, Volker Kuhn, Felix Eckstein, Thomas M Link, and Rainer Schubert. "Assessment of the individual fracture risk of the proximal femur by using statistical appearance models". In: *Medical physics* 37.6Part1 (2010), pp. 2560–2571.

[132] SR Goodyear, RJ Barr, E McCloskey, S Alesci, RM Aspden, DM Reid, and JS Gregory. "Can we improve the prediction of hip fracture by assessing bone structure using shape and appearance modelling?" In: *Bone* 53.1 (2013), pp. 188–193.

[133] Tristan Whitmarsh, Karl D Fritscher, Ludovic Humbert, M Luis, Tobias Roth, Christian Kammerlander, Michael Blauth, Rainer Schubert, and Alejandro F Frangi. "Hip fracture discrimination from dual-energy X-ray absorptiometry by statistical model registration". In: *Bone* 51.5 (2012), pp. 896–901.

[134] Tristan Whitmarsh, Karl D Fritscher, Ludovic Humbert, Luís Miguel Del Rio Barquero, Tobias Roth, Christian Kammerlander, Michael Blauth, Rainer Schubert, and Alejandro F Frangi. "A statistical model of shape and bone mineral density distribution of the proximal femur for fracture risk assessment". In: *International Conference on Medical Image Computing and Computer-Assisted Intervention*. Springer. 2011, pp. 393–400.

[135] Stanley Durrleman, Marcel Prastawa, Nicolas Charon, Julie R Korenberg, Sarang Joshi, Guido Gerig, and Alain Trouvé. "Morphometry of anatomical shape complexes with dense deformations and sparse parameters". In: *NeuroImage* 101 (2014), pp. 35–49.

[136] Tommaso Mansi. "Image-based physiological and statistical models of the heart: Application to tetralogy of fallot". PhD thesis. École Nationale Supérieure des Mines de Paris, 2010.

[137] Marc Vaillant and Joan Glaunès. "Surface matching via currents". In: *Biennial International Conference on Information Processing in Medical Imaging*. Springer. 2005, pp. 381–392.

[138] Stanley Durrleman, Xavier Pennec, Alain Trouvé, Paul Thompson, and Nicholas Ayache. "Inferring brain variability from diffeomorphic deformations of currents: an integrative approach". In: *Medical image analysis* 12.5 (2008), pp. 626–637.

[139] Tommaso Mansi, Ingmar Voigt, Benedetta Leonardi, Xavier Pennec, Stanley Durrleman, Maxime Sermesant, Hervé Delingette, Andrew Mayall Taylor, Younes Boudjemline, Giacomo Pongiglione, et al. "A statistical model for quantification and prediction of cardiac

remodelling: Application to tetralogy of fallot". In: *IEEE transactions on medical imaging* 30.9 (2011), pp. 1605–1616.

[140] Stanley Durrleman, Xavier Pennec, Alain Trouvé, and Nicholas Ayache. "Statistical models of sets of curves and surfaces based on currents". In: *Medical image analysis* 13.5 (2009), pp. 793–808.

[141] Stanley Durrleman. "Statistical models of currents for measuring the variability of anatomical curves, surfaces and their evolution". PhD thesis. 2010.

[142] Jan L Bruse, Kristin McLeod, Giovanni Biglino, Hopewell N Ntsinjana, Claudio Capelli, Tain-Yen Hsia, Maxime Sermesant, Xavier Pennec, Andrew M Taylor, Silvia Schievano, et al. "A statistical shape modelling framework to extract 3D shape biomarkers from medical imaging data: assessing arch morphology of repaired coarctation of the aorta". In: *BMC medical imaging* 16.1 (2016), p. 40.

[143] Ian T Jolliffe and Jorge Cadima. "Principal component analysis: a review and recent developments". In: *Philosophical Transactions of the Royal Society A: Mathematical, Physical and Engineering Sciences* 374.2065 (2016), p. 20150202.

[144] Timothy F Cootes, Cristopher J Taylor, et al. *Statistical models of appearance for computer vision*. 2004.

[145] Agnar Höskuldsson. "PLS regression methods". In: *Journal of chemometrics* 2.3 (1988), pp. 211–228.

[146] Roman Rosipal and Nicole Krämer. "Overview and recent advances in partial least squares". In: *International Statistical and Optimization Perspectives Workshop" Subspace, Latent Structure and Feature Selection"*. Springer. 2005, pp. 34–51.

[147] Amir Abbas Zadpoor, Gianni Campoli, and Harrie Weinans. "Neural network prediction of load from the morphology of trabecular bone". In: *Applied Mathematical Modelling* 37.7 (2013), pp. 5260–5276.

Acknowledgements

First of all, at the end of this path, I would like to thank Professor Alberto Audenino, my supervisor, for giving me the opportunity to carry out the work presented in this thesis as well as other activities with independence and freedom. I would like to thank him for his boundless knowledge, for his capability to arise much more doubts and questions than those you had in mind before meeting him, for always welcoming us in his office no matter what he was doing, ready to listen to anything we had to say.

I would like to thank Prof. Cristina Bignardi, for involving me in a number of activities throughout these years, for her helpfulness and humanity.

I am also deeply grateful to Prof. Umberto Morbiducci, without whom the last chapter of this thesis would probably not exist, other than for his frequent visits and encouragements.

The words I can write here would never be enough to express my profound gratitude to Dr. Mara Terzini, who has represented a fundamental guiding light throughout all my life in Politecnico, from all possible perspectives, as well as an inspiring unattainable model.

I would like to thank the people I met at the University of Sheffield during my stay there and in particular Dr. Pinaki Bhattacharya, not only for

what I had the possibility to learn, but also for making me feel part of the group right from the start.

In the end, I am deeply grateful to all the colleagues I've had the opportunity and luck to meet in these last three years and a half. Thank you all for having become a second big family to me.
In particular, I would like to thank those who have become real friends, for their support and presence during the hardest times, for the discussions, the outbursts, the breaks together. Thank you for the time we have shared and spent together, for the laughs and of course, last but not least, for the cheerful noise in the office.

Short *Curriculum Vitae*

Alessandra Aldieri was born in Torino (TO), Italy, in 1992. She received a BS degree (July 2014) and a MS degree (October 2016) in Biomedical Engineering from Politecnico di Torino.
After working under the supervision of Professors Alberto Audenino and Cristina Bignardi during her MS thesis, she was a PhD student in Biomedical Engineering at the Department of Mechanical and Aerospace Engineering, Politecnico di Torino, from November 2016 to October 2019.
From 2015 she has been working as a teaching assistant at Politecnico di Torino, in courses related to the biomechanics field: "Mechanical Bioengineering" ("Bioingegneria Meccanica") (AY 2015/2016, AY 2016/2017, AY 2017/2018, AY 2018/2019), "Solid Biomechanics" ("Biomeccanica dei Solidi") (AY 2015/2016, AY 2016/2017, AY 2017/2018, AY 2018/2019, AY 2019/2020).
From March to June 2019 she worked as a visiting PhD student at the University of Sheffield (Sheffield, UK).

Publications

Terzini, M. & **Aldieri, A.**, Rinaudo, L., Osella, G., Audenino, A. L., & Bignardi, C. (2019). Improving the hip fracture risk prediction through 2D finite element models from DXA images: validation against 3D models. *Frontiers in bioengineering and biotechnology*, 7, 220.

Aldieri, A., Terzini, M., Osella, G., Priola, A. M., Angeli, A., Veltri, A., Audenino A.L. & Bignardi, C. (2018). Osteoporotic hip fracture prediction: is T-score based criterion enough? A Hip Structural Analysis based model. *Journal of Biomechanical Engineering.*

Aldieri, A., Terzini, M., Bignardi, C., Zanetti, E. M., & Audenino, A. L. (2018). Implementation and validation of constitutive relations for human dermis mechanical response. *Medical & biological engineering & computing*, 1-11.

Terzini, M., **Aldieri, A.**, Zanetti, E. M., Massai, D., Audenino, A. L., & Bignardi, C. (2018). Native human dermis versus human acellular dermal matrix: A comparison of biaxial mechanical properties. *Australasian Medical Journal*, 11(8), 434-442.

Zanetti, E. M., **Aldieri, A.**, Terzini, M., Calì, M., Franceschini, G., & Bignardi, C. (2017). Additively manufactured custom load-bearing implantable devices: grounds for caution. *Australasian Medical Journal*, 10(8), 694.

Conferences

Oral Presentation

Author: Terzini, M.,**Aldieri, A.**, Bignardi, C., Audenino, A. L., Morbiducci, U. The Role of Geometric Patterns in the Osteoporotic Fracture: a Statistical Shape Modelling Approach. 25th Congress of the European Society of Biomechanics Vienna, 2019, July 7-10

Presenting author: **Aldieri, A.**, Terzini, M., Bignardi, C., Audenino, A. L., Morbiducci, U. Statistical Shape Analysis for the Assessment of

Proximal Femur Shape Features Meaningful to Osteoporotic Risk of Fracture. Summer Biomechanics, Bioengineering, and Biotransport Conference. Seven Springs, 2019, June 25-28.

Presenting author: **Aldieri, A.**, Terzini M., Zanetti E., Audenino A. L., Bignardi C. A 3D printed conversion device for the equi-biaxial mechanical characterization of human acellular dermal matrix. II Congresso Nazionale IDBN. Pavia, 2018, September 5-7.

Presenting author: **Aldieri, A.**, Terzini M., Osella G., Priola A. M., Angeli A., Audenino A. L., Bignardi C. Can Hip Structural Analysis predict osteoporotic hip fracture? A patient-specific Finite Element study. 8th World Congress of Biomechanics. Dublin, 2018, July 8-12.

Presenting author: **Aldieri, A.**, Terzini M., Bignardi C., Zanetti E. M., Audenino A. L. A constitutive framework for human dermis mechanical modelling. Materials and Contact Characterisation VIII, Tallinn, 2017, 21-23 June.

Author: Terzini M., **Aldieri, A.**, Bignardi C., Zanetti E. M., Audenino A. L. Equi-biaxial tests for mechanical characterization of human acellular dermal matrices through a custom-made biaxial fixture. Materials and Contact Characterisation VIII, Tallinn, 2017, 21-23 June.

Presenting author: **Aldieri, A.**, Terzini M., Bignardi C., Audenino A. L. Dermis Constitutive Model Identification From Experimental Strain Distribution. Società Italiana Biomateriali. 2017, Milan, May 24-26.

Poster Presentation

Author: Terzini M., **Aldieri, A.**, Rinaudo L., Osella G, Audenino A. L., Bignardi C. DXA-derived Finite Element models to enhance the hip

fracture risk prediction. IX annual meeting of the ESB-ITA. Bologna, September 30-October 1, 2019

Presenting author: **Aldieri, A.**, Terzini M., D. Massai D., C. Bignardi C., A.L. Audenino A- L. Development of an Animal-Free Methodology for Mechanical Performance Assessment of Engineered Skin Substitutes. II Centro 3R annual meeting. Genova, June 20-21.

Author: Terzini M., **Aldieri, A.**, Castaldo C., Di Meglio F., Nurzynska D., Serino G., Audenino A. L., Massai D. Mechanical behaviour of human decellularized dermis as scaffold for myocardial regeneration. 8th World Congress of Biomechanics. Dublin, 2018, July 8-12.

Author: Terzini M., Massai D., Romano V., Castaldo C., Di Meglio F., Nurzynska D., **Aldieri, A.**, Serino G., Bignardi C, Audenino A. L. Human Decellularized Dermis as Novel Scaffold for Cardiac Regenerative Medicine: Structure and Mechanical Behaviour. GNB 2018 - Sixth National Congress of Bioengineering. Milan, 2018, June 25-28.

Presenting author: **Aldieri, A.**, Terzini M., A. M. Priola, G. Osella, A. Veltri, A. L. Audenino, C. Bignardi. Hip fracture risk prediction through FE analysis: influence of HSA parameters. European Society of Biomechanics – Italian Chapter. Rome, 2017, September 28-29.

This Ph.D. thesis has been typeset by means of the TEX-system facilities. The typesetting engine was pdfLATEX. The document class was `toptesi`, by Claudio Beccari, with option `tipotesi=scudo`. This class is available in every up-to-date and complete TEX-system installation.